TURBULENT MIXING IN STABLY-STRATIFIED FLUIDS SUBJECTED TO ZERO-MEAN SHEAR

Thesis by

Imad A. Hannoun

In Partial Fulfillment of the Requirements

for the Degree of

Doctor of Philosophy

California Institute of Technology

Pasadena, California

1987

(Submitted October 10,1986)

To my parents

ACKNOWLEDGEMENT

I would like to thank my adviser Professor E. John List for his continued support, guidance, kindness, and friendship throughout my four years at Caltech. To him I am greatly indebted.

I would like to thank Dr. Harindra Fernando who helped me define my project while he was a post-doctoral fellow at Caltech. Thanks are also due to Professors Jorg Imberger, Norman Brooks, and Donald Coles whose valuable suggestions are appreciated. Dr. Bob Koh's help and advice are also greatly appreciated.

Among my fellow students I would like to thank Dr. Jim Skjelbreia for answering my frequent questions about lasers and computers. The help of Dr. Panos Papanicolaou in operating the laser-Doppler velocimeter and that of Dr. Dimitri Papantoniou in using the data acquisition system with the Reticon camera proved to be invaluable. Thanks are also due to Dennis Lyn, Marco Rasi, Peter Goodwin, and Francis Ting. The help of Dr. M. Koochesfahani in demonstrating the use of the image processor is appreciated.

The work could not have been finished in this period of time without the enthusiastic help of Joe Fontana. His expert advise and ingenious designs insured trouble-free operation of all the mechanical equipment. Thanks are also due to Rich Eastvedt, Elton Daly, and Leonard Montenegro.

I wish to thank Rayma Harrison and Gunilla Hastrup for their help in obtaining obscure references. Furthermore, their friendship and sense of humor brightened many of my days. The help of Joan Mathews in taking care of many administrative problems and insuring the arrival of my stipend is appreciated. Thanks are also due to Melinda Hendrix-Werts and Sandy Brooks.

I am very grateful to my undergraduate Professors George Ayoub and Constantine Inglessis who encouraged me to pursue graduate study.

Last but by no means least, I would like to thank my whole family for providing me with support and encouragement. The continuous help and sacrifices of my parents are deeply appreciated. Moreover, I would like to thank my wife Betty for her ideas and encouragement.

This work was financially supported by the National Science Foundation Grant No. MSM 84-12641, A01, and the California Institute of Technology through a variety of assistantships.

ABSTRACT

The interaction of a sharp density interface with oscillating grid induced shear-free turbulence was experimentally investigated. A linear photodiode array was used in conjunction with laser-induced fluorescence to measure the concentration of a tracer that was initially located in the less dense layer. A laser-Doppler velocimeter was used to measure the vertical component and a horizontal component of velocity near the interface, and also at a point where tracer concentration was measured. Potential refractive index fluctuation problems were avoided using solutes that provided a homogeneous optical environment. The study consists of two major parts.

In the first part of the investigation, energy spectra, velocity correlations, and kinetic energy fluxes were measured. Amplification of the horizontal turbulent velocity fluctuations, coupled with a sharp reduction in the vertical velocity fluctuation level, was observed near the density interface. Moreover, the experiments indicate that the density interface acts in a manner qualitatively similar to a rigid flat plate inserted in the flow. These findings are in agreement with previous results pertaining to shear-free turbulence near rigid walls (Hunt & Graham 1978).

In the second part of the investigation, internal wave spectra, wave amplitudes and velocities, and the interfacial mixing layer thickness were measured. The results indicate that mixing occurs in intermittent bursts and that the local gradient Richardson number J remains constant for a certain range of the overall Richardson number R_j. The spectra of the internal waves decay as f^{-3} at frequencies below the maximum Brunt-Väisälä frequency. These findings give support to a model of oceanic turbulence proposed by Phillips (1977) in which the internal waves are limited in their spectral density by sporadic local instabilities and breakdown to turbulence. The results also indicate that, for a certain R_j range, the thickness of the interfacial layer (normalized by the integral length scale of the turbulence) is a decreasing function of R_j. At sufficiently high R_j the interfacial thickness becomes limited by diffusive effects. A simple model for entrainment at a density interface in the presence of shear-free turbulence is presented and compared with the observations.

TABLE OF CONTENTS

LIST OF FIGURES

LIST OF TABLES

LIST OF SYMBOLS

a	Amplitude of grid oscillation (L)
a_{i1}, a_{i2}, $a_{\rho 1}$, $a_{\rho 2}$	Constants in equations (A.1) and (A.2)
A	Constant
b_{i1}, b_{i2}, $b_{\rho 1}$, $b_{\rho 2}$	Constants in equations (A.1) and (A.2)
B	Constant
c	Constant in equation (1.2.3)
c_1	Constant
c_i, c_ρ	Constants in equations (A.1) and (A.2)
count	Number of array diodes (1024) + blanking period clocks (64)
C	Dye concentration (M/L^3)
C_A, C_B	Concentration of component A (or B) (mass of solute/volume of solution)
C_u	Time-averaged dye concentration in the upper mixed layer (M/L^3)
$\overline{C'}$	Time-averaged maximum vertical concentration gradient (M/L^4)
d	Depth of the fluid layer above the thermocline in the ocean (L)

D	Depth of the turbulent layer measured from a virtual origin (L)
E_u	Energy spectrum for the horizontal velocity fluctuations (L^2/T)
E_w	Energy Spectrum for the vertical velocity fluctuations (L^2/T)
f	Frequency (1/T)
f_a	Estimated frequency output of the LDV photodiodes (1/T)
f_g	Grid oscillation frequency (1/T)
f_i	Input frequency to the LDV processor (1/T)
f_m	Frequency of occurence of mixing events (1/T)
f_D	Doppler frequency (1/T)
g	Gravitational acceleration (L/T^2)
G	Some function
h	Interfacial layer thickness (L)
h_c	Interfacial layer thickness = $C_u/\overline{C'}$ (L)
h_s	'Static' thickness of the interface after the stirrer has been stopped and the turbulent motions have calmed down (L)
i	Refractive index
i_A	Refractive index of a solution containing solute A
i_B	Refractive index of a solution containing solute B
i_{AB}	Refractive index of a solution containing both solutes

A and B

I Intensity of the laser beam after it traverses a distance x_3 in the fluid (W/L^2)

I_0 Initial intensity of the laser beam at $x_3 = 0$ (W/L^2)

J Local gradient Richardson number

J_i Local gradient Richardson number = $(L_o/\zeta)^2 (n_a/N_m)^2$

k Horizontal wave number (1/L)

ℓ Integral length scale of the turbulence defined as the area under the curve when the horizontal velocity auto-correlation coeffficient is plotted as a function of horizontal distance (L)

L Integral length scale of the turbulence = $[\tau][\sigma_w]$ = .1 D (L)

m Exponent in $u_e/[\sigma_u]_o \sim P_e^{-m}$

M Center-to-center spacing of oscillating grid bars

n Exponent in equation (1.2.1)

n_a Internal wave frequency = $c_1(w_i/\zeta)$ (1/T)

N_m Maximum averaged Brunt-Väisälä frequency (1/T)

P_e Peclet number = $(\sigma_u)_o \ell_o/\kappa$

P_r Prandtl number = ν/κ

q^2 Turbulent kinetic energy per unit mass = $1/2(2u'^2 + w'^2)$ $(L/T)^2$

Q Ratio of the active area of the interface (where entrainment

is occuring) to its total area

R_e Reynolds number = $[\sigma_w]^2[\tau]/\nu$

R_i Overall Richardson number = $\Delta b \ell_o/(\sigma_u)_o^2$

R_j Overall Richardson number = $\Delta b L_o/[\sigma_u]_o^2$

$(R_j)_a$ Cut-off value of R_j below which buoyancy effects are negligible

s Amplitude of the thermocline displacement (L)

s_a Width of the glass container used in determining ϵ (L)

t Time (T)

u Horizontal velocity in the x_1 direction (L/T)

u' Fluctuating horizontal velocity in the x_1 direction (L/T)

u_e Entrainment velocity = dD/dt (L/T)

u_s Typical velocity scale near an interface (L/T)

U'_m Maximum rate of shear (1/T)

v Horizontal velocity in the x_2 direction (unmeasured) (L/T)

v' Fluctuating horizontal velocity in the x_2 direction (L/T)

V Analog output of the LDV processor (V)

V_c Averaged voltage output of the array (Appendix B) (V)

$(V_c)_O$ Value of V_c at C = 0 (V)

V_i Analog output of the LDV processor in the calibration (V)

w Vertical velocity (in the x_3 direction) (L/T)

w' Fluctuating vertical velocity (L/T)

w_d Instantaneous vertical velocity of the internal waves (L/T)

w_h r.m.s. vertical velocity at the entrainment interface (L/T)

w_i Measure of the vertical velocity of the internal waves (L/T)

x_1 Horizontal coordinate (in whose direction velocity measurements were made) (L)

x_2 Horizontal coordinate (in whose direction velocity measurements were not made) (L)

x_3 Vertical coordinate (L)

z Vertical distance away from the grid (L)

z_a Vertical distance from an arbitrary origin (L)

z_c Vertical distance to a certain concentration contour line measured from an arbitrary origin (L)

GREEK SYMBOLS

α constant

$\overline{\alpha_k^2}$ Mean square displacement of the thermocline (L^2)

β constant

δ^ν Thickness of the viscous sub-layer in the theory of Hunt & Graham (1984) (L)

Δb Buoyancy jump across the density interface (L/T^2)

Δi_{all} Maximum allowable change in the refractive index

Δz Spatial resolution of the Reticon camera (L)

$\Delta\rho_{max}$ Maximum density difference corresponding to Δi_{all} (M/L^3)

ϵ Dye absorption coefficient (L^2/M)

ζ Measure of the amplitude of the internal waves (L)

η Vertical distance away from the flat plate (L)

θ Measure of the inhomogeneity in velocity along a horizontal line (Appendix C)

κ Molecular diffusivity (L^2/T)

ν Kinematic viscosity (L^2/T)

ξ Vertical distance away from the density interface (L)

ρ Fluid density (M/L^3)

ρ_{AB} Fluid density of a solution containing solutes A and B (M/L^3)

ρ_1 Fluid density in the upper layer (M/L^3)

ρ_2 Fluid density in the lower layer (M/L^3)

σ_u r.m.s. velocity in the x_1 horizontal direction (L/T)

σ_w r.m.s. velocity in the vertical direction (L/T)

τ Integral time scale of the turbulence defined as the area under the curve when the auto-correlation coefficient of w(t) is plotted against time (T)

Φ Spectrum of the internal wave vertical displacement fluctuations (L^2T)

χ Deviation of a certain concentration contour from its best fit least-squares line (L)

ψ Vertical flux of clear fluid = $[1-C/C_u]w$ (L/T)

ω Frequency of the first mode internal wave (1/T)

ω_a Adjustable frequency of input clock to Reticon array (1/T)

OTHER SYMBOLS

$\overline{\quad}$ (Overbar) Time average

[ ] Spatial average in a horizontal plane

SUBSCRIPTS

o Pertains to quantities in a homogeneous fluid at the location of the density interface or the flat plate

ref Pertains to quantities at z/a = 7.70 in a homogeneous fluid

CHAPTER 1

INTRODUCTION

1.1 Introductory Notes and Scope of Work

Turbulent mixing, and especially turbulent mixing within density stratified fluids, continues to be a perplexing problem in environmental and geophysical fluid dynamics. Of particular interest is mixing in the neighborhood of relatively sharp density interfaces in oceans, lakes, reservoirs, and the atmosphere. Since these interfaces can control and dramatically reduce the vertical transport of momentum and mass it is desirable both to predict their location and characterize the exchange processes that occur across them.

In environmental fluid mechanics, an understanding of these mixing processes is essential in determining water quality in water bodies containing a sharp density interface. The presence of such an interface, by suppressing fluid turbulence, limits the downward transfer of pollutants and gases such as CO_2 and O_2 from the upper mixed layers (Fischer *et al* 1979) and the upward transport of nutrients to organisms that live in the surface layer (Scavia & Robertson 1981). It has important consequences in the design of wastewater outfalls. In the atmosphere severe air pollution problems may result from the presence of thermal inversions that

inhibit the vertical transport of pollutants. Here again, a knowledge of the exchange processes across the inversion layer can be important in predicting and controlling air quality in the lower atmosphere.

Several prior attempts (Gartrell 1979a, Kato & Phillips 1969, Kantha, Phillips & Azad 1977, Wu 1973, Hopfinger & Toly 1976, Wolanski & Brush 1976, Bouvard & Dumas 1967, Folse *et al* 1981, Linden 1975, Crapper & Linden 1974, Hopfinger & Linden 1982, Kantha & Long 1980, Turner 1968, Thompson & Turner 1975, McDougall 1979a, Fernando & Long 1983,1985a,b,c, Cromwell 1960, and Rouse & Dodu 1955), both experimental and theoretical, have been made at observing and modelling the mixing across sharp density interfaces. However, most of these studies have focused on understanding bulk quantities, such as the entrainment rate (*i.e.* the rate of mass transfer of one fluid into the other) and the thickness of the interfacial layer, rather than investigating in detail the mechanics of the processes involved. It is thought that this is probably a consequence of the limitations in the experimental equipment available. In as much as these bulk parameters are important, these studies have been a useful first approach. However, it is felt that a closer scrutiny of the interfacial layer structure and processes involved in the mixing is of primary importance to a fundamental understanding of the problem.

In this work, we report the details of a study on the nature of entrainment and the structure of sharp density interfaces subjected to shear-free turbulence induced by an oscillating grid. The thrust of the work is experimental but also includes the development of a phenomenological model to aid in the prediction of the interfacial layer thickness, the rate of entrainment, and the associated internal waves. The experiments were performed in a two-layer stably-stratified fluid and involved measurements of both fluid velocity and the concentration of a tracer element initially placed in only one of the fluid layers. Velocity measurements were performed with a laser-Doppler velocimeter and vertical tracer concentration profiles were determined using laser-induced fluorescence. Refractive index fluctuation problems were avoided by maintaining a uniform refractive index in the fluid across the interface.

A stable stratification inhibits turbulence so that a continuous supply of energy is needed to sustain the fluid motion. This can be achieved by use of an oscillating grid located in one of the fluid layers. Previous experiments by others have used this and other stirring mechanisms:

- Shear production of turbulence as in stratified shear flows (Gartrell 1979a, Kato & Phillips 1969, Kantha Phillips & Azad 1977, and Wu 1973).
- Convective heating or cooling on the surface (Hopfinger

& Linden 1982, and Kantha & Long 1980).

- Oscillating grids (Bouvard & Dumas 1967, Wolanski & Brush 1976, Folse *et al* 1981, Linden 1975, Crapper & Linden 1974, Hopfinger & Toly 1976, Turner 1968, Thompson & Turner 1975, McDougall 1979a, Fernando & Long 1983, 1985a,b, Cromwell 1960, and Rouse & Dodu 1955).

In our experiments, the oscillating grid was chosen because it is simple to build and run. Furthermore, with such a geometry the equations of energy conservation can be greatly simplified since the mean turbulent kinetic energy flux is one-dimensional.

In the following section we discuss previous theories and experiments pertinent to the problem. The details of the experimental method and apparatus are discussed in Chapter 2. Chapter 3 contains the results of velocity measurements in and near a density interface and close to a rigid flat plate and discusses their significance. The results of concentration measurements and concentration-velocity correlations are presented in Chapter 4. A simple model for turbulent mixing and entrainment at a shear-free density interface is also proposed. Chapter 5 is a summary of the results obtained and the conclusions derived therefrom.

1.2 Historical Background

1.2.1 Overview

The pioneering experiments of Rouse & Dodu (1955) showed that when a stably stratified fluid is stirred by an oscillating grid (in their case located at the base of a container) a mixed layer, whose depth D increases with time, develops near the mixer. The turbulence decays across an interfacial layer of thickness h located between the mixed layer and the unmixed fluid. A large buoyancy jump $\Delta b = 2g(\rho_2 - \rho_1)/(\rho_2 + \rho_1)$ is created between the two layers, where g is the gravitational acceleration and ρ_1 and ρ_2 are the densities in the upper and lower layers respectively (see Figure 1.1). Cromwell (1960) constructed a similar experiment, but further interest in the problem did not develop until Bouvard & Dumas (1967) and Turner (1968) made some careful measurements. Since then, many identical or similar experiments have been conducted (Wolanski & Brush 1976, Folse *et al* 1981, Linden 1975, Hopfinger & Toly 1976, Crapper & Linden 1974, Thompson & Turner 1975, McDougall 1979a, and Fernando & Long 1983,1985a,b).

In these oscillating grid experiments investigators have proposed that an entrainment velocity, defined as $u_e = dD/dt$, is given by a simple law of the form

$$u_e/(\sigma_u)_o \sim R_i^{-n}, \qquad (1.2.1)$$

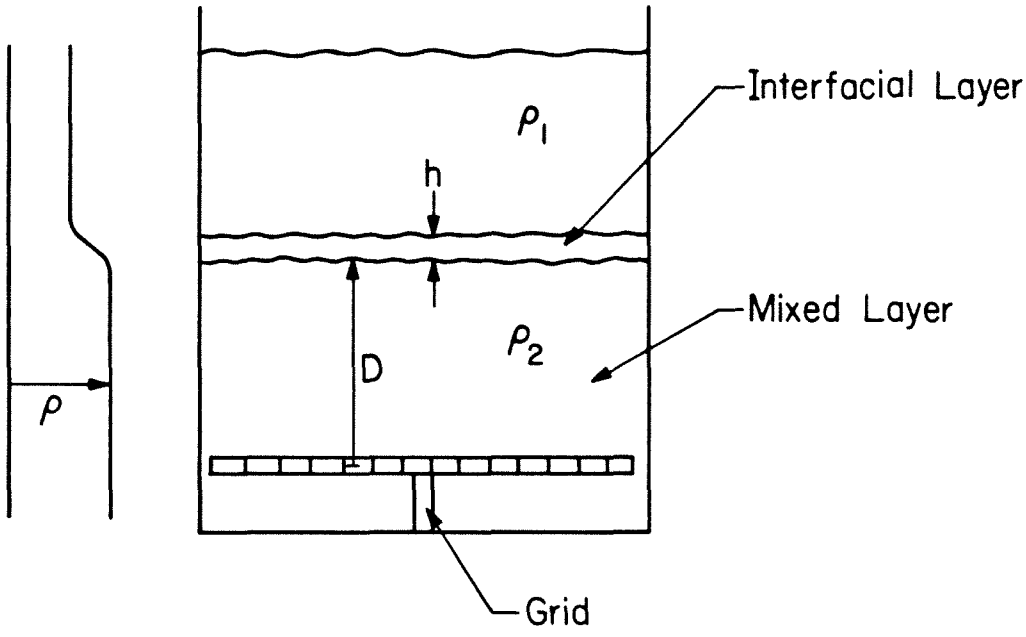

Figure 1.1: Schematic diagram of the experiment of Rouse & Dodu (1955)

where σ_u is the r.m.s. Horizontal velocity and the subscript o here and subsequently refers to the quantity being measured in a *homogeneous* fluid at the same distance from the oscillating grid as the density interface. R_i is an overall Richardson number defined by $R_i = \Delta b \, \ell_o / (\sigma_u)_o^2$, and ℓ_o is an integral length scale of the turbulence defined as the area under the auto-correlation coefficient curve of the horizontal velocity component (when the velocity measurements are obtained with a rotating probe). It is interesting to note that some investigators, such as Turner (1968), used overall Richardson numbers based on the frequency of the grid oscillation. However, the two different forms of the overall Richardson number have been shown to be equivalent (Thompson & Turner 1975).

In his experiments Turner found $n = 3/2$ when the density stratification was due to salt. When the stratification resulted from a temperature gradient, the value of n was found to be about 1. Turner (1979) suggested that viscosity differences cannot be used to explain the different values of n. He proposed that the large differences in u_e using salt and heat can only be explained by consideration of the molecular diffusion of mass or heat as defined by the appropriate diffusivity κ. He added a second dimensionless number, a Peclet number $P_e = (\sigma_u)_o \, \ell_o / \kappa$, and proposed that the entrainment velocity would be a function of both an overall Richardson number and the Peclet number of the form

$$u_e/(\sigma_u)_o = f\ (R_i, P_e). \qquad (1.2.2)$$

Turner (1968) suggested that

$$u_e/(\sigma_u)_o = R_i^{-1}\ (\ c + R_i P_e)^{-1/2}, \qquad (1.2.3)$$

where c is a constant. When P_e is small this relationship reduces to

$$u_e/(\sigma_u)_o \sim R_i^{-1}. \qquad (1.2.4)$$

When P_e is large (1.2.3) becomes

$$u_e/(\sigma_u)_o \sim R_i^{-3/2}\ P_e^{-1/2}. \qquad (1.2.5)$$

The work of Turner motivated other investigations of the nature of the mixing at a density interface and the properties of oscillating grid turbulence. In the following section we will discuss the results of some of these studies.

1.2.2 Properties of Oscillating Grid Turbulence

In order to evaluate properly the velocity and length scales of the fluid turbulence near the density interface several studies have addressed the problem of the evolution of the turbulence as a function of distance from the grid. Thompson & Turner (1975), by using a rotating hot film anemometer and three different grid geometries, measured r.m.s. velocities and integral length scales of the turbulence generated by an oscillating grid in a homogeneous fluid. They found that the integral length scale varied as $\ell \sim z$ where z is a vertical distance away from the grid. This is in agreement with a result by Bouvard and Dumas (1967). Thompson & Turner also found that the r.m.s. horizontal velocity decayed as $\sigma_u \sim z^{-3/2}$. However, Hopfinger & Toly (1976) suggested that a better fit to their data is $\sigma_u \sim z^{-1}$. Other experiments by Hopfinger & Toly (1976) and McDougall (1979a) using laser-Doppler anemometry showed that $\sigma_u \sim z^{-1}$. The dependence of σ_u on the stirring frequency f_g was systematically studied by Thompson & Turner (1975) and McDougall (1979a). They both found that $\sigma_u \sim f_g$ for grids consisting of square bars.

1.2.3 Mixing Near a Density interface

After Turner's work clearly showed different entrainment rates for heat and salt interfaces, other investigators attempted to explain the differences both theoretically and experimentally. A

problem that confronted experimentalists was that the molecular diffusivities of heat and salt differ by about two orders of magnitude and that other suitable solutes with intermediate diffusivities are unavailable. This made the systematic study of the problem over a continuous range of P_e very difficult. As a result, the experimental data that is available tends to be at either low P_e (using heat) or rather high P_e (using salt or other solutes with comparable diffusivities). The results at each of these ranges as well as those obtained at very high R_i will be discussed next.

1.2.3.1 High Peclet Number Investigations

Previous attempts to estimate the mixing rate near a high Peclet number density interface in the absence of shear have been based on the energetics of the mixing process. Linden (1975) proposed that the rate of change of potential energy due to mixing is proportional to the total turbulent kinetic energy flux available at the entrainment interface. This argument leads to a relationship of the form $u_e/(\sigma_u)_o \sim R_i^{-1}$. However, other studies performed with oscillating grids (Hopfinger & Toly 1976, Turner 1968, Fernando & Long 1983, and Folse *et al* 1981) strongly suggest that entrainment takes place at a rate much slower than that predicted by the $u_e/(\sigma_u)_o \sim R_i^{-1}$ relationship. Long (1978) extended the results of the rapid distortion theory of Hunt and Graham (1978) (referred to

hereafter as HG) to estimate the vertical and horizontal r.m.s. velocities at the entrainment interface. Accordingly, large eddies of the size of the integral length scale of the turbulence tend to flatten at the density interface, thus transferring the kinetic energy of the vertical velocity component to the horizontal components. Long further argued that the vertical r.m.s. velocity at the entrainment interface, denoted as w_h, reduces to a value corresponding to that appropriate to the interfacial waves, which is much smaller than the r.m.s. horizontal velocity component near the entrainment interface. In a detailed analysis Long finds $w_h/(\sigma_u)_o \sim R_i^{-1/4}$ and $u_e/(\sigma_u)_o \sim R_i^{-7/4}$. As pointed out by Fernando & Long (1985a), the latter relationship can also be obtained by assuming that the rate of change of potential energy due to mixing is proportional to the vertical kinetic energy flux available at the interface. Experiments by Folse *et al* (1981) and Fernando & Long (1983,1985a,b) support the $u_e/(\sigma_u)_o \sim R_i^{-7/4}$ behavior, whereas Turner (1968) and Hopfinger & Toly (1976) find $u_e/(\sigma_u)_o \sim R_i^{-3/2}$. Long's model also suggests that the entrainment occurs due to the breaking of interfacial waves in the interfacial layer. This wave-breaking is considered to occur through a resonance mechanism in which the forcing is accomplished by the "quasi-isotropic" eddies of the mixed layer acting on the upper surface of the interfacial layer (Fernando & Long 1983). Some of the postulates of Long's (1978) model have been verified by Fernando & Long (1983,1985b) and Folse *et al* (1981). However, the mechanism for mixing and

wave-breaking, the flattening of the eddies near the interface in accordance with the theory of HG, as well as the dependence of the interfacial wave velocities on R_i have not been experimentally verified in oscillating grid experiments. McDougall (1979a) carried out experiments to measure turbulent r.m.s. velocities using an LDV. Close to the density interface he observed a hint of some amplification of the horizontal velocity at high R_i but did not have enough data to assert this with confidence.

Linden (1973) had previously proposed another model for turbulent entrainment at a high R_i density interface. He experimentally investigated the effects of a vortex ring impinging on a sharp density interface and developed a model for the ring-interface interaction. The model was then extended to calculate the rate of entrainment at a density interface in the presence of oscillating grid turbulence. This was done with the conjecture that, in this particular case, a vortex ring appears to be a good approximation to a turbulent eddy. Linden found that $u_e/u_s \sim Q\, R_l^{-3/2}$, where $R_l = \Delta b\, l_s / u_s^2$, is an overall Richardson number, u_s and l_s are typical velocity and length scales respectively near the interface, and Q is the ratio of the active area of the interface (where entrainment is occuring) to its total area. This result reduces to the entrainment law suggested by Turner (1979), *i.e.* $u_e/(\sigma_u)_o \sim R_i^{-3/2}$, if Q is a constant and u_s and l_s are taken to be equal to $(\sigma_u)_o$ and ℓ_o respectively. However,

the implication that Q is a constant as well as some other assumptions in Linden's model have not been tested.

The thickness of the interfacial layer h in salt stratified experiments was determined by Crapper & Linden (1974) using both a traveling conductivity probe and shadowgraph techniques. They found h/ℓ_o to be independent of R_i and given by $h/\ell_o \sim 1\text{-}1.5$. They also observed that there was no significant difference between their time-averaged and instantaneous density profiles. Hopfinger & Toly (1976) also measured h/ℓ_o and found a clear dependence on R_i which contradicts the observations of Crapper & Linden. Hopfinger & Toly also measured h_s, the 'static' thickness of the interface after the stirrer has been stopped and the turbulent motion had calmed down. They observed that $h_s \sim \ell_o$ and that $(h-h_s)/h_s \sim R_i^{-1}$. Measurements by Fernando & Long (1985b) using a traveling conductivity probe suggest that at low R_i, an instantaneous density profile is not a good indicator of the average profile. They also find that h/D is a constant considerably less than that obtained by Crapper & Linden.

As evident from the above discussion there is considerable confusion regarding the thickness of the interfacial layer and the shape of the density profile. Some of these discrepancies might be partly due to the experimental methods employed. The use of a shadowgraph might be misleading in determining h because the method averages over the entire width of the experimental facility. Moreover, a traveling conductivity probe may produce significant

perturbations as it penetrates the density interface.

In experiments using different types of solutes, Wolanski & Brush (1976) concluded that the exponent n in (1.2.1) is a function of the Prandtl number $Pr = \nu/\kappa$, where ν is the viscosity. Such an observation cannot be explained by either Linden's (1973,1975) or Long's (1978) theoretical models since both are independent of viscosity and diffusion effects (at high Reynolds numbers). McDougall (1979a) suggested that this observation might be due to non-Newtonian effects exhibited by some of the fluids used by Wolanski and Brush.

1.2.3.2 Low Peclet Number Investigations

In experiments involving heat as a stratifying agent, Crapper & Linden (1974) found that molecular diffusion is important in the determination of the interfacial structure at $P_e \leq 200$. In this case they found that a diffusive core is formed at the center of the interfacial layer across which all transport occurs by molecular diffusion. Fernando (1986) pointed out that if all transport is due to molecular diffusion then $u_e \sim \kappa/h$. By invoking the relationship $h/\ell_o \sim P_e^{-1/2}$, a result in agreement with the observations of Crapper & Linden (1974), Fernando obtained $u_e/(\sigma_u)_o \sim P_e^{-1/2}$. This is clearly different from the R_i^{-1} behavior observed by Turner (1968). Denton & Wood (1981) suggested that at sufficiently large R_i, $u_e/(\sigma_u)_o \sim P_e^{-1}$ and that the R_i^{-1} behavior observed by Turner

occurs in a transition between the $R_i^{-3/2}$ and the P_e^{-1} regimes when $u_e/(\sigma_u)_o$ is plotted against R_i. In that work, Denton & Wood considered that the entrainment at sufficiently large R_i is predominantly due to molecular diffusion.

1.2.3.3 High Richardson Number Range

At very large R_i, Turner (1979) suggested that all mixing curves flatten out and become independent of R_i. Fortescue and Pearson (1967) showed that at very large R_i, $u_e/(\sigma_u)_o \sim P_e^{-1/2}$ in the context of gas absorption into a water surface. Turner (1979) suggested that their explanation of the $P_e^{-1/2}$ behavior, which uses a theory based on molecular diffusion into the large eddies of turbulence in the water, also seems appropriate for a very stable liquid-liquid interface. The $P_e^{-1/2}$ dependence is equivalent to stating that

$$u_e \sim \kappa/h, \tag{1.2.6}$$

with h given by

$$h \sim [\kappa\tau_o]^{1/2}, \tag{1.2.7}$$

where τ_o is the integral time scale of the turbulence near the density interface. In this case τ_o may be viewed as the time of

molecular diffusion between overturns.

To obtain $u_e/(\sigma_u)_o \sim P_e^{-1}$ at sufficiently high R_i when the entrainment is governed by molecular diffusion, Denton & Wood (1981) used (1.2.6) together with $h \sim \ell_o$ as observed by Crapper & Linden at high R_i when the stratification is due to salt. Denton & Wood also suggested that their model could be improved by allowing for a change in the interface thickness at low P_e as observed by Crapper & Linden. A consequence of such an improvement implies that the rate of entrainment changes from $P_e^{-1/2}$ to P_e^{-1} as P_e increases for sufficiently high R_i.

1.3 Goals of the Present Investigation

As evident from the discussion in Section 1.2, there is considerable confusion in characterizing the structure of turbulent density interfaces and the dynamics of mixing events. In particular, there are many discrepancies in measuring the thickness of the interfacial layer as defined by the temperature or salinity gradients. Moreover, the mechanisms leading to the instability of the interface and subsequent mixing, as well as the turbulence-internal wave interactions, are not very well understood. In order to clarify some of these points we undertake in this study the task of investigating in detail the nature of turbulent density interfaces by measuring the properties of turbulence near such interfaces, determining the characteristics of the internal

wavefield (amplitude, velocities, and spectra), and characterizing the mechanisms that lead to wave breaking and mixing. Moreover, we measure the interfacial layer thickness, the vertical mass flux, and investigate the evolution of mixing events. To achieve this, we use some relatively new non-intrusive techniques, namely laser-Doppler velocimetry and laser-induced fluorescence. Furthermore, the LIF technique is capable of providing both temporal and spatial resolution unattainable by conventional methods. We also aim at developing a simple model to aid in the prediction of turbulent mixing near a shear-free density interface.

CHAPTER 2

EXPERIMENTAL METHOD

The experiments described in this work can be divided into five categories:

(i) Turbulent velocity measurements in a homogeneous fluid.

(ii) Turbulent velocity measurements in and near a density interface.

(iii) Turbulent velocity measurements near a rigid flat plate in a homogeneous fluid.

(iv) Linear concentration measurements through a density interface.

(v) Flow visualization using laser sheet illumination.

The experimental procedure and equipment in each of these experiments is discussed below.

2.1 Tank and Grid

All experiments were carried out in a 3.35m deep glass-walled tank with a cross section of 1.15 x 1.15m. The tank was designed and built in the laboratory and construction details are given in Papanicolaou (1984). A schematic diagram of the experimental facility is shown in Figure 2.1. The oscillating grid, which consists of an array of rectangular bars 1.27 cm horizontal by 2.54 cm vertical, was placed in the upper portion of the tank as shown in Figure 2.1. The bars are placed on 6.35 cm centers thus yielding a

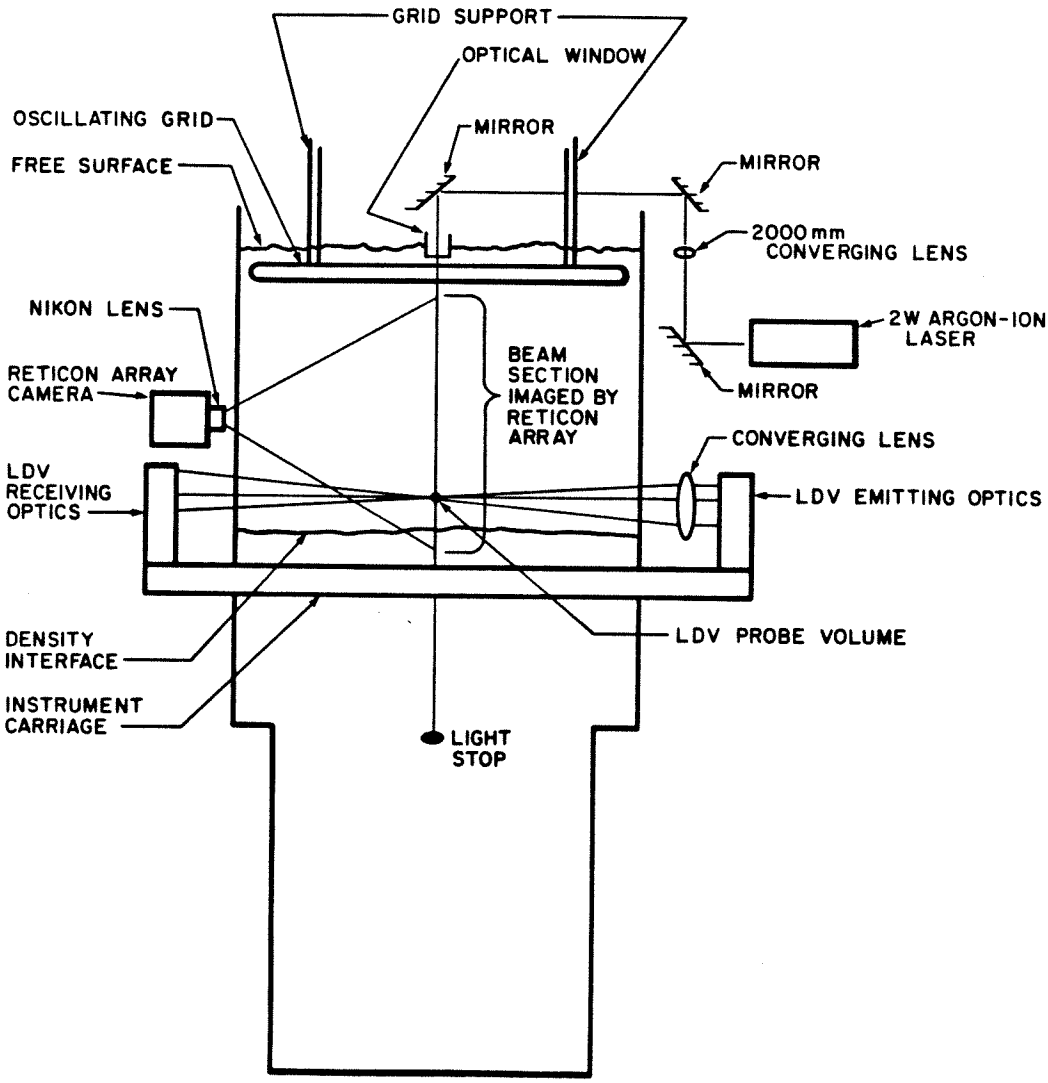

Figure 2.1: Schematic diagram of the tank, grid, and the optical layout

grid solidity of 36%. The grid solidity was chosen to be equal to that in previous investigations (Turner 1968, Hopfinger & Toly 1976, Fernando & Long 1983, Crapper & Linden 1974). A diagram of the oscillating grid is shown in Figure 2.2. The outside dimensions of the grid are 109.2 x 109.2 cm. The oscillating grid is supported by a rigid frame that is suspended from the laboratory ceiling in an attempt to minimize vibrations that may interfere with LDV and LIF measurements. A 3 hp DC motor is used to drive the oscillating grid via a reduction gear box. The rotary motion of the motor is converted to the vertical reciprocating motion of the oscillating grid by using an eccentric wheel and sliders. The tendency of the grid to move laterally was suppressed by the use of four rods guided by pillow blocks. A side view of the grid, eccentric drive, and guide rods is shown in Figure 2.3. The stroke of the grid motion was 6.35 cm with an oscillation frequency in the range of 2.12- 2.32 Hz. The frequency of the grid oscillation was chosen to be the maximum value attainable without causing excessive vibration problems. Due to the large size of the grid, a brace was needed to prevent the grid from excessive deformation. Four pieces of plexiglass, each being 69.9 x 15.2 x 1.27 cm, were glued together to form an open ended box. This box was glued to the top surface of the oscillating grid at a distance of 19.1 cm from each edge, with the 15.2 cm side being vertical and the 1.27 cm side being placed directly on top of a grid bar as shown in Figure 2.2. This resulted in a solid brace that did not alter the grid solidity. It is

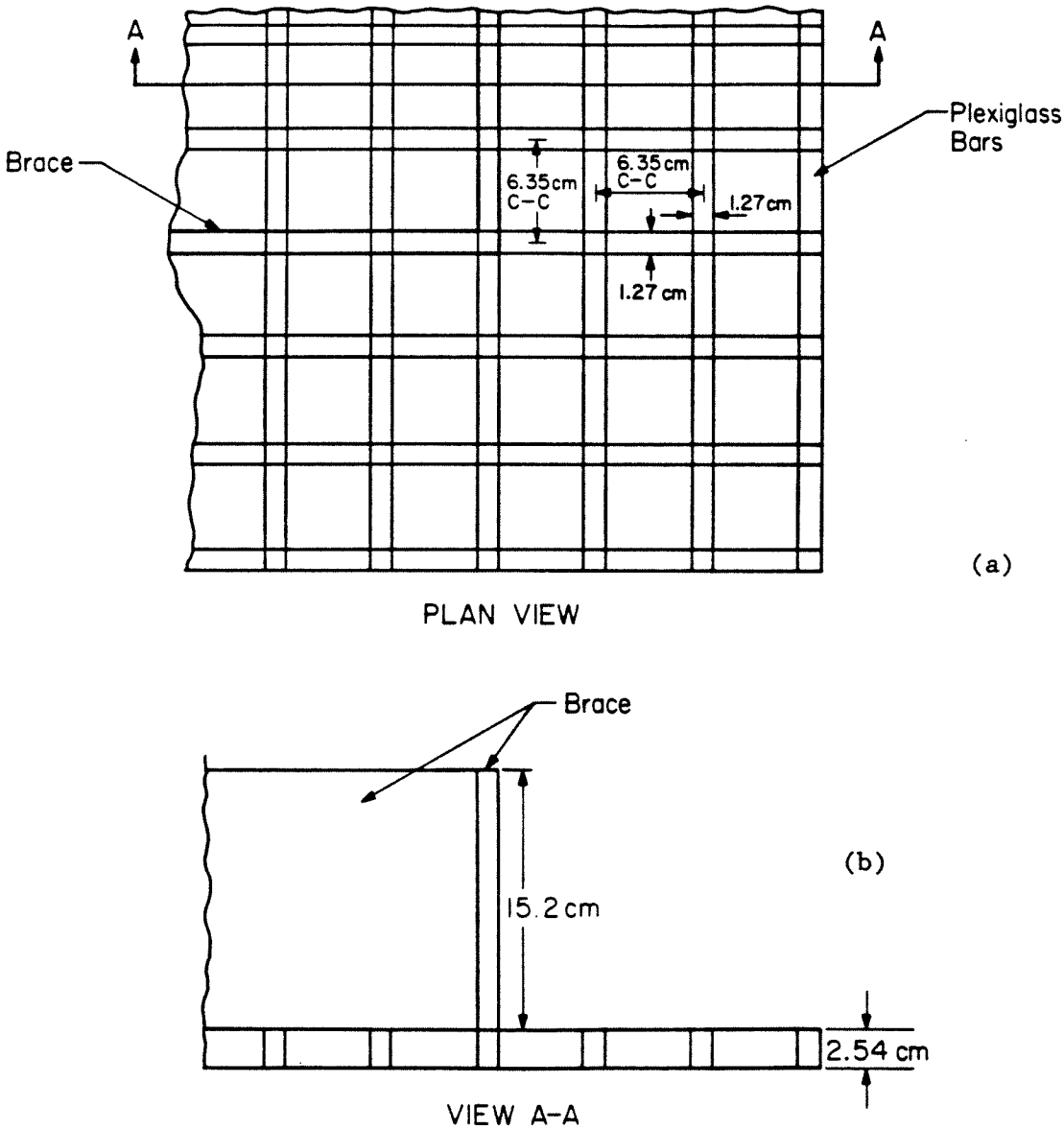

Figure 2.2: Details of the oscillating grid
(a) Plan View (b) View A-A

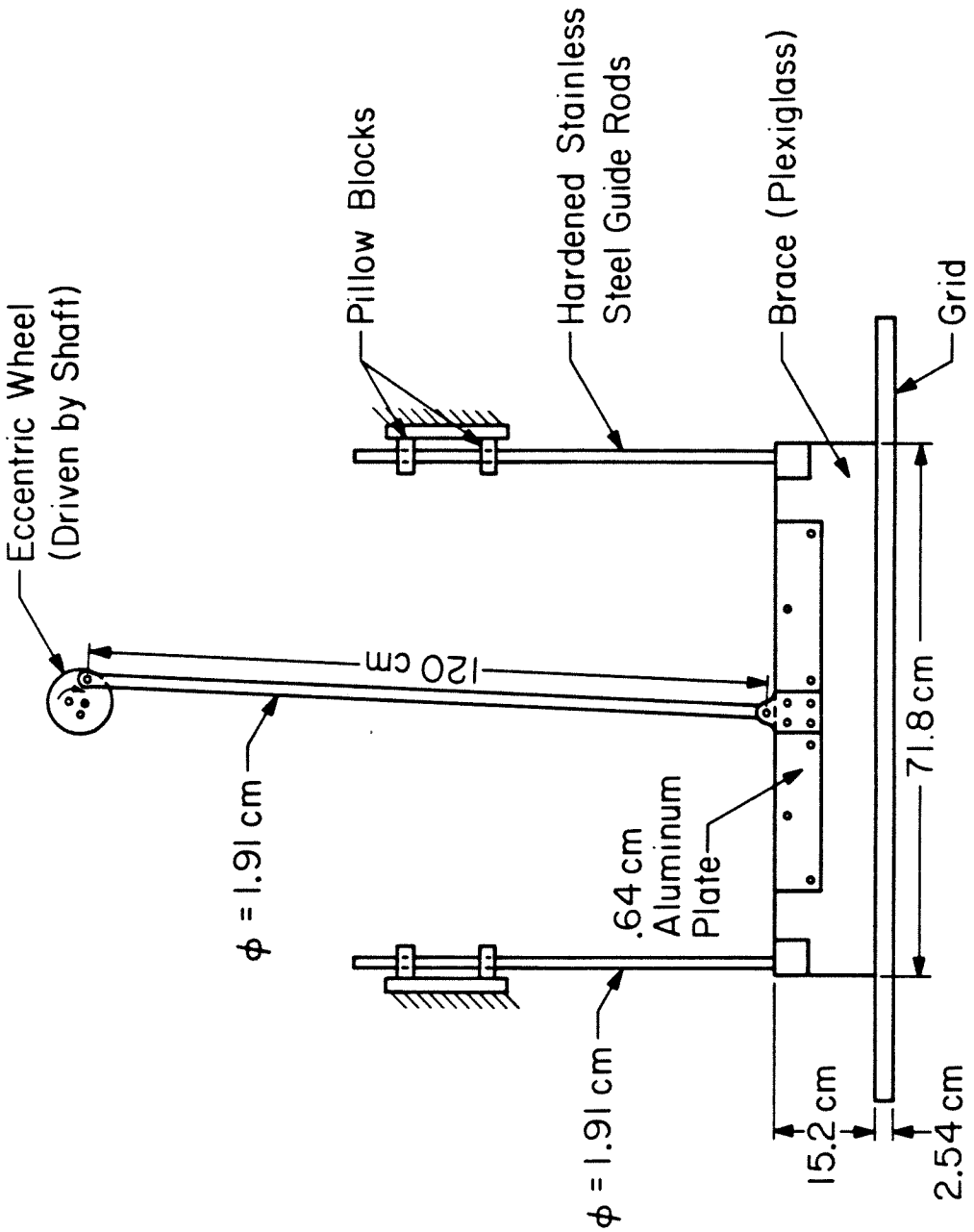

Figure 2.3: Side View of the grid, guide rods, and eccentric wheel driving mechanism

anticipated that the effect of the brace on the flow in the central parts of the tank is negligibly small.

2.2 Laser-Doppler Velocimeter System

A two-component LDV was used to measure the vertical velocity component and a horizontal component simultaneously at the same point in space. The transmitting and receiving optics of the LDV are mounted on a counter-weighted instrument carriage. The carriage is attached to the tank and provides both vertical and lateral movement (normal to the plane of Figure 2.1) for the instrumentation. The LDV employs a 7 mW He-Ne laser (Hughes model 3227H-PC) and uses a two reference beam system. The general optical layout is shown in Figure 2.1 and the details of the emitting optics are shown in Figure 2.4. The laser beams are split using prisms and are directed by a combination of mirrors and lenses to intersect in the middle plane of the tank. In order to discriminate the flow direction the frequencies of the laser beams are shifted by 88.889 kHz using two 40 MHz Bragg cells (Coherent model 305). The amplifiers used to drive the Bragg cells are model 300L RF Broadband Power Amplifiers manufactured by Electronic Navigation Industries Inc.. The electronics circuit for the Bragg cell exciters is shown in Figure 2.5. The length of the probe volumes are 3.6 mm and 8.0 mm for the vertical and horizontal velocity components respectively (Papanicolaou 1984). The Doppler shift obtained is 1132 Hz/cm/sec

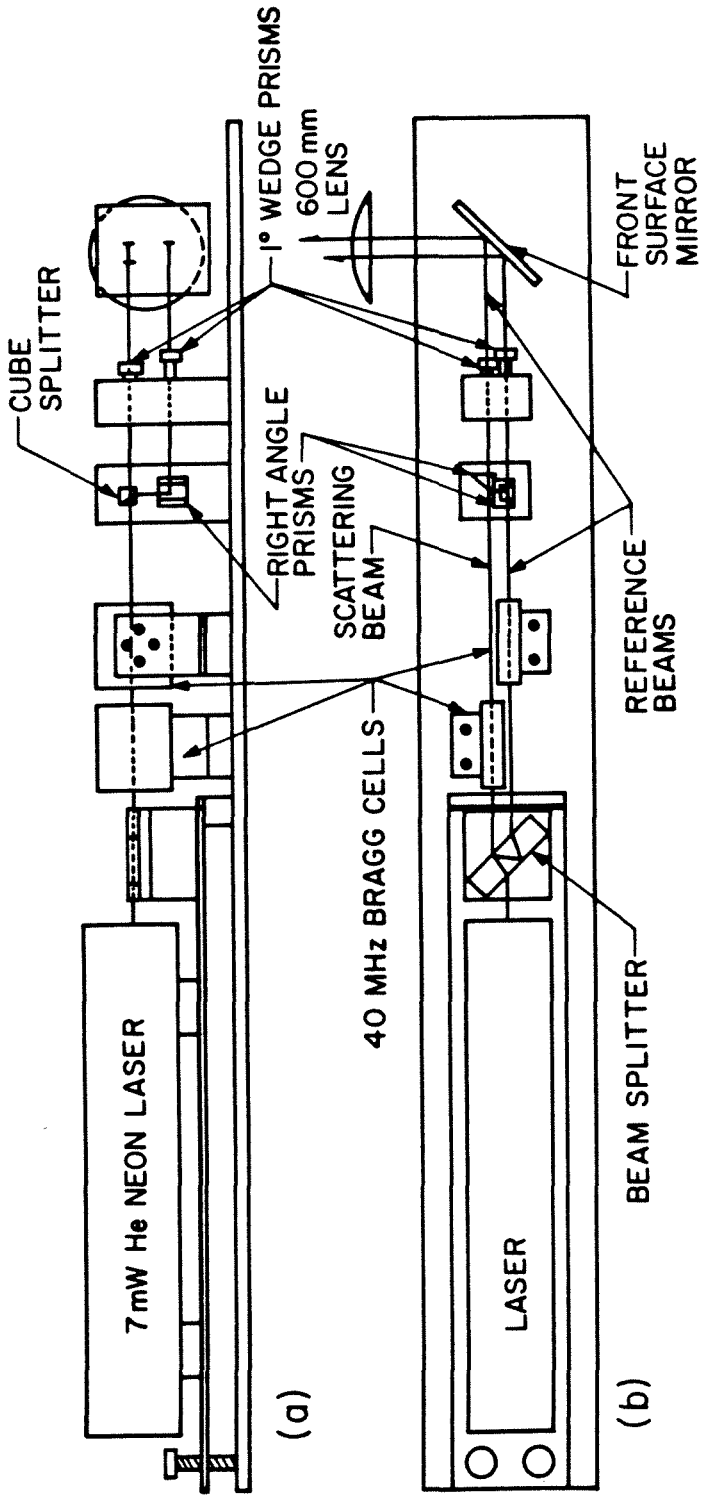

Figure 2.4: Schematic of the LDV emitting optics.
(a) Elevation (b) Plan (from Papanicolaou 1984)

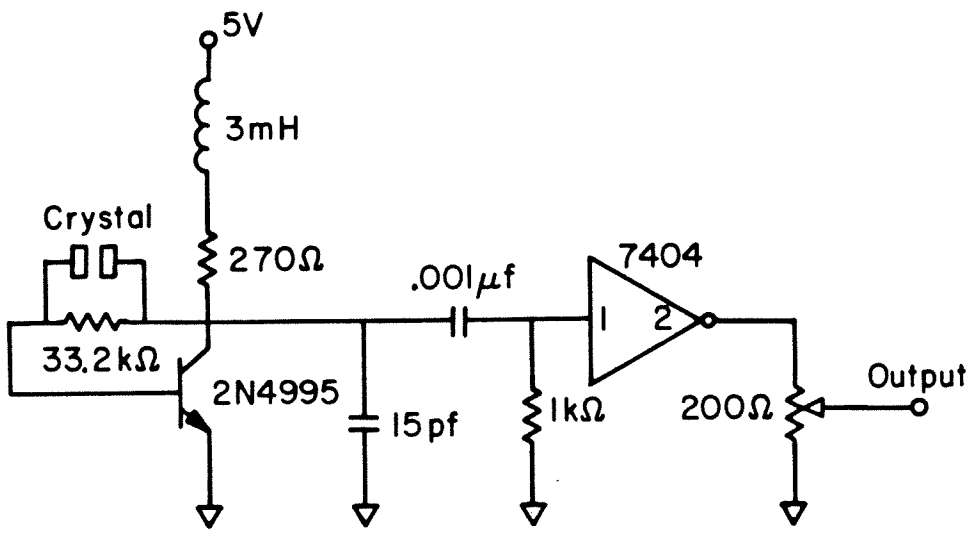

Figure 2.5: Electronic circuit for the Bragg cell exciters (from Papanicolaou 1984)

for the vertical component and 495.8 Hz/cm/sec for the horizontal component. Other details of the optical set-up are given in Papanicolaou (1984). The two reference beams and the scattering beam are focused onto two fast response silicon photodiodes (EG&G type DT-25) using two 12.5 cm converging lenses as shown in Figure 2.6.

It was found that the amount of particles present in the laboratory water supply system was adequate for velocity measurements. As a result, no seed particles were added to the water. The laboratory water was filtered using a commercial filter (Sears) that entrapped large particles present in the water supply. Details about the characteristics of particles present in the laboratory water supply are discussed in Papanicolaou (1984).

The pre-amplified signal outputs of the photodiodes are fed to two identical laboratory built signal processors. The signal processors are of the counter type and include electronic circuitry for the detection of Doppler bursts. A schematic of one of the signal processors and the data acquisition system is shown in Figure 2.7. The raw signal from the photodiodes is amplified and band pass filtered (Krohn-Hite model 3202 filter) at 80 and 100 kHz. The filtered signal is then fed to two parallel circuits: the first circuit is a zero crossing counter while the other parallel circuit is a validation circuit that reinitializes the counting if the signal falls below a certain preset threshold. This insures that

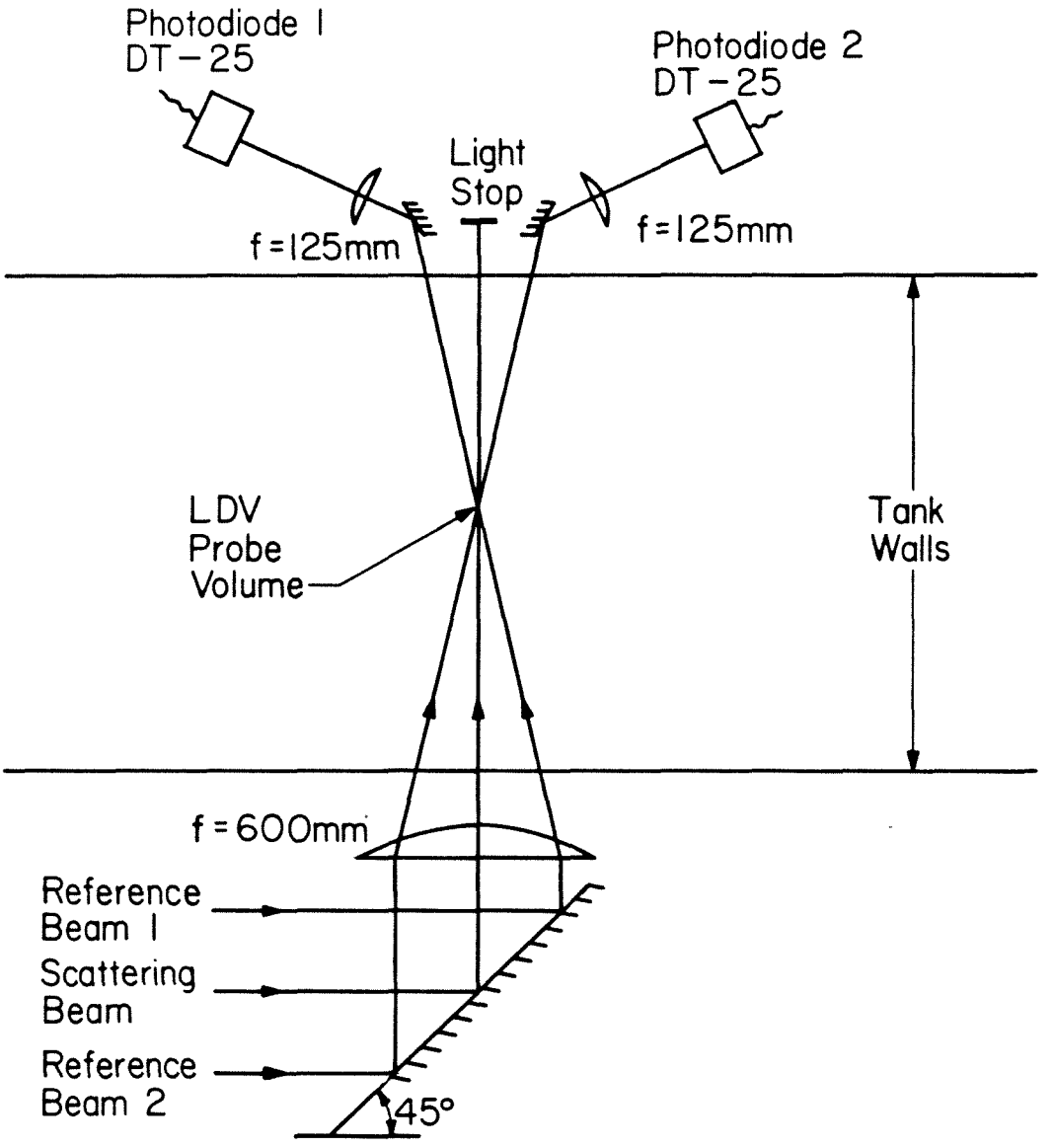

Figure 2.6: Plan view of the LDV receiving optics and the arrangement of the laser beams

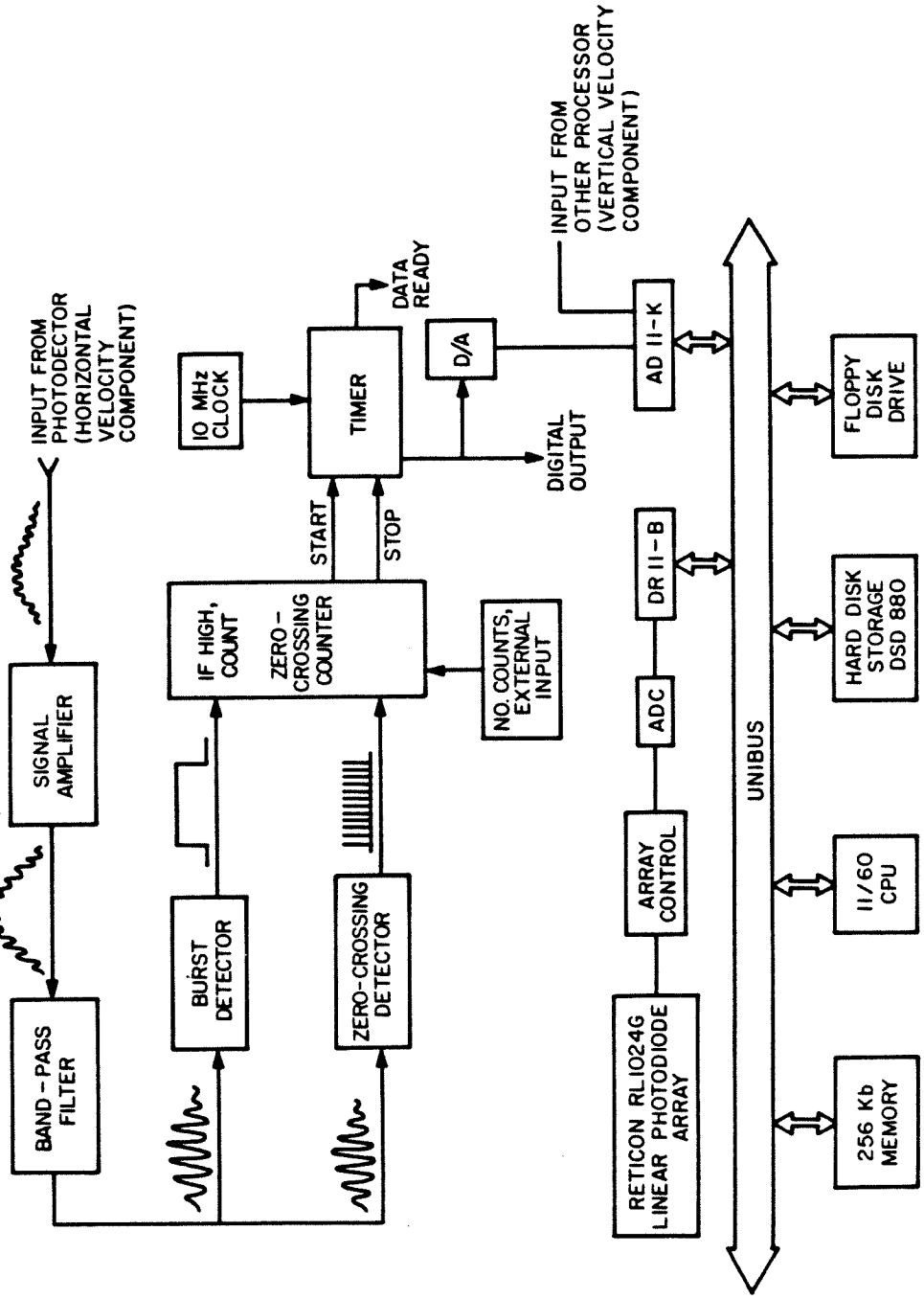

Figure 2.7: Schematic of the LDV processor, Reticon camera signal transmission, and layout of the data acquisition system

the only signals that are considered are due to particles passing in the central region of the probe volumes. The output of the signal processor is updated at a rate of about 200 Hz. Details of the signal processor are in Gartrell (1979b). The signal processors were calibrated before every experiment by using a sinusoidal signal generator with known input frequencies f_i that cover the range of the expected frequency output of the photodiodes during the course of an experiment. The corresponding analog output of the processor V_i was recorded by the computer. From the (f_i, V_i) pairs a least square fit of the form $f_a = A/V + B$ was determined where f_a is the estimated frequency output of the photodiodes, V is the analog output of the processors, and A and B are constants. Such a fit proved to be very accurate and the correlation coefficient was typically about 1.00002. After determining the constants A and B, f_a (and hence the Doppler shift $f_D = f_a - 88.889$) can be calculated from the above formula. The velocity is then obtained from f_D in a straightforward manner (*e.g.* Drain 1980, Durst *et al* 1976, and Watrasiewicz 1976).

2.3 Laser-Induced Fluorescence System

The method of measuring concentrations by LIF is becoming increasingly popular. In the last few years Papanicolaou (1984), Koochesfahani (1984), and Papantoniou (1986), among others, have successfully used this technique to obtain further insight on the

nature of mixing in turbulent flows. The technique, as used in this study, is based on the ability of Rhodamine 6G dye to fluoresce at wavelengths near 570 nm when exposed to a laser beam having a wave length of 514 nm. For a range of dye concentrations, the intensity of the emitted light is proportional to the concentration of the dye. This provides a non-intrusive method for measuring concentrations. The details of the method of concentration measurement by LIF will not be discussed here but a comprehensive discussion on this subject can be found in Liu *et al* (1977).

In our set-up the 514 nm line of a 2 W argon-ion laser (Spectra Physics model 265) is directed vertically downward by the use of a combination of coated front surface mirrors. The beam then passes through a small glass window placed at the free surface as shown in Figure 2.1. Before it enters the water the beam also passes through a 200 cm converging lens that is placed appropriately so that the beam is of nearly uniform thickness of about 0.5 mm in the test section. A section of the laser beam was imaged by an array of 1024 photodiodes (EG&G Reticon model RL1024G) after the original 514 nm line was filtered-out using an optical filter. The photodiode array is encased in an LC300A camera from EG&G. This camera is about the size of, and its operation is analogous to, an ordinary photographic camera, with the exception that the film is replaced by the photodiode array and its associated electronic circuitry. The array diodes are in a single row with a center-to-center spacing of 25 μm.

The aperture width of each pixel is 26 μm. The field of view of the camera depends on the lens selected and its distance away from the laser beam. The object resolution is therefore determined by the field of view. In our experiments a 50 mm f 1.8 Nikon lens was used and the LC300A camera was supported on a rigid surveying tripod. The imaged laser beam passes through the center of the tank and the camera was at a distance of 65-80 cm away from the beam thus giving a resolution of about 0.3-0.4 mm. The array was scanned by a sample and hold circuit controlled by a clock, which switches from diode to diode at an adjustable frequency ω_a. After scanning the last diode, there is an adjustable blanking period before sampling the first diode of the next scan. ω_a was supplied by a signal generator and was in the range of 85-110 kHz. The frequency at which data is available from each pixel is given by ω_a/count, where "count" equals the number of array diodes (1024) plus the blanking period clock cycles (fixed at 64 in this study). This gives a data output rate of about 80-100 Hz per pixel. However, due to the large amount of data generated and the limited disk storage volume, only a fraction of the available data was digitized and stored on a hard disk. Typically, we digitized every fourth scan thus yielding a frequency of about 20-25 Hz per pixel. Alternatively, we could have obtained these frequencies by using a smaller ω_a and digitizing every scan. However, large values of ω_a help in preserving the sharpness of the flowfield. A total of 5120 array scans were recorded in the experiments reported in Chapter 4.

The electronic circuitry included with the LC300A camera assembly consists of three boards. These are the array board, video processing board, and the interface board. The array board consists of an integration counter that determines the number of clock pulses between start pulses to the array. The video processing board consists of an integrator, sample and hold circuit, buffer amplifier, blanking pulse generator, reset pulse, integrate pulse, and sample pulse generators, while the interface board consists of a clock generator, regulator, data comparator, line drivers, and a line receiver. Other details of the circuitry are included in the Reticon LC300A manual (1981). The camera is driven by a ±15 V DC power supply.

The analog output of the camera has an amplitude of zero to 1.0 V. Dark noise is typically less than 10 mV, giving a dynamic range of 100:1. The analog output is digitized using a custom built A/D (details are in Papantoniou 1986) and then fed to a PDP 11/60 computer through a DMA interface as shown in Figure 2.7. A description of the data acquisition system is given in Section 2.8 and more details are in Papantoniou (1986).

Before experiments to measure concentration were carried out, a calibration was performed in order to account for the effects of lens aberration, variable beam width, and various imperfections such as distortions caused by the glass windows. Rhodamine 6G dye was mixed with dechlorinated water in the tank to yield a homogeneous

fluid with a known dye concentration. The beam was then focused onto the camera and the average output from 512 scans was recorded by the computer. A typical plot of the averaged camera calibration output is shown in Figure 2.8 as a function of the pixel number. After the calibration was over, special care was taken to insure that the camera was not touched until the experiment was over. Calibration curves such as the one in Figure 2.8 were used in correcting the raw data output from the Reticon array. The dye concentration during a calibration was determined so as to be within 10% of the dye concentration in an actual experiment. This was needed since the fluorescent light seemed to attenuate as it propagated through the fluid containing Rhodamine 6G on its way towards the photo-diode array. It is to be noted that this kind of attenuation is different from the attenuation of the original incident laser beam as it passes through the Rhodamine 6G solution. Within the range of dye concentrations used in this experiment, the attenuation of the fluorescent light was estimated to be less than 10% of the light received by the array. Another precaution that was taken to reduce the effects of fluorescent light attenuation was the positioning of the camera at a higher vertical position than the density interface. This was needed to insure that all the fluorescent light incident on the array passed through a homogeneous solution, *i.e.*, the upper mixed layer, and was therefore attenuated equally. By positioning the camera above the interface and using similar dye concentration values in both the calibrations and the

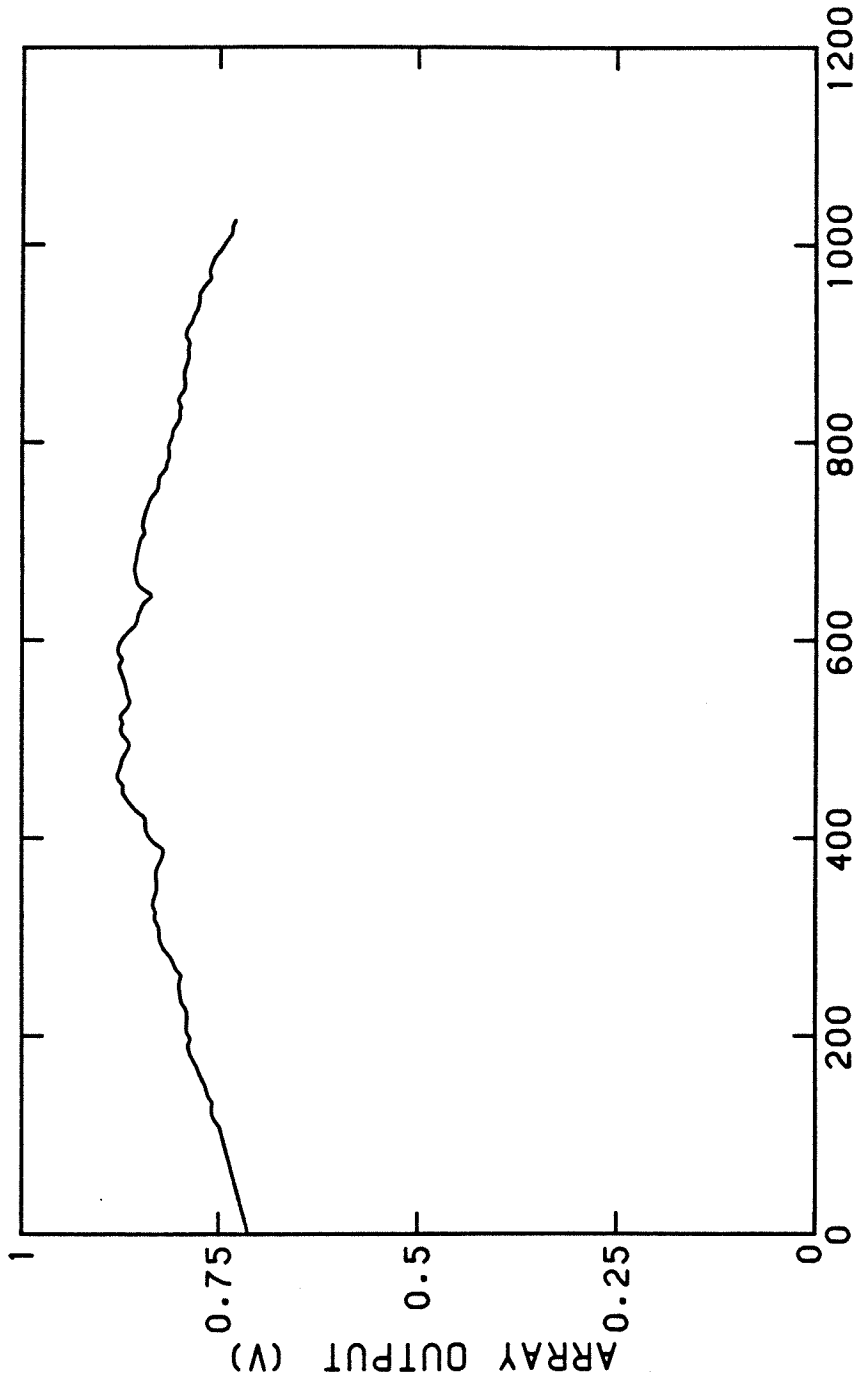

Figure 2.8: Typical calibration curve for the Reticon camera

experiments, errors due to the attenuation of the fluorescent light are limited to less than 1% of the values recorded by the array. Details of the use of the Reticon array camera are in Hannoun (1986).

2.4 Matching the Refractive Index

It is well known that index of refraction fluctuations create problems with LDV measurements. The consequences of these undesirable effects have been studied by McDougall (1979b) and Komori *et al* (1983). They concluded that, in general, the index of refraction fluctuations induce "pseudo turbulence" in the high frequency spectrum. To overcome this problem McDougall used two different solutes (sugar and Epsom salt) to obtain two fluids with different densities but with matching refractive indices. Due to the fact that our tank was more than eighty times the volume of the one used by McDougall, use of Epsom salt is not economical. Moreover, the choice of the solutes is limited so as to avoid the phenomenon of double diffusive convection, which introduces a stringent constraint on solute selection. After an exhaustive search, we have been successful in determining that the refractive indices can be matched while maintaining a significant density difference (up to 2.0%) by using ethyl alcohol and common salt as solutes in the upper and lower layers respectively. In this way, the phenomenon of double diffusive convection is overcome altogether

since both solutes are stably stratified. In any event, no double diffusion of the salt finger type was observed in any of the experiments. Furthermore, alcohol and salt are quite inexpensive and their molecular diffusivities are approximately equal. A hand refractometer (American Optics model AO 10419) was used to match the refractive indices of the two layers. The tank was covered by a sheet of plastic in order to minimize alcohol evaporation, which was observed to be negligible after the cover was installed. Other details of the method of matching the refractive index using salt and alcohol are in Appendix A.

2.5 Procedure in Density-Stratified Experiments

Prior to the start of an experiment involving density stratification two fluid volumes were prepared with salt and alcohol as solutes, respectively. After matching the refractive indices and insuring that the temperature difference between the layers was less than 0.1 ^{o}C, the aqueous alcohol solution (typically 2-3% alcohol by weight) was allowed to spread very slowly over the lower saline layer using a carefully designed manifold. The manifold consists of a perforated horizontal pipe placed at the top of the lower layer. The alcohol solution was fed to the pipe under gravity and the fluid that was forced out from the perforations formed a thin sheet and spread over the heavy layer. To avoid interfacial mixing, the filling process proceeded at a very slow rate and it took several

hours to stratify the tank. A schematic diagram of the tank plumbing system is shown in Figure 2.9.

In the two-layer stratified mixing experiments measurements were not started until the upper layer grew by at least 20% of its depth at the end of the stratification process. This was done in order to minimize the effects of any anomalies from the tank filling process. Due to the transient nature of the experiment, the depth of the upper mixed layer, referred to as D, is a slowly increasing function of time. However, we limited the maximum variation in D during any experiment to 12% of its value at the beginning of the experiment, thus minimizing the effect of the transient due to interfacial movement on R_i and other parameters. In the experiments involving velocity measurements at various distances away from the interface (Chapter 3), the velocities were measured at a fixed point in space while the interface was moving downward. Hence, measuring velocities at different times is equivalent to sampling velocities at different distances away from the density interface.

2.6 Flat Plate Experiments

Flat plate experiments were performed in a homogeneous fluid, the fluid being filtered tap water. The flat plate consisted of a 115 x 10.0 x 1.27 cm plexiglass plate which was placed in a position parallel to the grid at a distance of 21.2 cm away from the lowest point of the grid. At this position the width of the plate was

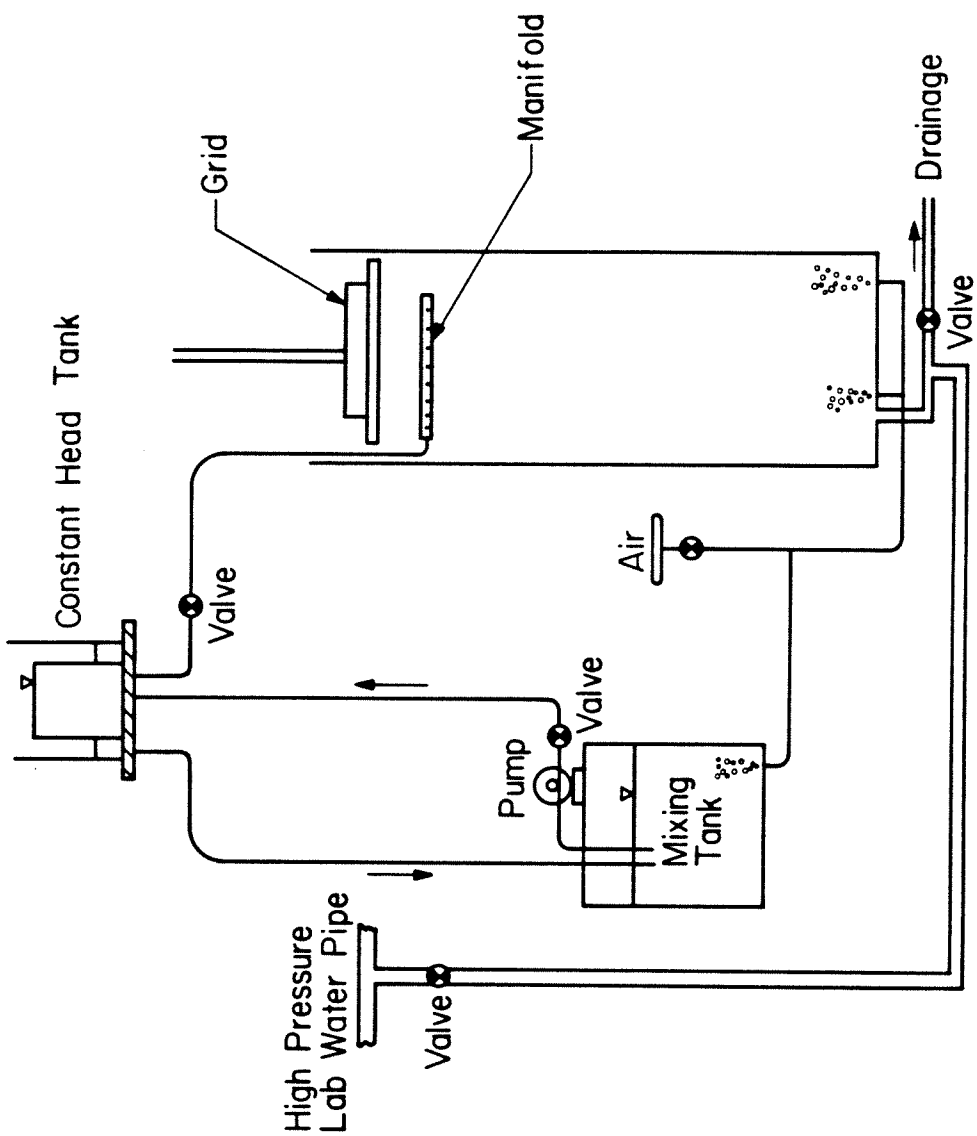

Figure 2.9: Schematic of the tank plumbing and stratification system

about five times the integral length scale of the turbulence. Since the velocities were measured in a plane equidistant from the edges of the plate, effects due to the finite width of the plate can be considered to be minimal.

2.7 Laser Sheet Illumination

Visualization of the flow field in the presence of a density interface was done by illuminating the flow with a sheet of laser light about 0.5 mm thick and with fluorescent dye added to the upper mixed layer. The sheet of laser light was obtained by expanding the 514 nm laser beam from the 2 W argon-ion laser using a cylindrical lens. The advantage of this method of planar illumination is in the preservation of the flow detail that is masked when the visualization method averages over the depth of the flow. Pictures using a 35 mm camera and Kodak ASA 400 film with shutter speeds of 1/250 seconds were obtained. Moreover, extended flow visualization was carried out by taking 16 mm movie films.

2.8 Data Acquisition and Processing

The analog output of the LC300A camera was digitized using a custom made analog-to-digital converter (Papantoniou 1986) and then fed to a PDP 11/60 computer through a DMA interface. The data was recorded on a DSD 880 Winchester disk as shown in Figure 2.7. The data acquisition program was based on an assembly language

subroutine that maximized the efficiency of the process. The program also sampled two AD11-K analog-to-digital converter channels that were connected to the analog outputs of the two LDV signal processors. These two AD11-K channels were sampled synchronously at the end of each array scan. Thus, the velocities were also sampled at rates of 20-25 Hz. It is to be noted that no mechanism was used to insure the arrival of both velocity signals at the same time. However, the new data update rate was about 200 Hz. As a result, we can deduce that both components of velocity are measured within about .005 sec. This should not have a significant effect on velocity correlations. Other details about the data acquisition process are given in Papantoniou (1986).

In the experiments that involved long velocity measurements (Chapter 3), LIF measurements were used for the sole purpose of locating the position of the density interface relative to the point where the velocities were measured. Due to the large amount of data generated and the finite disk storage volume, we were limited in sampling concentrations before the beginning and after the end of the velocity measurements. Each of the concentration sampling intervals lasted for 90 seconds. From these two concentration records the mean position of the interface was determined at two distinct time intervals. Intermediate interfacial positions were obtained by interpolation according to the relationship $u_e/(\sigma_u)_o \sim R_i^{-3/2}$.

After the data were recorded on magnetic media, they were transferred to a PDP 11/24 and a VAX 750 computer where all data reduction was done. The LIF data were corrected by taking into account the calibration curve as discussed in Section 2.3. The data were also corrected for the attenuation of the laser beam as it passes through the Rhodamine 6G solution by using a relationship of the form

$$I = I_0 \, e^{-\int_0^{X_3} \epsilon C dx_3}, \qquad (2.1)$$

where I is the intensity of the laser beam after it traverses a distance x_3 in the fluid, I_0 is the initial intensity of the laser beam at $x_3 = 0$, C is the dye concentration, and ϵ is the dye absorption coefficient. The laser beam attenuation is actually determined by replacing the integral in the last formula with a summation and using the values of C as obtained from the array output. The details of the method of correction for attenuation are discussed in Koochesfahani (1984). The maximum correction due to beam attenuation was kept to below 20% by using sufficiently low dye concentrations. Moreover, due to the fact that the dye concentration away from the interface is almost constant, large errors resulting from miscalculating the attenuation can be detected. The determination of the constant ϵ is outlined in Appendix B and other details of the data reduction process are in Papantoniou (1986). Some of our LIF data were displayed at an image

processor at the Graduate Aeronautical Laboratories at Caltech.

CHAPTER 3

CHARACTERIZATION OF THE VELOCITY FIELD

In this chapter, we report the details of an experimental investigation on the nature of turbulence near a density interface. We start by studying the characteristics of the turbulence generated by the grid and measuring its spatial evolution. Following that, we discuss the effects of the density interface on the turbulence properties and compare these effects to those of a rigid flat plate inserted in the flow. We also discuss the significance of the findings and attempt to answer questions concerning the applicability of the rapid distortion theory in situations where there is no mean flow (Hunt 1984) and near sharp density interfaces.

3.1 Measurements in a Homogeneous Fluid

In this section we will briefly present turbulent velocity measurements in a homogeneous fluid. Although other authors have already reported similar measurements we feel that these results constitute an important reference for comparison with measurements across a density interface and near a rigid flat plate. Moreover, we report here values of the velocity correlation coefficients, kinetic energy fluxes, and spectra that have not been previously measured. The grid oscillation frequency for all the experiments reported in this chapter was fixed at 2.20 Hz. In Figure 3.1 the

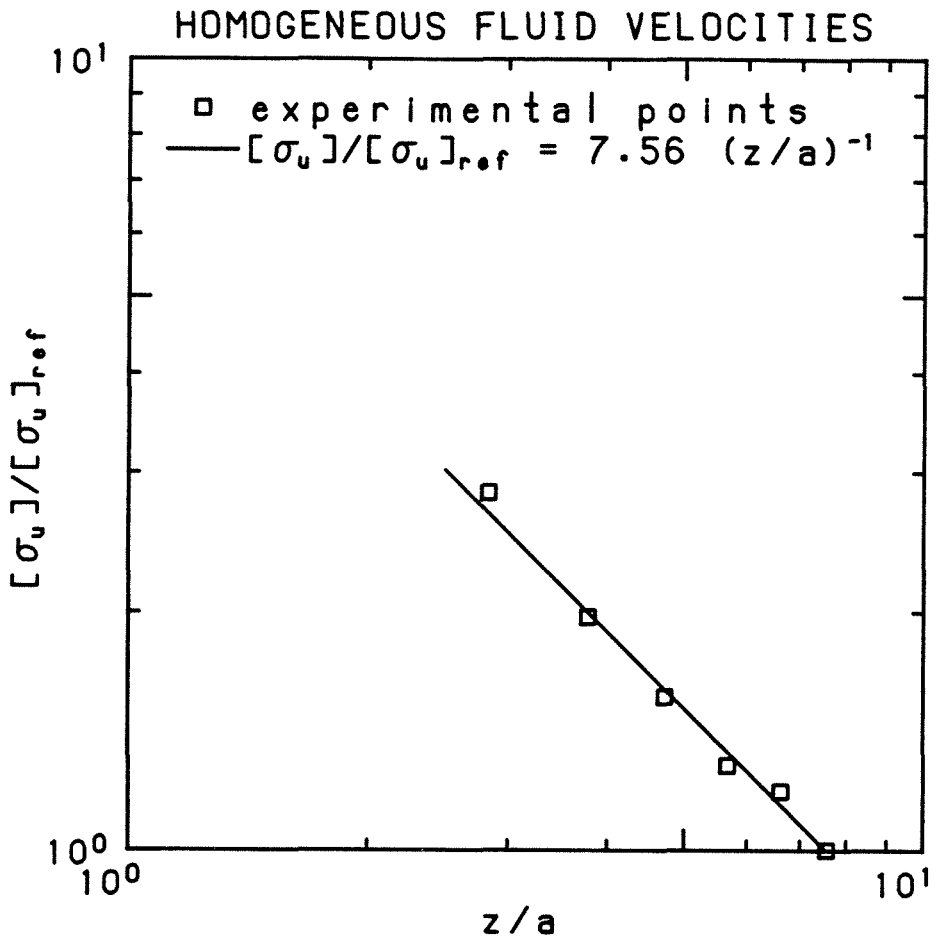

Figure 3.1: Variation of the non-dimensional r.m.s. horizontal velocity with non-dimensional distance away from the grid.
$[\sigma_u]_{ref}$ = 0.38 cm/sec; a = 3.18 cm

measured r.m.s. horizontal turbulent velocities * $[\sigma_u]$ are plotted in non-dimensional form against z/a, where z is a distance away from a virtual origin coinciding with the lowest position of the grid and a is the amplitude of grid oscillation. The virtual origin was determined from the ordinate intercept when z_a, a vertical distance away from an arbitrary origin, is plotted against $1/[\sigma_u]$ and a least-square line is fitted to the data. It can be seen from Figure 3.1 that a law of the form $[\sigma_u] \sim 1/z$ satisfactorily describes the data. Actually, a different choice of the virtual origin will yield a different dependence of $[\sigma_u]$ on z. However, the homogeneous fluid measurements will only be used in the rest of this study as a bench-mark for comparison with measurements near a density interface and a rigid flat plate. It is also worth noting that the virtual origin for the vertical r.m.s. velocity, $[\sigma_w]$, independently obtained in a similar fashion, is within 1 mm of the virtual origin for $[\sigma_u]$. Moreover, $[\sigma_w]$ also satisfies a law of the form $[\sigma_w] \sim 1/z$. The spatial averaging procedure is used to compensate for the measured variation of σ_u and σ_w in a horizontal plane. The variation in σ_u in a horizontal plane has a standard deviation of 5% of $[\sigma_u]$ at $z/a = 6.60$. The spatially averaged correlation

---

* Throughout this paper, the brackets [ ] represent a spatial average in a horizontal plane along a straight line. In all homogeneous fluid measurements without the rigid plate, thirteen points in the central region of the tank separated by 1 cm were used for the averaging. Also, an overbar denotes time averaging.

coefficient, $[\overline{u'w'}/\sigma_u\sigma_w]$, where u' and w' are fluctuating horizontal and vertical velocities, respectively, is -0.023 with a standard deviation of .07 at z/a = 6.60. More details about the horizontal inhomogeneities in velocity are given in Appendix C. The average value of $[\sigma_w]/[\sigma_u]$ is 1.32 for six values of z/a ranging from 2.80 to 7.60. This is slightly higher than the value of 1.2 measured by Hopfinger & Toly (1976).

From simultaneous measurements of u' and w' at the same point, we can obtain the vertical kinetic energy flux term $[\overline{q^2w'}]$, where $q^2 = 1/2\ (u'^2 + v'^2 + w'^2)$. In doing so we make an additional assumption that $[\overline{v'^2w'}] = [\overline{u'^2w'}]$, where v' is the fluctuating horizontal velocity component in a direction normal to that of u'. This assumption is needed since we do not measure v' and it is justified on the basis that there is no apparent reason why the time averaged statistics in the direction of v' should differ from those in the direction of u', considering the one dimensional nature of the turbulent energy propagation and the geometry of the experimental configuration. Accordingly, we will take $q^2 = 1/2\ (2u'^2 + w'^2)$. Hopfinger & Linden (1982) have assumed a relationship of the form $\overline{q^2w'} \sim \sigma_u^3$ for turbulence generated by an oscillating grid. To test the validity of such a relationship we plot $[\overline{q^2w'}]^{1/3}/[\sigma_u]$ versus z/a as shown in Figure 3.2. From Figure 3.2 it seems that $[\overline{q^2w'}]^{1/3}/[\sigma_u]$ is a constant function of z/a if we take into account that the estimated error in $[\overline{q^2w'}]$ is about 15% of

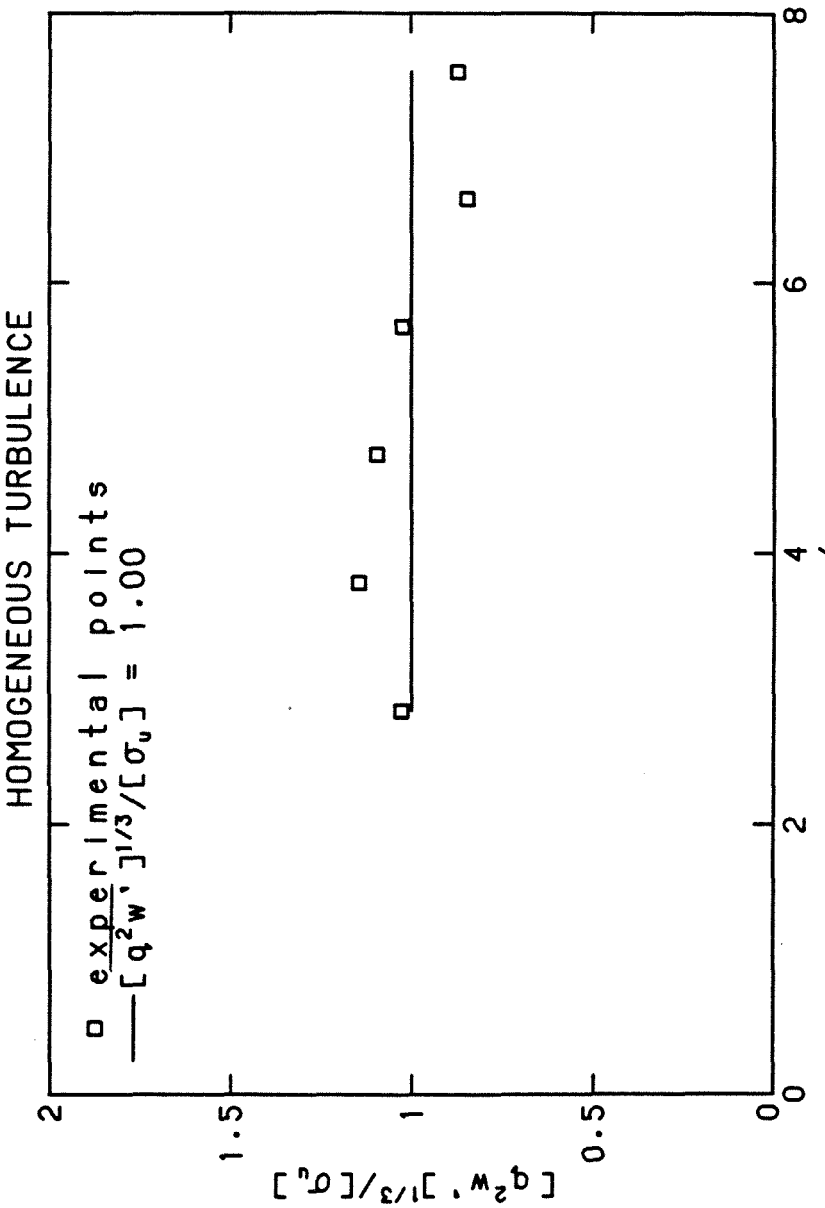

Figure 3.2: Variation of $\overline{[q^2w']}^{1/3}/[\sigma_u]$ with non-dimensional distance away from the grid

its value.

The integral time scale of the turbulence τ, defined as the area under the vertical velocity autocorrelation coefficient curve, was found to be well represented by a function of the form $[\tau]/[\tau]_{ref} = 0.0175[z/a]^2$ (where $[\tau]_{ref}$ is the value of $[\tau]$ at $z/a = 7.70$) as shown in Figure 3.3. Thus, if we define the integral length scale of the turbulence as $L = [\tau][\sigma_w]$, then we obtain $L \sim 0.1\ z$ for our experiments. It is worth noting here that L is different from the integral length scale ℓ used by some other investigators. The main difference is that ℓ is directly obtained as the area under the autocorrelation coefficient curve when measurements with a rotating probe are made. However, since our velocity measurements were obtained at a fixed point, the area under the velocity autocorrelation coefficient curve represents an integral time scale.

The Reynolds number, $R_e = [\sigma_w^2][\tau]/\nu$, is plotted against z/a in Figure 3.4. We notice that R_e is almost constant and does not show any significant trend for different values of z/a. In Figure 3.5, we present a power spectrum of the vertical velocity fluctuations at $z/a = 6.60$. It is possible to observe a range where the spectrum decays as $f^{-5/3}$ which seems to follow a prediction of the spectral decay in the inertial subrange by Tennekes (1975) in the absence of a mean flow.

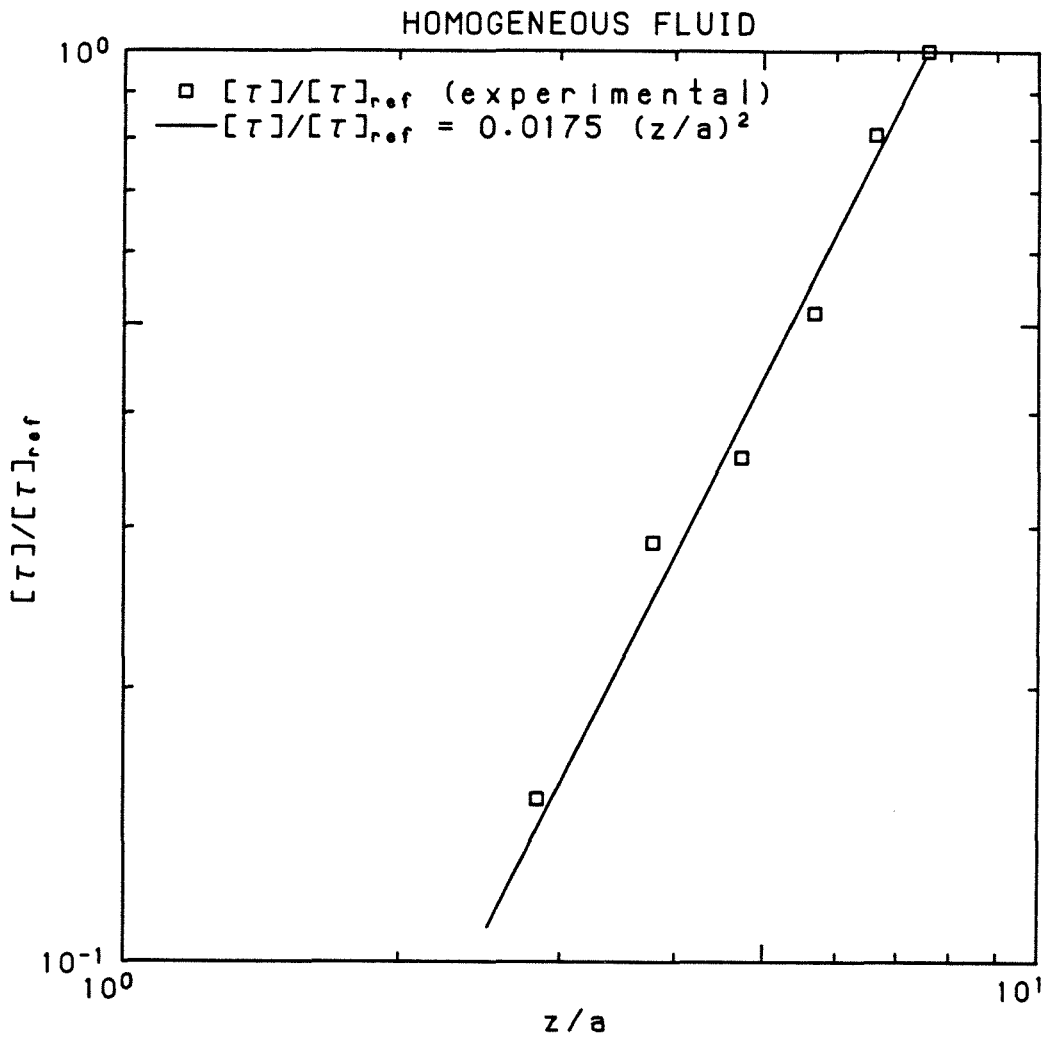

Figure 3.3: Variation of the integral time scale of the turbulence with distance away from the grid. $[\tau]_{ref}$ = 4.1 sec

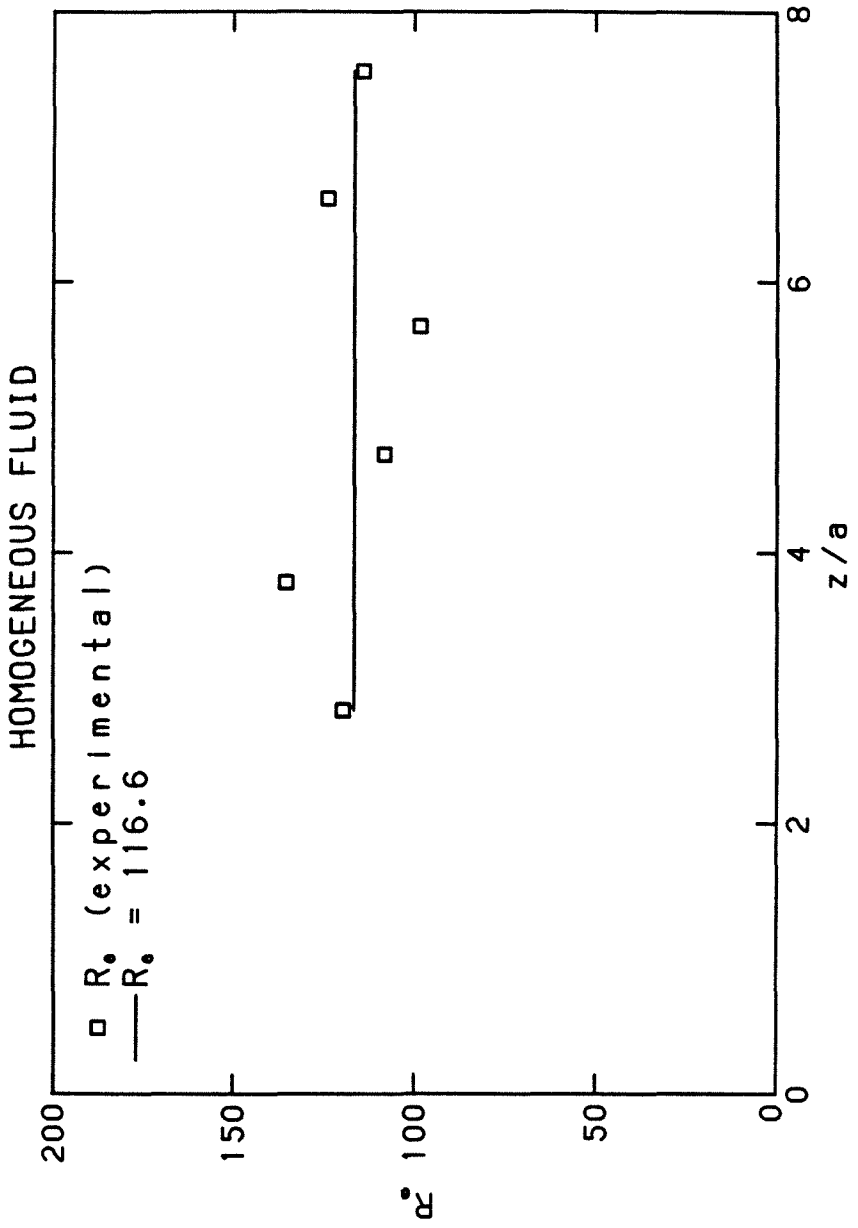

Figure 3.4: Variation of the Reynolds number R_e with distance away from the grid

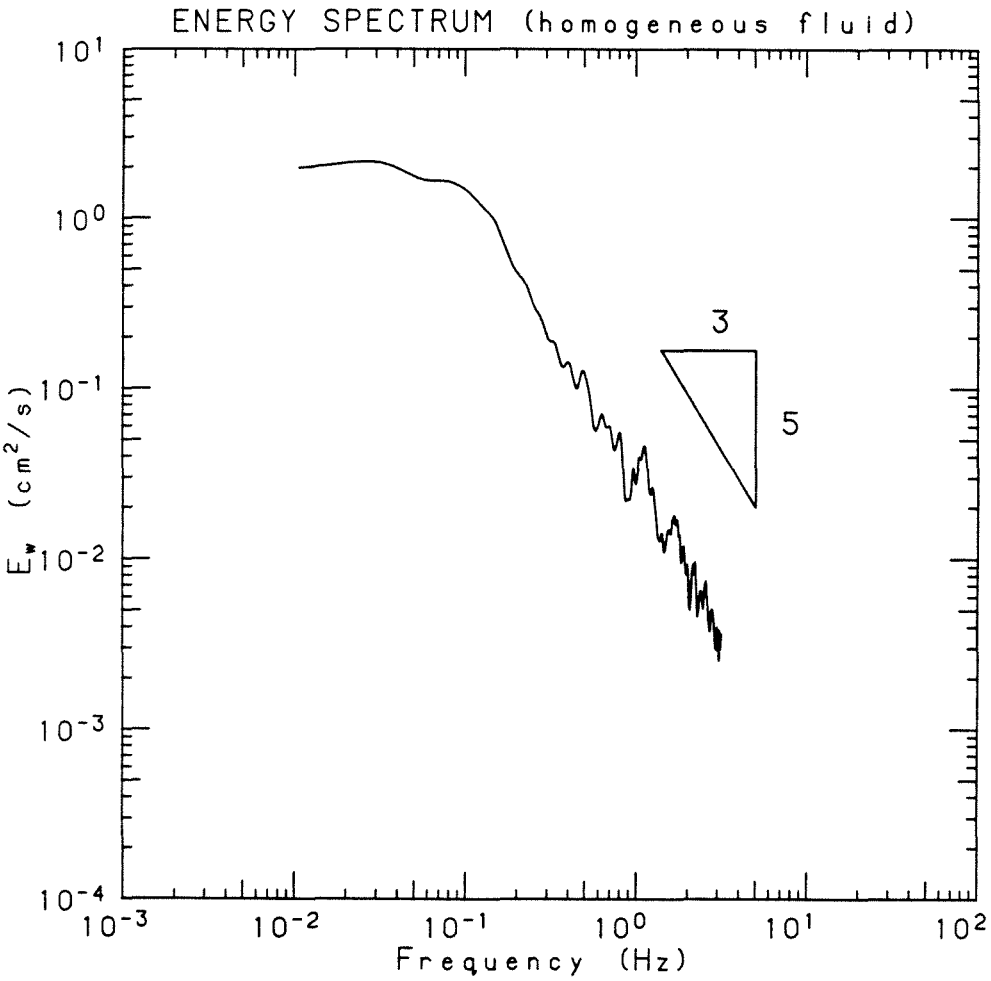

Figure 3.5: Energy spectrum of the vertical velocity fluctuations in a homogeneous fluid. z/a = 6.60

3.2 Measurements in Density Stratified Fluids

As discussed in Section 2.5, the velocity measurements in the experiments with a density interface were performed at a fixed point in space with the interface migrating very slowly. The time trace of velocity is divided into several segments and the position of the mean interface relative to the measuring volume is calculated for each segment by interpolation as pointed out in Section 2.8*. The experimental conditions in the experiments involving velocity measurements near a density interface are presented in Table 3.1. In Figures 3.6a and 3.6b, we plot normalized values of σ_u and σ_w, the horizontal and vertical r.m.s. components, respectively, as a function of ξ/L_o where ξ is a vertical distance measured from the mean density interface. From both Figures 3.6a and 3.6b, which correspond to two different values of the stability parameter R_j, where $R_j = \Delta b\ L_o/[\sigma_u]^2_o$, we notice that $\sigma_u/[\sigma_u]_o$ is amplified, whereas $\sigma_w/[\sigma_w]_o$ shows a monotonic decay as the interface is approached. These measurements indicate that there is a transfer of energy from the vertical component to the horizontal components, thus rendering the turbulence strongly anisotropic. It is also apparent from Figures 3.6a and 3.6b that the effects of the density interface extend to about $\xi/L_o \sim 1$. Figure 3.7a shows the energy

* The position of the interface for each data segment is defined as the mean over the data segment of the vertical position of the point at which the dye concentration is one half of its value in the mixed layer.

Table 3.1

Conditions for the experiments involving velocity measurements near a density interface

Experiment number	L_o (cm)	f_g (Hz)	$[\sigma_u]_o$ (cm/sec)	$\Delta\rho$ (gm/cm^3)	R_j
1	1.90	2.20	0.50	0.00919	70
2	2.21	2.20	0.42	0.00824	100

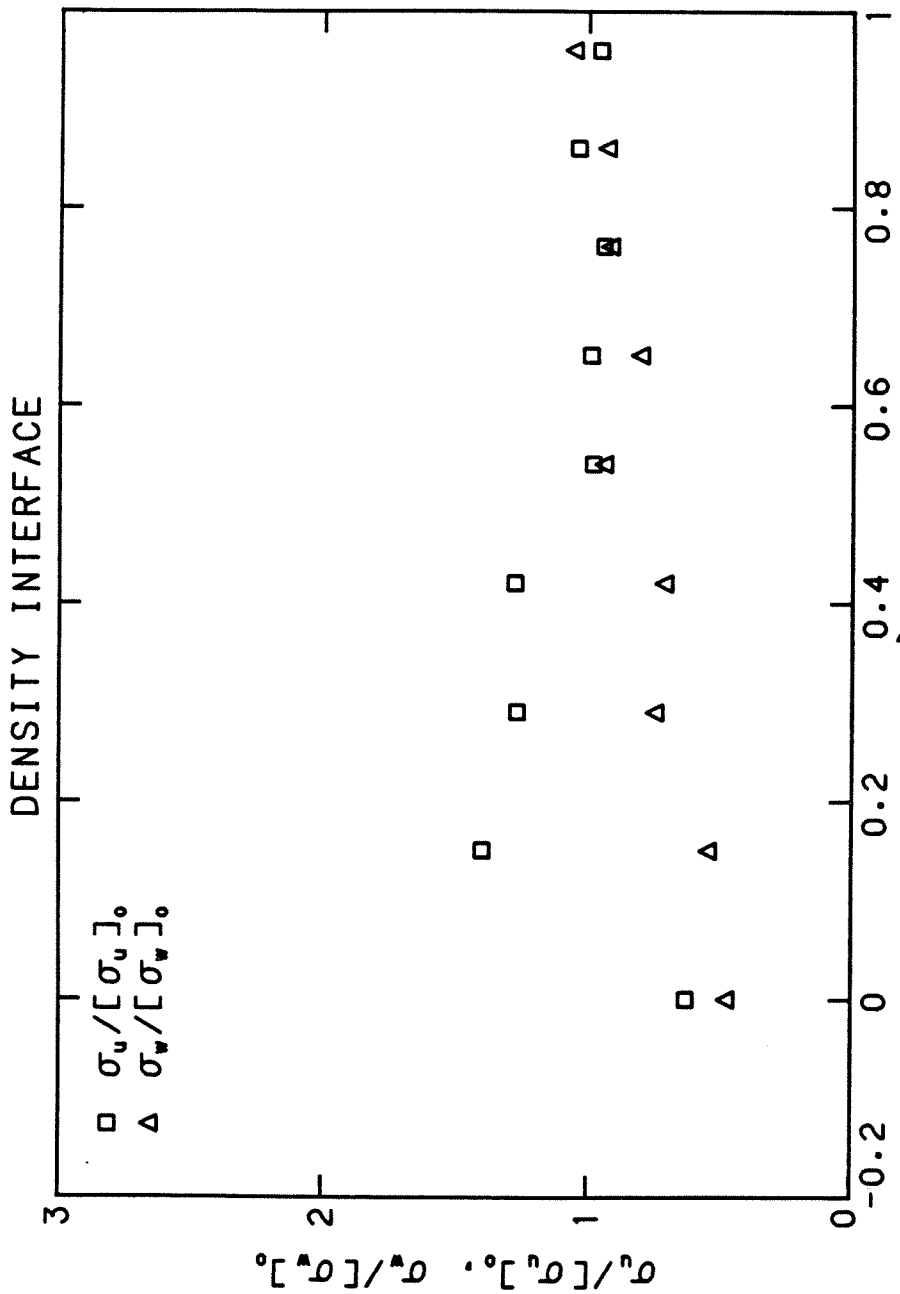

Figure 3.6a: Variation of the horizontal and vertical r.m.s. velocities with distance away from the interface. Experiment #1

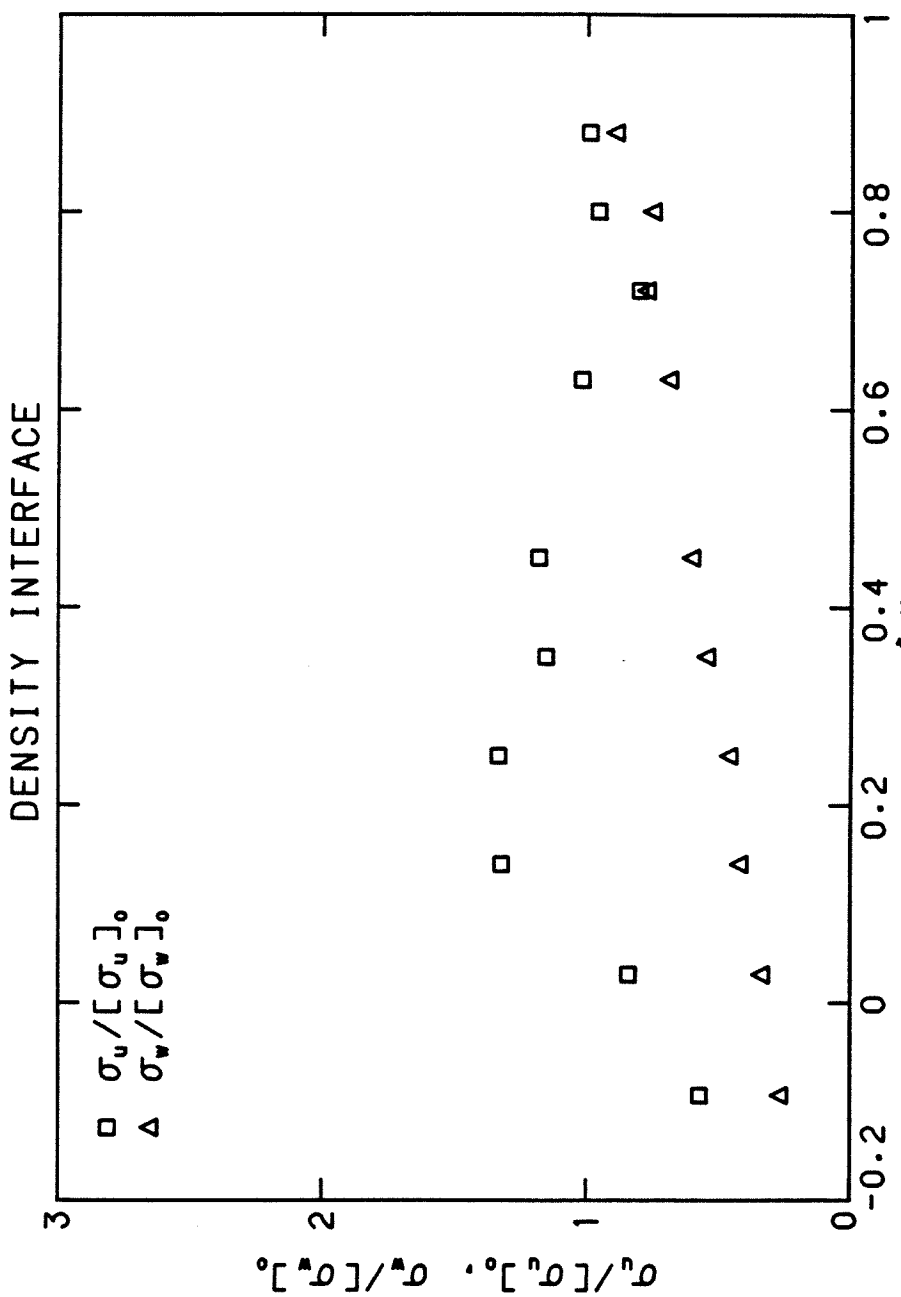

Figure 3.6b: Variation of the horizontal and vertical r.m.s. velocities with distance away from the interface. Experiment #2

spectra of the vertical velocity fluctuations E_w for various non-dimensional distances ξ/L_o away from the density interface, whereas Figure 3.7b gives the energy spectra of the horizontal velocity fluctuations. From Figure 3.7a we observe that there is preferential attenuation of low frequencies (large scales) as we approach the interface implying that the density interface has a significant influence on the large eddies. The power spectra of the horizontal velocity fluctuations in Figure 3.7b indicate that there is a net energy gain at the low frequency end of the spectrum (large scales) as the density interface is approached. Moreover, the high frequency ends of all spectra remain virtually unaffected, implying that the net transfer of turbulent kinetic energy from the vertical to the horizontal components is confined to small eddy frequencies or large eddy scales.

It is of interest to see how the profiles of both vertical and horizontal turbulence intensities affect the distribution of the turbulent kinetic energy near the density interface. If we plot the normalized total turbulent kinetic energy per unit mass, $\overline{q^2}/[\overline{q^2}]_o$, against ξ/L_o as shown in Figure 3.8 we notice that the values of $\overline{q^2}/[\overline{q^2}]_o$ are less than 1 for ξ/L_o between about 0.5 and 1.0. A similar result was obtained by HG for the case of shear-free turbulence near a rigid boundary. They explained that the decrease in the energy of the turbulence as being due to a rise in the mean pressure. Very close to the flat plate, HG predict that the energy

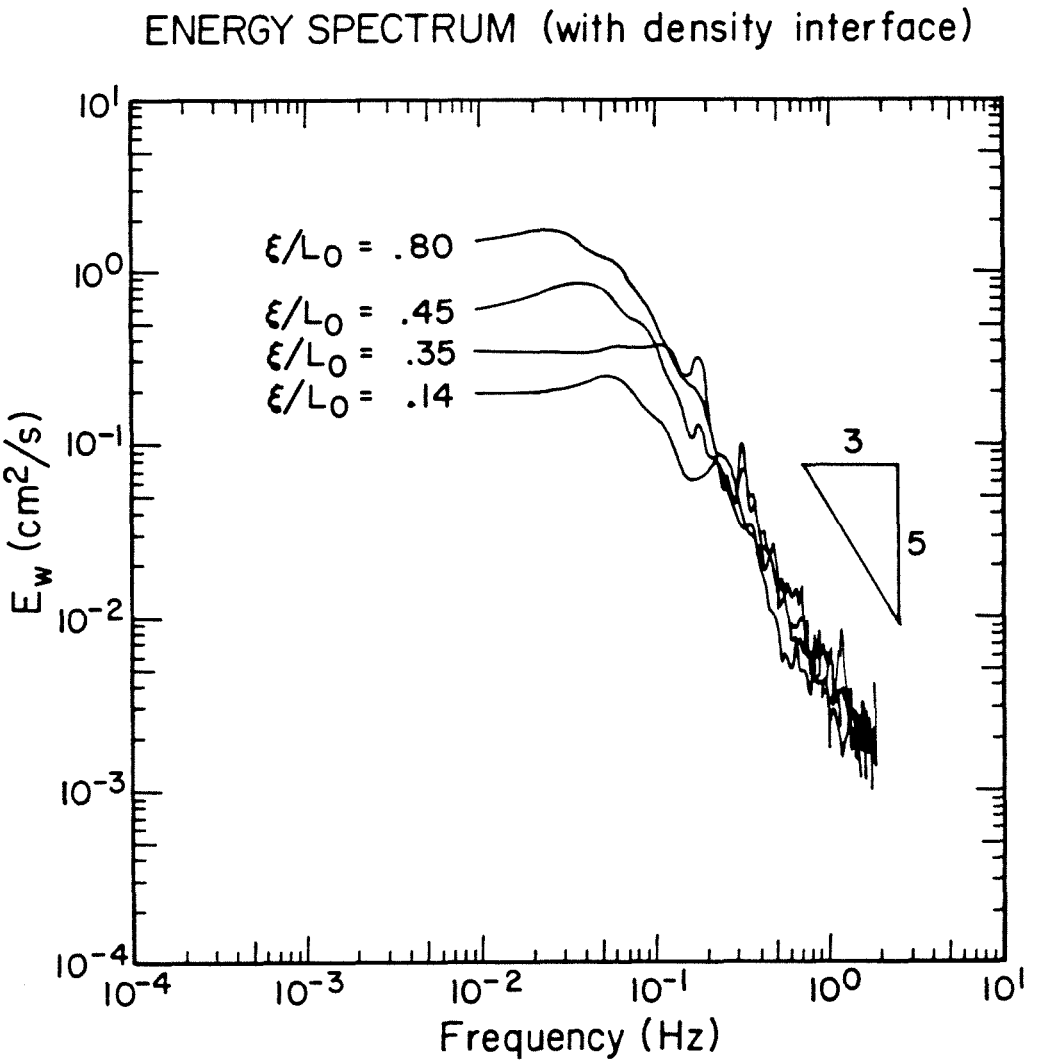

Figure 3.7a: Energy Spectra of the vertical velocity fluctuations near the density interface. Experiment #1

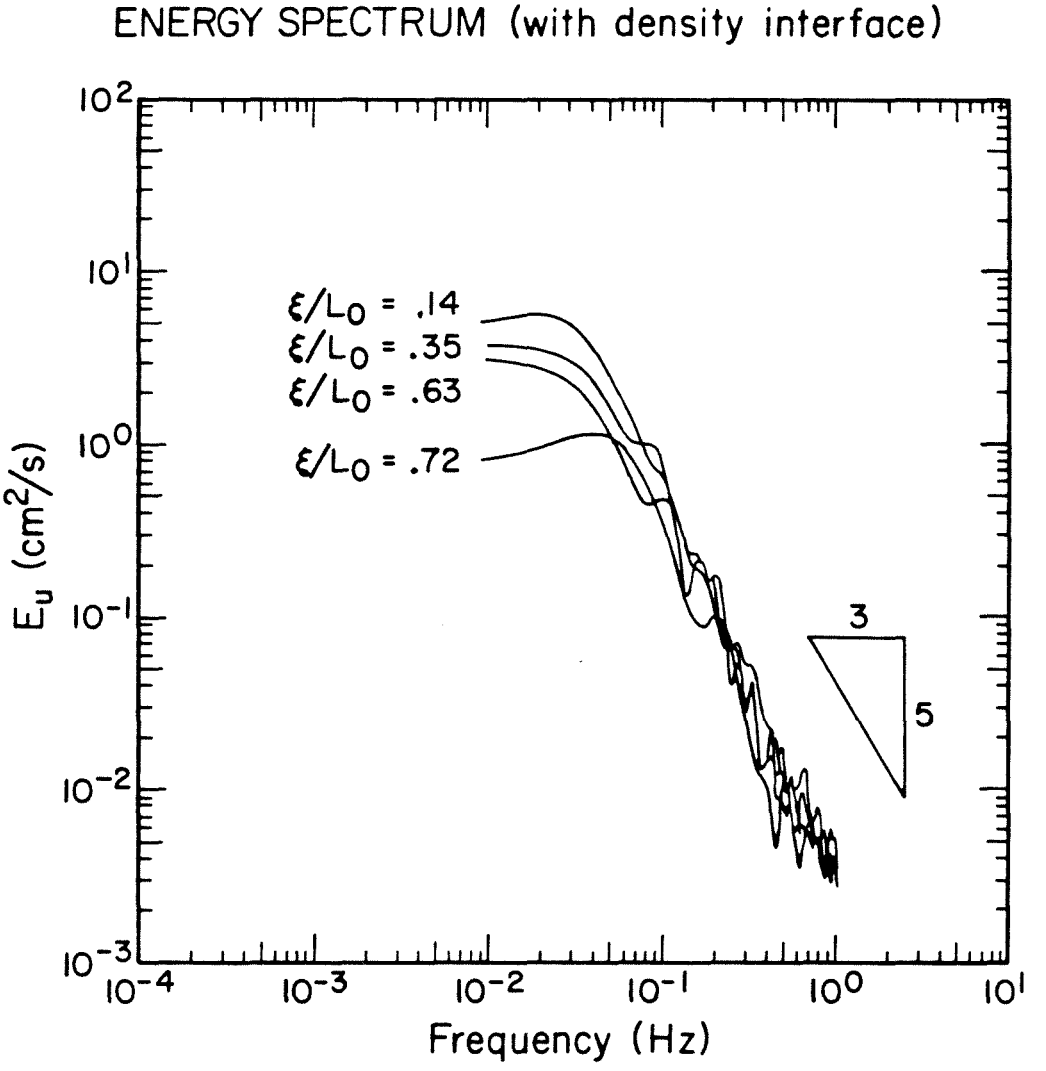

Figure 3.7b: Energy Spectra of the horizontal velocity fluctuations near the density interface. Experiment #1

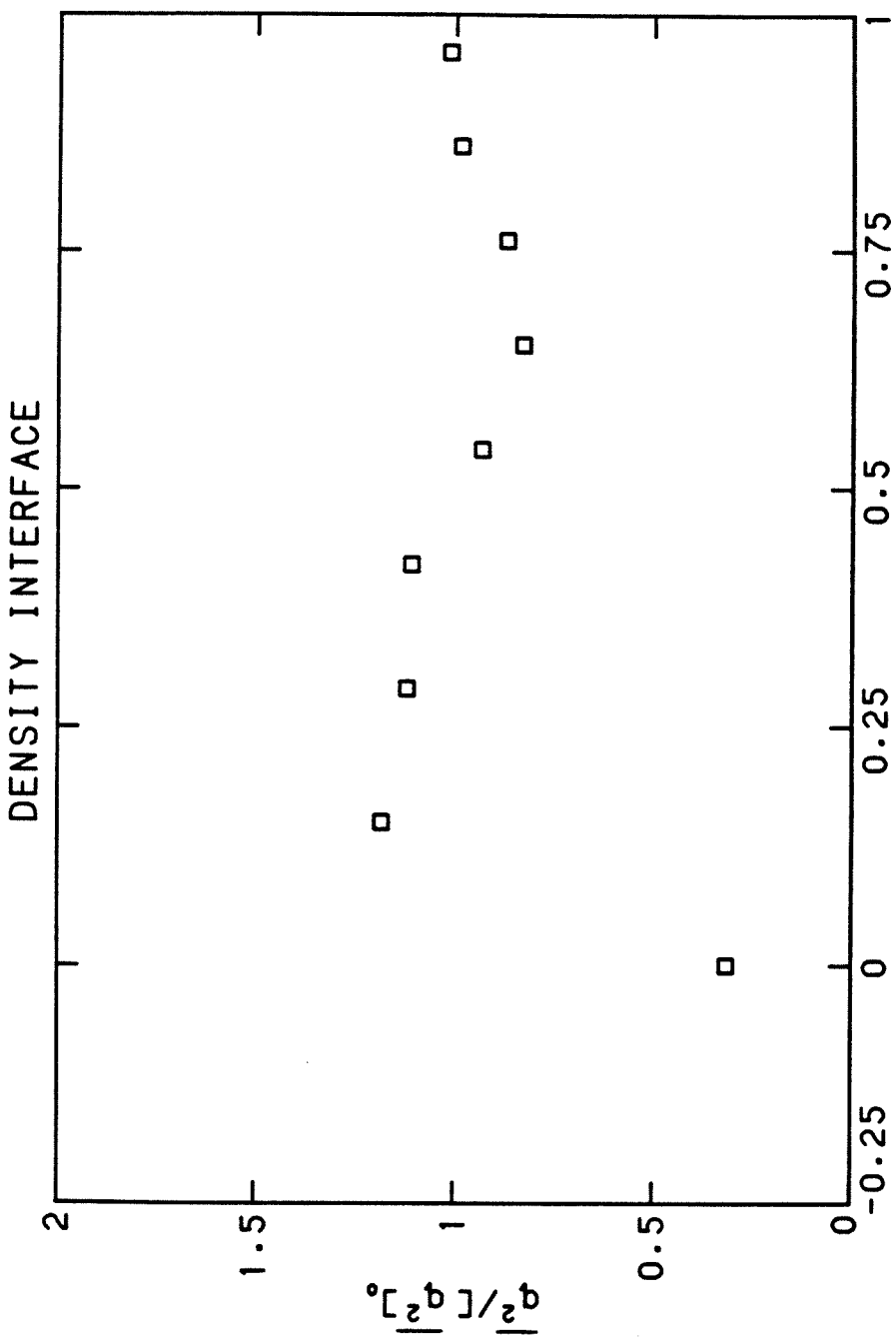

Figure 3.8: Variation of the turbulent kinetic energy per unit mass with distance away from the density interface. Experiment #1

of turbulence recovers to its value far from the boundary. Figure 3.8 also shows that $\overline{q^2}/[\overline{q^2}]_o$ exceeds 1 near the density interface. This result is reproducible in every experiment and at the first glance seems paradoxical due to the fact that the turbulent kinetic energy near the interface exceeds its value in a homogeneous fluid. However, if we plot $\overline{q^2w'}/[\overline{q^2w'}]_o$ against ξ/L_o, we notice that $\overline{q^2w'}/[\overline{q^2w'}]_o$ drops from about 1 at $\xi/L_o \sim 1$ to zero as ξ/L_o approaches zero as depicted in Figure 3.9. This implies that the energy flux divergence increases and thus the energy that was previously feeding the rest of the tank is now trapped in a layer of vertical dimension on the order of L_o. As a result, turbulent kinetic energy per unit mass values close to the interface may exceed those in a homogeneous fluid.

3.3 Measurements Near a Rigid Flat Plate

In order to compare the effect of a sharp density interface on shear-free turbulence to that of a rigid flat plate we report in this section the results of velocity measurements made near a rigid flat plate. The same set up is used as in the previous experiments except for the substitution of the two fluid system with a homogeneous fluid and the insertion of a rigid flat plate in the flow. The details of the experimental techniques were described in Section 2.6. The experimental conditions are given in Table 3.2.

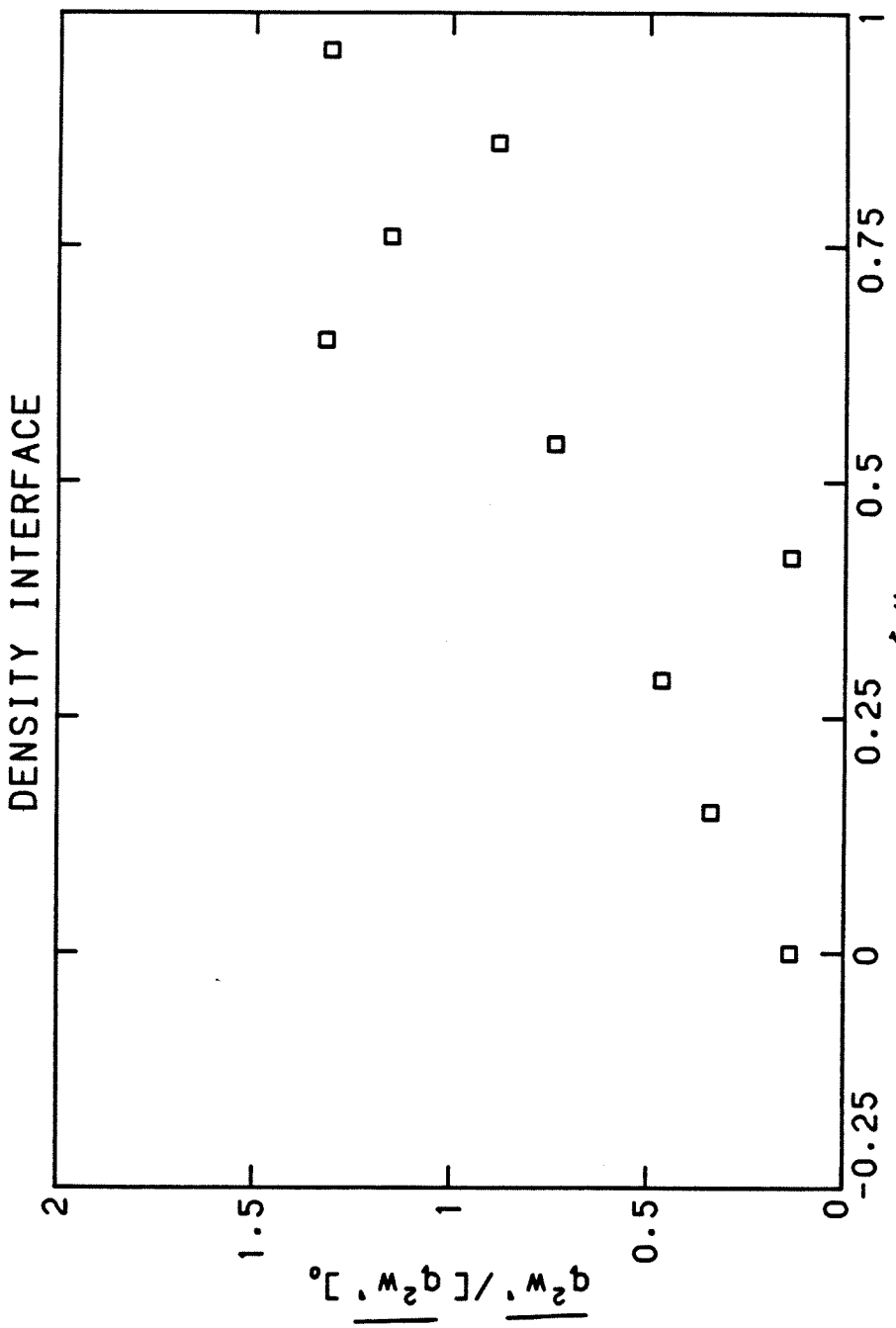

Figure 3.9: Variation of the vertical kinetic energy flux with distance away from the density interface. Experiment #1

Table 3.2

Conditions for the experiments near a rigid flat plate

Experiment number	L_o (cm)	f_g (Hz)	$[\sigma_u]_o$ (cm/sec)
3	2.12	2.20	0.44

In Figure 3.10 we plot $[\sigma_u]/[\sigma_u]_o$ and $[\sigma_w]/[\sigma_w]_o$ against η/L_o where η is a vertical distance away from the flat plate and the subscript o refers to measurements in a homogeneous fluid in the absence of a flat plate at the vertical location of the flat plate. Note that for this case, [ ] represents a spatial average of three measurements in the same horizontal plane along a straight line and separated by 2 cm. The behaviour of both $[\sigma_u]/[\sigma_u]_o$ and $[\sigma_w]/[\sigma_w]_o$ shows a striking qualitative similarity to the experiments where a density interface is present. $[\sigma_u]/[\sigma_u]_o$ is amplified at small values of η/L_o, while $[\sigma_w]/[\sigma_w]_o$ shows a continuous decay as we approach the rigid surface. Again, the effect of the wall on the turbulence seems to extend up to $\eta/L_o \sim 1$.

Figure 3.11a presents the energy spectra of the vertical velocity fluctuations E_w for different distances η/L_o away from the plate whereas Figure 3.11b shows the power spectra of the horizontal velocity fluctuations E_u. We notice that the flat plate is most effective at transferring energy from the vertical component to the horizontal components at small frequencies. The high frequency end of the spectrum is virtually unaffected by the presence of the plate. This is equivalent to saying that the larger eddies are most affected by the presence of the plate.

Figure 3.12 depicts the variation of $[\overline{q^2}]/[\overline{q^2}]_o$ with η/L_o when the flat plate is present. On the same plot the variation of $[\overline{q^2}]/[\overline{q^2}]_o$ in a homogeneous fluid in the absence of the plate is

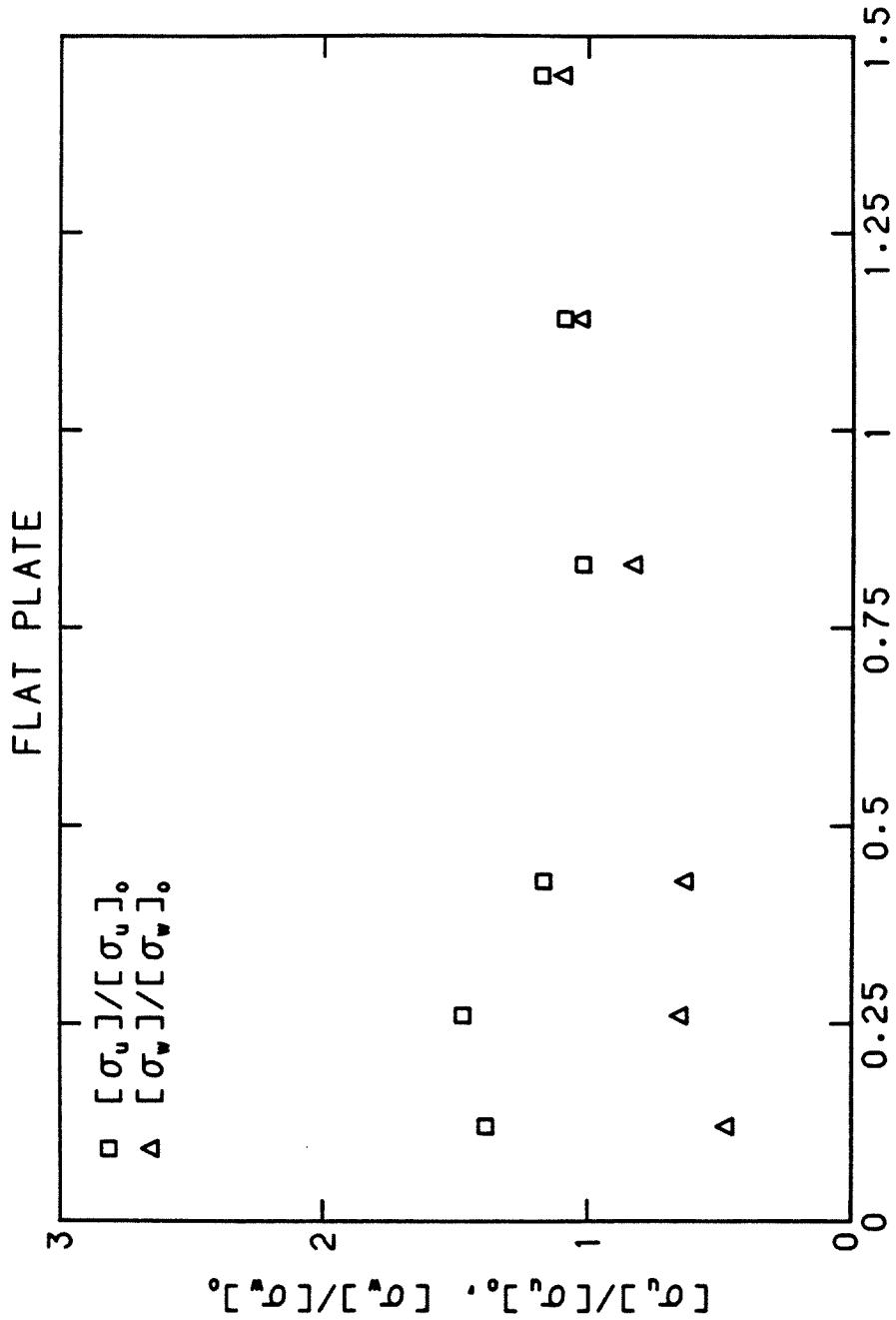

Figure 3.10: Variation of horizontal and vertical r.m.s. velocities with distance away from the flat plate

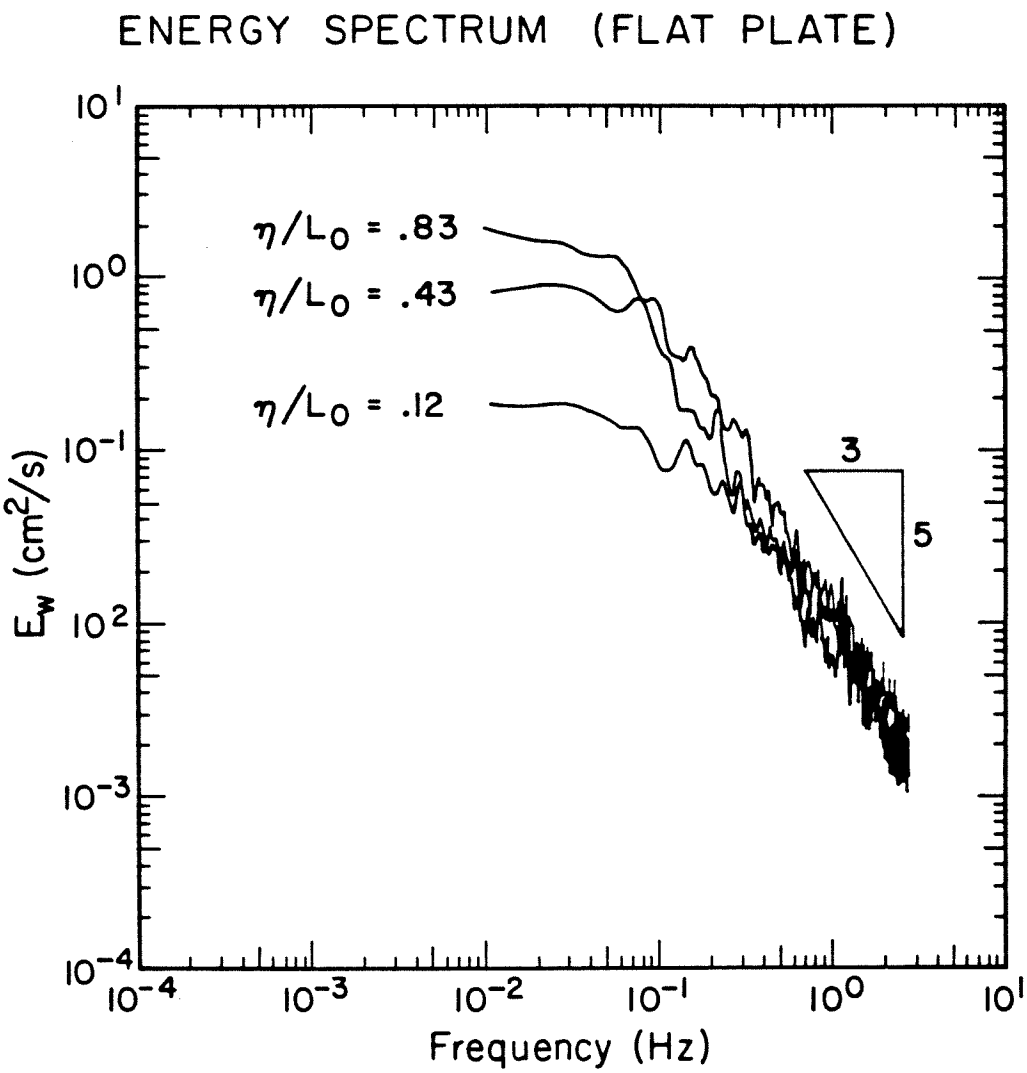

Figure 3.11a: Energy Spectra of the vertical velocity fluctuations near the rigid flat plate

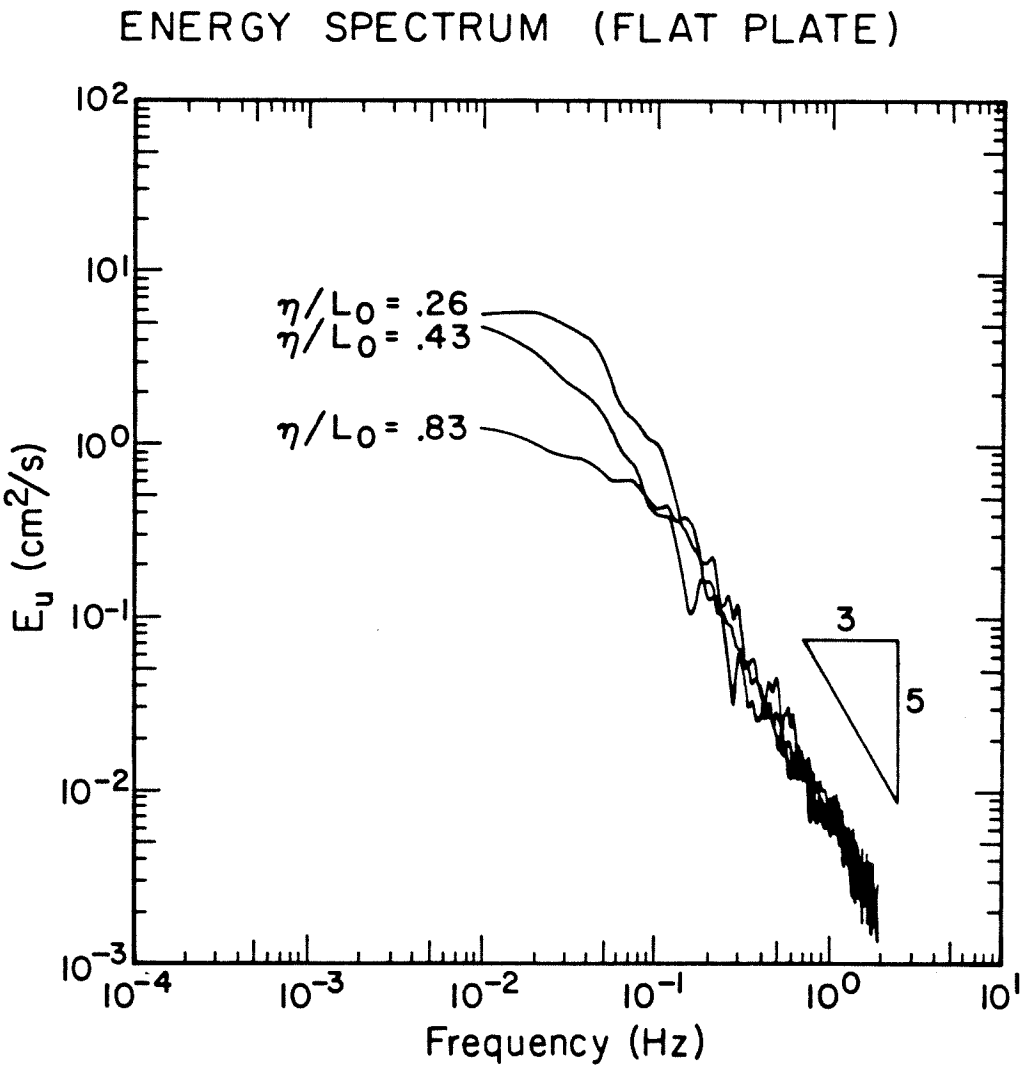

Figure 3.11b: Energy Spectra of the horizontal velocity fluctuations near the rigid flat plate

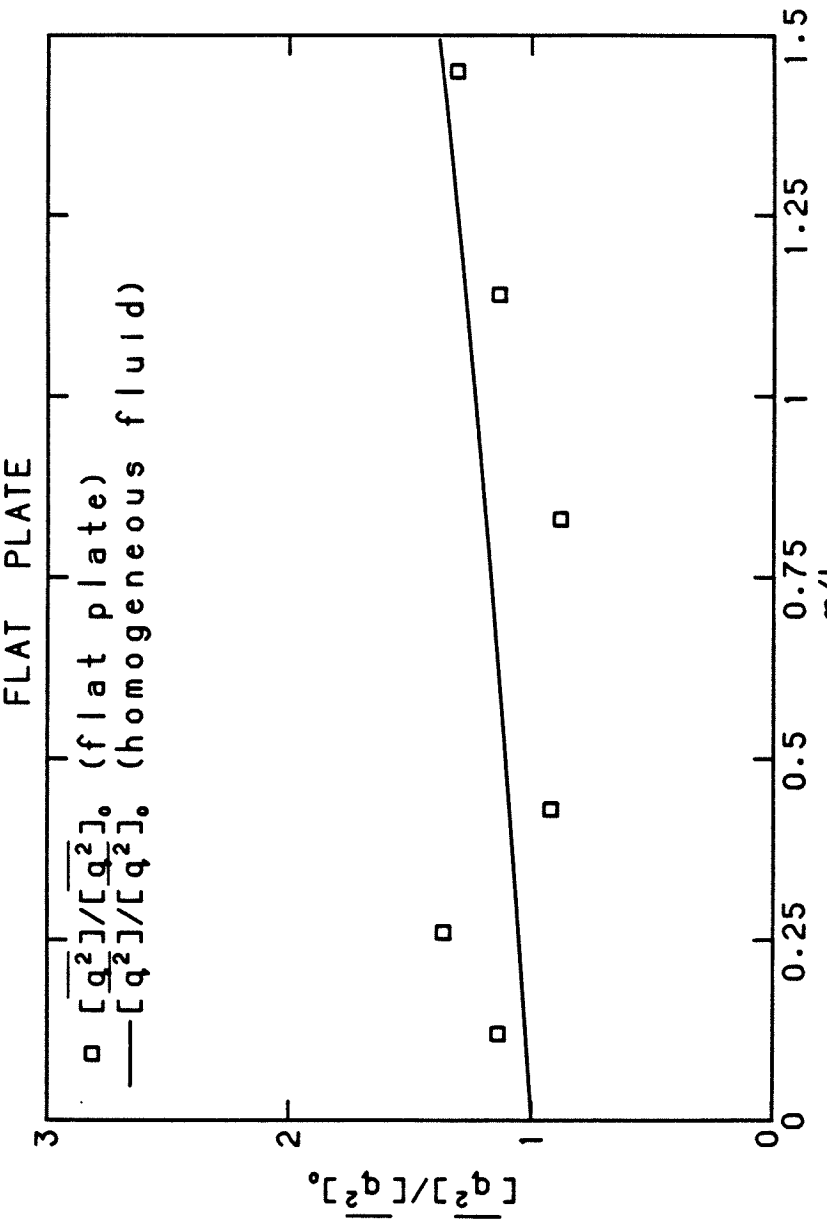

Figure 3.12: Variation of turbulent kinetic energy per unit mass with distance away from the flat plate. □ measurements near a rigid flat plate. —— measurements in a homogeneous fluid in the absence of the plate. Curve is best fit to experimental data and is of the form $[\overline{q^2}] \sim 1/z^2$

also shown *. We notice that $[\overline{q^2}]/[\overline{q^2}]_o$ in the presence of a flat plate exceeds its value in the absence of a plate at small η/L_o. This result can also be explained by the increased values of the energy flux divergence near the rigid flat plate. Figure 3.13 presents $[\overline{q^2w'}]/[\overline{q^2w'}]_o$ plotted against η/L_o. It can be seen that $[\overline{q^2w'}]/[\overline{q^2w'}]_o$ decreases from about unity to zero as η/L_o varies from one to zero. This implies that the energy flux divergence is high near the flat plate, and as a result, the turbulent kinetic energy near the flat plate can exceed its value in the absence of the plate at the same location. From Figure 3.13, we also notice that the turbulent kinetic energy per unit mass at about η/L_o = 0.5-1.4 is less than that measured in a homogeneous fluid in the absence of the plate. This might be associated with a rise in the mean pressure in that region as discussed by HG for shear-free turbulence near a rigid boundary.

3.4 Discussion

The primary objective of the present investigation was to study the nature of shear-free turbulence near a stable density interface and to acquire an increased understanding of turbulent mixing in stratified flows. The experiments indicate that the density

* It is to be noted that in Figures 3.12 and 3.13 $[\overline{q^2}]$ and $[\overline{q^2w'}]$ are normalized by their values in a homogeneous fluid at the plate and not by their values in a homogeneous fluid at the same location. Hence $[\overline{q^2}]/[\overline{q^2}]_o$ and $[\overline{q^2w'}]/[\overline{q^2w'}]_o$ in a homogeneous fluid are not equal to 1.

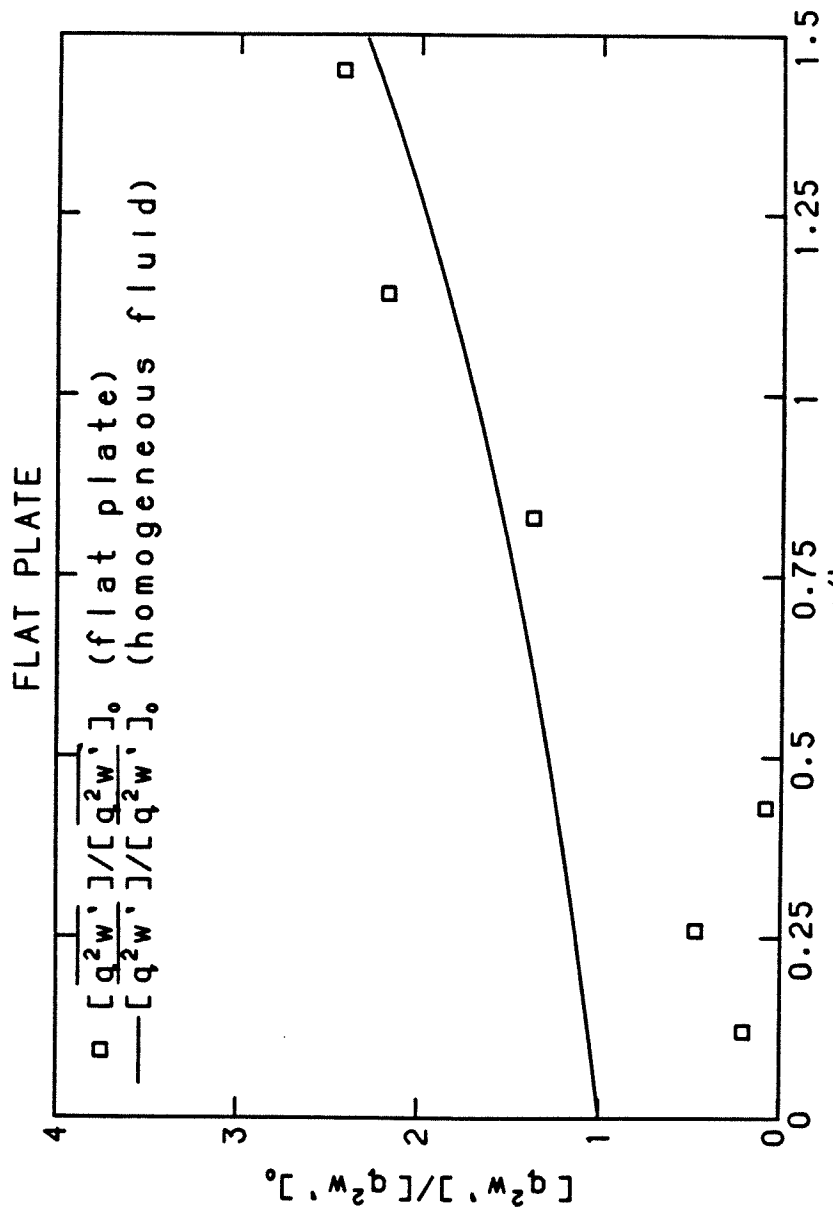

Figure 3.13: Variation of vertical energy flux with distance away from the flat plate. □ measurements near a flat plate. —— measurements in a homogeneous fluid in the absence of the plate. Curve is best fit to experimental data and is of the form $[\overline{q^2w'}] \sim 1/z_a^3$

interface acts, at least qualitatively, in a manner similar to a rigid flat plate where σ_u is amplified and σ_w is sharply attenuated in a layer adjacent to the plate. This can be regarded as being due to the flattening of the turbulent eddies near the interface/flat plate. The point at which the maximum amplification in σ_u occurs is about 0.1-0.2 L_o away from the interface or the flat plate. The effect of the interface/flat plate on the turbulence seems to extend to about one integral length scale away.

The study also determined the turbulence scales that are most affected by the anisotropy created by either a density interface or a flat plate. The power spectra of the vertical velocity fluctuations show that there is preferential attenuation of low frequencies (large scales) indicating that the density interface/flat plate is more efficient in damping large eddies. On the other hand the horizontal energy spectra indicate that there is a substantial gain at the low frequency end of the spectrum. In both the horizontal and vertical spectra, the high frequency end was not significantly affected (since the velocity at the flat plate is zero the energy spectrum will eventually approach zero in a very thin viscous layer near the wall where no measurements were made).

One reason why the density interface affects the turbulence in a very similar manner to the rigid flat plate and flattens the turbulent eddies may be the sharpness of the density interface. Figure 3.14 (a-c) presents pictures of the density interface taken

by illuminating the flow with a sheet of laser light about 0.5 mm thick and with fluorescent dye added to the upper mixed layer. The advantage of this method of planar illumination is in the preservation of the flow detail that is masked when the visualization method averages over the thickness of the tank. Figures 3.14a and 3.14b indicate that the interface between the turbulent and the non-turbulent fluid can be very sharp. This is in contrast to the findings of Crapper & Linden (1974) who visualized the flow through a shadowgraph and also determined the interfacial thickness by using a conductivity probe. It is thought that the determination of the interfacial layer thickness using a shadow graph can be misleading since the resulting image represents an average over a large horizontal span. Detailed interfacial layer thickness measurements using laser-induced fluorescence techniques that are reported in Chapter 4 support the fact that the interfacial layer thickness h is finite but can be much smaller than $h/\ell_o \sim 1\text{-}1.5$ as determined by Crapper & Linden (1974).

Turner (1968) concluded that the large eddies are entraining fluid in the form of sheets, which are ultimately mixed through the whole stirred layer. Although our Figures 3.14a and 13.14b are similar to Turner's Figure 2a in that they show eddies impinging on the interface, movie films obtained in our experiment (using the same method of visualization) indicate that the large eddies that impinge on the interface "bounce" back up with no significant

Figure 3.14a: Picture of the flow obtained using thin laser sheet illumination. The fluorescent dye is pre-mixed with the upper layer fluid which appears light. $R_j \sim 60$. 1 cm in the picture corresponds to 1.2 cm in actuality

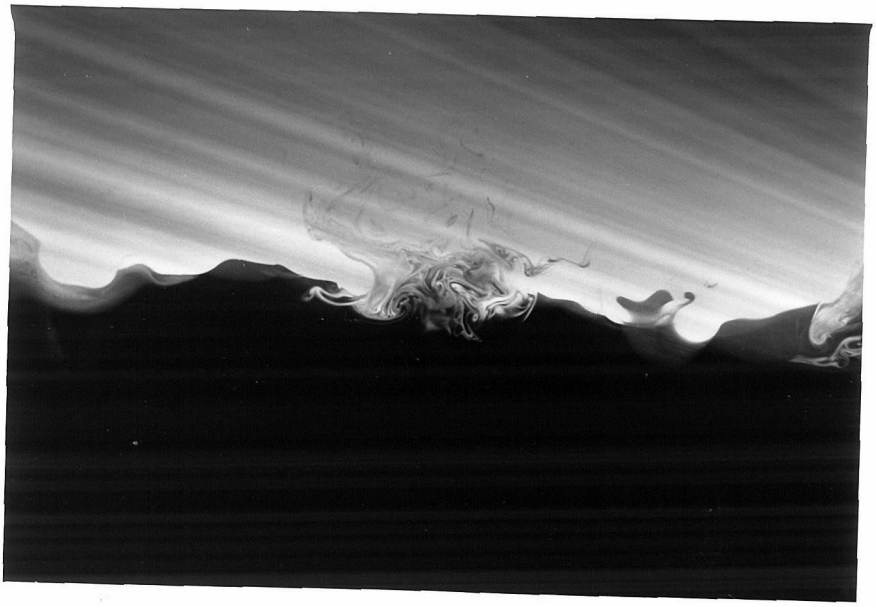

Figure 3.14b: See Figure 3.14a for caption

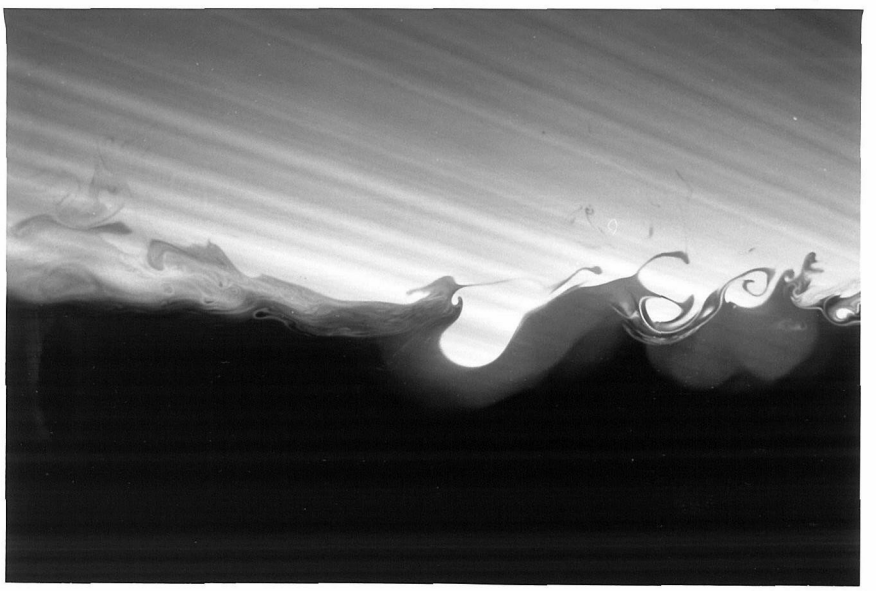

Figure 3.14c: See Figure 3.14a for caption. The cloudiness is due to reflected light from the rear window of the tank

entrainment of unstirred fluid. The movies also indicate that patches of turbulence such as those in Figures 3.14a and 3.14b might be the result of local interfacial instabilities that give rise to patches of intense, small scale turbulence. Such patches occur sporadically in time and space. Figure 3.14c also shows some intermittent mixing processes at a density interface. In this figure the mixing processes at the right of the picture seem to be more regular than those depicted in Figures 3.14a and 3.14b. They appear to have some of the characteristics of Kelvin-Helmholtz billows. It is worth noting that the occurrence of mixing events such as the ones in Figure 3.14c is apparently much less frequent than mixing events similar to those in Figures 3.14a and 3.14b.

The findings of our investigation for both the density interface and the rigid flat plate indicate strong qualitative (and sometimes quantitative) agreement with the postulates of the theory of HG. In particular, the amplification of the horizontal velocities accompanied by a sharp reduction in the vertical velocity, the form of the energy spectra, and the distance up to which the effect of the wall/density interface is felt are all in accordance with the predictions of HG's theory. At this point, it is worth noting that the theory of HG is valid when the inertial effects of the turbulence are not important and the vertical energy flux is zero. However, Hunt (1984) shows that the basic conclusions of HG are still valid even for $t > \tau_o$ provided the rate of

dissipation of turbulent kinetic energy is constant over $\eta \sim L_o$. This might explain why our experiments which describe the steady-state flow near the plate show some agreement with the results of HG. One observation which is not in good agreement with the results of HG is the magnitude of the amplification of the horizontal turbulent velocity. Near both the density interface and the flat plate, σ_u is amplified by as much as 40% as opposed to a maximum of 22% predicted by HG. This discrepancy might be due to the increased values of the energy flux divergence near the density interface and the flat plate. Moreover, the decrease in the energy of the turbulence (compared to homogeneous fluid values) in a region near the interface and the flat plate is in qualitative agreement with HG. They argued that the decrease in the energy of the turbulence is associated with a rise in the mean pressure in the same region.

The thickness of the viscous sub-layer δ^ν, where the horizontal velocity begins to be attenuated, is predicted by HG to be $2\ (\nu\tau_\infty)^{1/2}$, where τ_∞ is the integral time scale of the turbulence in the free stream. This prediction holds for times on the order of τ_∞ after the turbulence encounters the wall. In our experiments, $2(\nu\tau_o)^{1/2}$ is approximately 0.35 cm. The closest point to the plate that we were able to measure velocities was at 0.25 cm away from the plate surface. At that point $[\sigma_u]$ has not shown any significant decay. Although we did not measure δ^ν we can still suggest that δ^ν

in our experiments is not larger than predicted by a $\delta^{\nu} = 2(\nu\tau_o)^{1/2}$ relationship.

Our results are also in agreement with some of the results in the model proposed by Long (1978). In that model, Long conjectures that the results of the theory of HG apply to the case where the rigid plate is replaced by a high R_j density interface. Long also finds that the large turbulent eddies are flattened near the density interface and he characterizes the entrainment process as an intermittent bursting phenomena. Our results and flow visualization pictures seem to support these arguments. Long also showed that $w_h \sim \sigma_u R_j^{-1/4} \ll \sigma_u$. However, we cannot test the validity of such a relationship from our velocity measurements due to the large errors that might be involved in measuring very small velocities with our LDV equipment. Nevertheless, we are able to estimate w_h from the concentration measurements and this will be discussed in Chapter 4.

As a result of the redistribution of kinetic energy near the density interface, the kinetic energy in the vertical velocity component is only a small fraction of the total kinetic energy. Therefore, previous conjectures (Linden 1975) that the rate of change of potential energy due to mixing is proportional to the total kinetic energy flux available at the interface may not be valid.

McDougall (1979b) carried out experiments to measure the velocities in and near a density interface and in the vicinity of a rigid flat plate. His results did not indicate any substantial amplification of the horizontal velocity in the vicinity of the flat plate. According to McDougall there is a "... hint of some amplification of the horizontal velocity" at higher R_i but he did "not have enough accurate data to assert this with confidence". This observation might be possibly due to the low Reynolds numbers used in McDougall's experiments (the Reynolds numbers for McDougall's experiments were about 40), as opposed to values of around 120 in our experiments. The HG theory is valid only at high Reynolds numbers and the experiments of Uzkan & Reynolds (1967) and Thomas & Hancock (1977) clearly show that high Reynolds number turbulence is necessary for the amplification of the horizontal velocity component.

It is also worth mentioning here that measurements at about one integral length scale below the mean interface indicate that the velocity is very small and is indistinguishable from the noise in the LDV signal. This suggests that the interface inhibits the downward transport of the mixed layer turbulence. It is thought that the motion below the interface is irrotational, and as a result, decays exponentially.

CHAPTER 4

CHARACTERIZATION OF THE CONCENTRATION FIELD AND THE INTERFACIAL STRUCTURE

In this chapter, we report the details of linear concentration measurements and concentration-velocity correlations in and near the density interface. We start by making qualitative observations about the structure of the density interface. Following that, we discuss, in a more quantitative way, the characteristics of the interface and the internal wave field. Finally, we present a simple model for turbulent entrainment at a shear-free density interface and compare our model with previous experimental findings.

4.1 Preliminary Observations

The most convenient and illustrative method of presenting the linear concentration data is by displaying them in false color images using a color video screen and an image processor. Figures 4.1(a,b,c,d) present such images of the flow reconstructed from the Reticon camera data. In these figures, the vertical axis represents a vertical distance whereas the horizontal axis represents time. The concentration data, which have values from 0 to 255 (with 0 corresponding to fluid with no Rhodamine 6G dye), are color coded according to the spectrum accompanying Figure 4.1. R_j for the experiments presented in Figure 4.1 and in the rest of this chapter

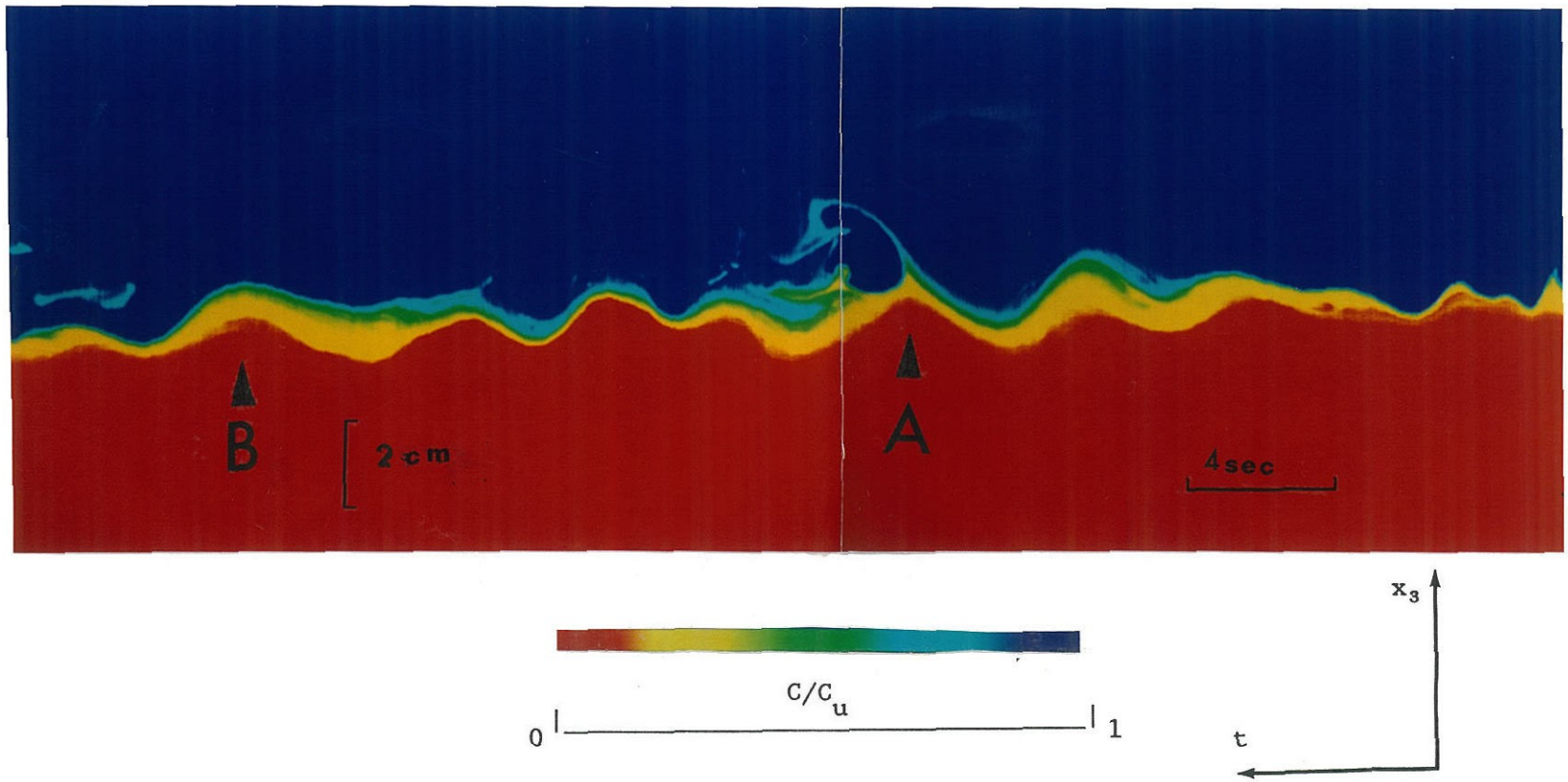

Figure 4.1a: Flow images reconstructed from the Reticon camera data. (a) & (b) R_i = 24; (c) R_i = 39; (d) R_i = 98. The color assignments are also shown. The events marked A through H correspond in time to those in figure 6. Vertical location where the velocity was measured is marked by an x.

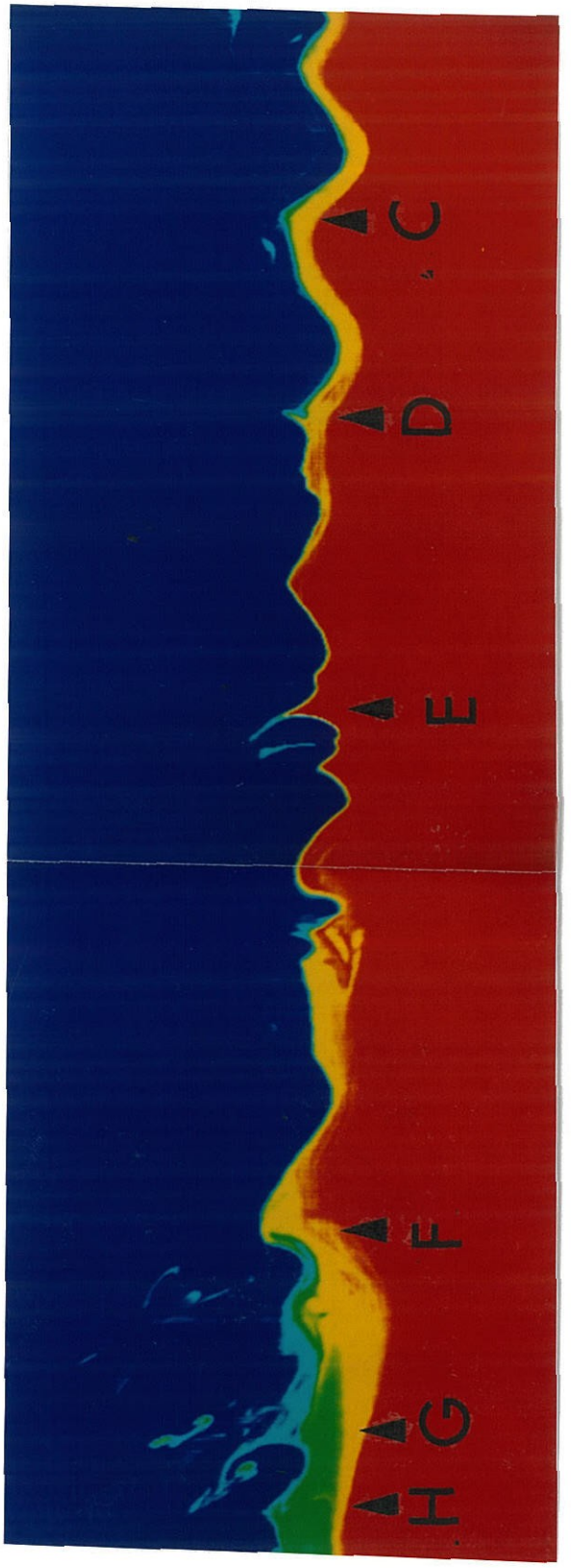

Figure 4.1b: See Figure 4.1a for caption

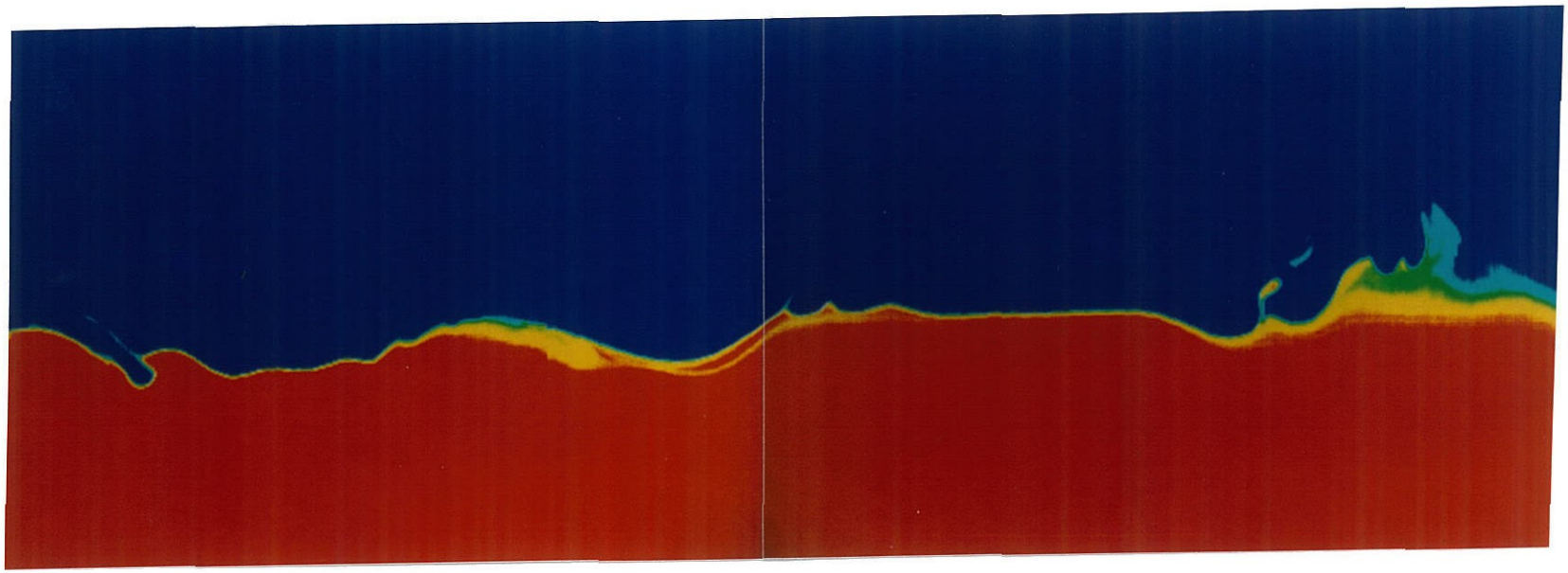

Figure 4.1c: See Figure 4.1a for caption

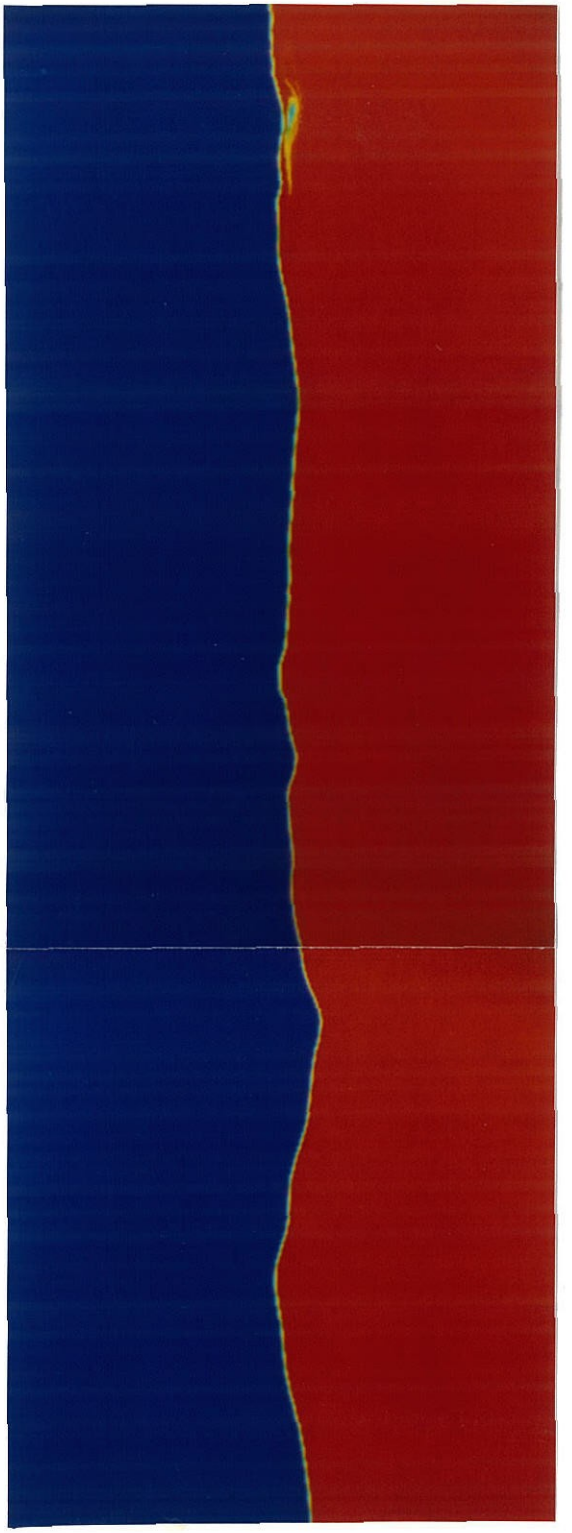

Figure 4.1d: See Figure 4.1a for caption

is in the range 24-98. R_j was calculated based on average values during an experiment.

In Figures 4.1a and 4.1b, which present sequential flow images at $R_j = 24$, it can be seen that the amplitude of the interfacial waves is of the same order of magnitude as the thickness of the interfacial layer. We can also observe that the shape of the concentration profile varies with time and cannot be adequately described by any one specific profile. In particular, an instantaneous concentration profile does not bear much resemblance to the average concentration profile, a result which is in disagreement with Crapper & Linden (1974). The interfacial waves seem to break intermittently thus giving rise to localized patches of turbulent fluid. This breaking of the internal waves seems to occur predominantly at the crests of the waves (*i.e.*, when the interface is near its highest point of oscillation). After the occurrence of these local instabilities, some mixed fluid is transported upwards and ultimately becomes fully incorporated into the upper mixed layer. As R_j increases, as shown in Figures 4.1c and 4.1d, the amplitude of the interfacial waves as well as the thickness of the interfacial layer tend to decrease. Additionally, the interface seems to get 'calmer' and the frequency of violent overturns decreases with increasing R_j. At $R_j = 98$ as shown in Figure 4.1d, the mixing events seem less frequent and not as violent as at lower R_j. However, this should be regarded with caution,

since in this case the thickness of the interfacial layer is comparable with the spatial resolution of our equipment. As a result, some mixing events might go undetected. Quantitative results concerning the thickness of the interface and the properties of the internal waves will be presented in Section 4.2.

In Figure 4.2, a 30 s time-averaged concentration profile at $R_j = 24$ is shown. An instantaneous concentration profile obtained in less than 10 ms is also presented. We can observe, in a more quantitative way than in Figure 4.1, that the instantaneous concentration profile does not bear much resembance to the average profile. This is thought to be due to both (i) the contribution of internal waves to the average thickness of the interfacial layer and to (ii) the temporal change in the shape of the instantaneous profile. The significance of the internal wave motions in determining the time-averaged concentration profile depends on the ratio of the amplitude of the internal waves to the instantaneous thickness of the density interface. The larger this ratio, the more important the interfacial wave contribution will be. It will be seen from results in Section 4.2 that this ratio increases with increasing R_j. The temporal change in the shape of the instantaneous profile is determined by the dynamics of the interface and the occurrence of instabilities and mixing events. It can be observed from Figure 4.1 that the temporal variability in the shape of the instantaneous concentration profile decreases with increasing

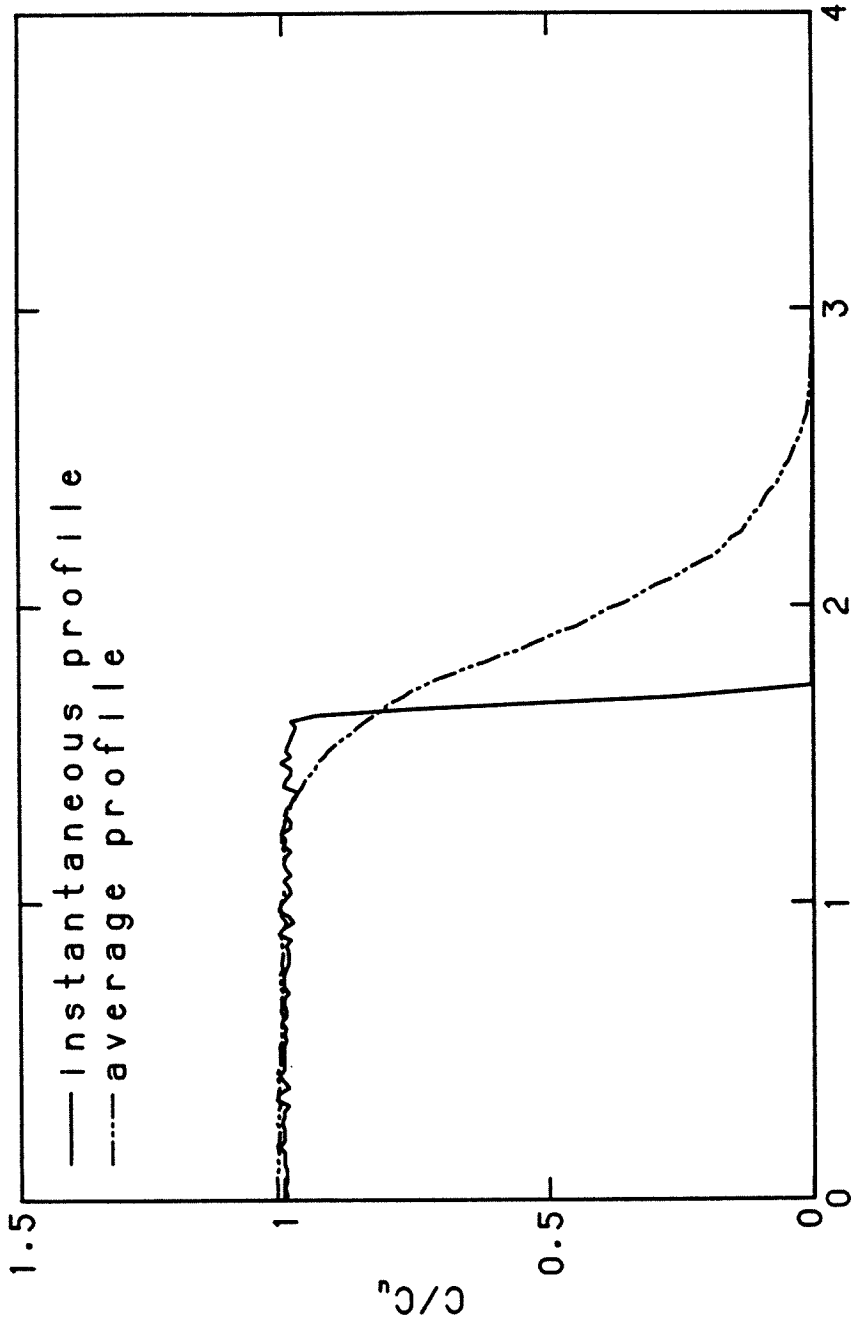

Figure 4.2: —··—30 sec time-averaged concentration profile
——— 'instantaneous' concentration profile
obtained in less than 10 ms. $R_j = 24$

R_j.

It is of interest to further investigate the intermittent mixing events within the density interface. Figure 4.3 presents a time history of the vertical velocity component at a point near the interface for the same experiment depicted in Figures 4.1a and 4.1b. The vertical position of the point at which the velocity was measured is marked on Figure 4.1a. Moreover, the dye concentration C at that same point, normalized by the time-averaged concentration in the upper mixed layer C_u, is also shown. Another quantity that is presented in Figure 4.3 is $\psi = [1-C/C_u]w$ which represents the vertical flux of the clear (lower) fluid. In this particular case, ψ is more useful as an indicator of interfacial activity than $(C/C_u)w$, the vertical dye flux. This is a result of ψ preferentially disclosing motion of lower fluid mixing into the upper layer fluid as shown in Figure 4.3. The temporal relationship between Figure 4.3 and Figures 4.1(a,b) is established by the use of alphabetically labelled arrows that correspond to the same instants in time.

Event A depicted in Figure 4.1a indicates that some lower layer fluid is being ejected upwards. An examination of Figure 4.3 indicates that at A the vertical velocity maintains significant upward (positive) values. Figure 4.3 also shows that ψ remains positive for about 5 seconds. These observations imply that Event A represents a situation where there is a net vertical mass flux and

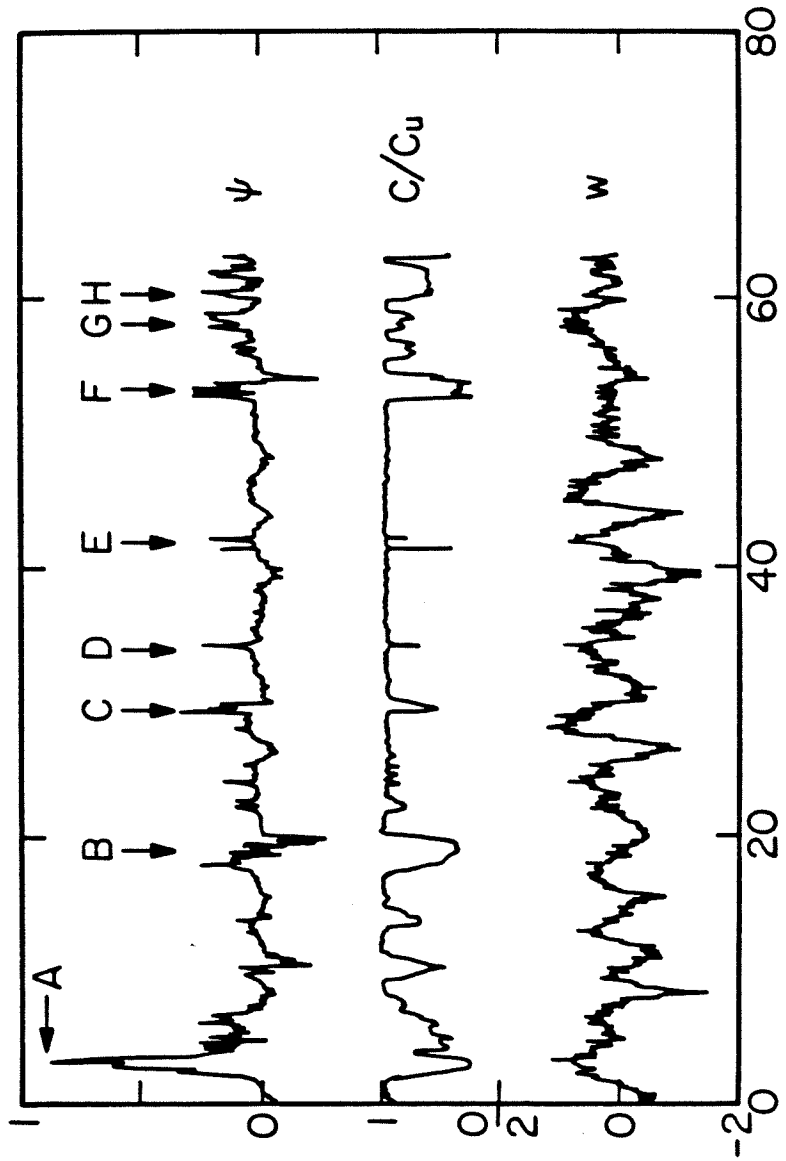

Figure 4.3: Time history of the vertical velocity, concentration, and vertical flux of clear fluid. (a) vertical velocity w (cm/sec) versus time. (b) C/C_u versus time. (c) ψ (cm/sec) versus time. The events marked A through H correspond to those in figure 4(a,b). $R_j = 24$

can hence be labeled a mixing event. On the other hand, ψ in Event B switches signs in going from positive to negative. The net vertical mass flux associated with B is small. This implies that the observed behaviour at B is due to an interfacial wave since the net vertical mass flux associated with internal waves is zero. An examination of Figure 4.1a also supports this observation.

Other occurrences of events leading to a net vertical mass transport can be determined from an examination of ψ in Figure 4.3. There are several discrete positive peaks in ψ without accompanying comparable negative values. The arrows labeled C, D, E, G, and H all indicate such events. Another observation that can be made from Figure 4.3 is that the vertical velocity maintains significant upward values for these events. The length of time during which w is upward is usually longer than the time ψ remains positive for the individual events. The flow images at E and G in Figure 4.1b clearly reveal that some fluid is being ejected upwards whereas the processes involved at C, D and H are less obvious. However, we can notice that at C ,D, and H the interfacial structure is abrupt and pointed and does not exhibit the smoothness associated with relatively uninterrupted internal waves (such as B). The event marked F indicates that ψ switches sign from positive to negative. The net flux of clear fluid associated with F is upward since the net area under the ψ curve in the vicinity of F is positive. All these observations, when viewed in their entirety, indicate that the

intermittent mixing events occur sporadically in time.

4.2 Characteristics of the Interface and the Internal Wave Field

In this section we will present some quantitative results concerning the dynamics of the density interface and the internal wave field. Figure 4.4 presents concentration contours of C/C_u. Three contours are shown corresponding to $C/C_u = \alpha$ with α taking on the values 0.1, 0.5, and 0.9. To obtain a certain $C/C_u = \alpha$ contour the following procedure was followed: (i) for each array scan determine, starting from the bottom of the scan, the vertical position of the first point at which C/C_u exceeds α; (ii) repeat (i) for every scan; (iii) plot the vertical position versus time. One consequence of the use of this method for determining contours is its inability to determine multiple occurrences of $C/C_u = \alpha$ in the event of concentration inversions. However, the fraction of time at which there is an inversion in the concentration profile is small in all our experiments.

Contours similar to the ones presented in Figure 4.4 are very useful in studying the dynamics of the density interface. The slope of a least-squares straight line fitted to a particular contour is a measure of the vertical velocity u_e of the interface. Such least-squares lines were obtained and a representative one is shown in Figure 4.5. The results indicate that $u_e/[\sigma_u]_o \sim R_j^{-n}$, with n being close to 3/2 as shown in Figure 4.6. This result is in

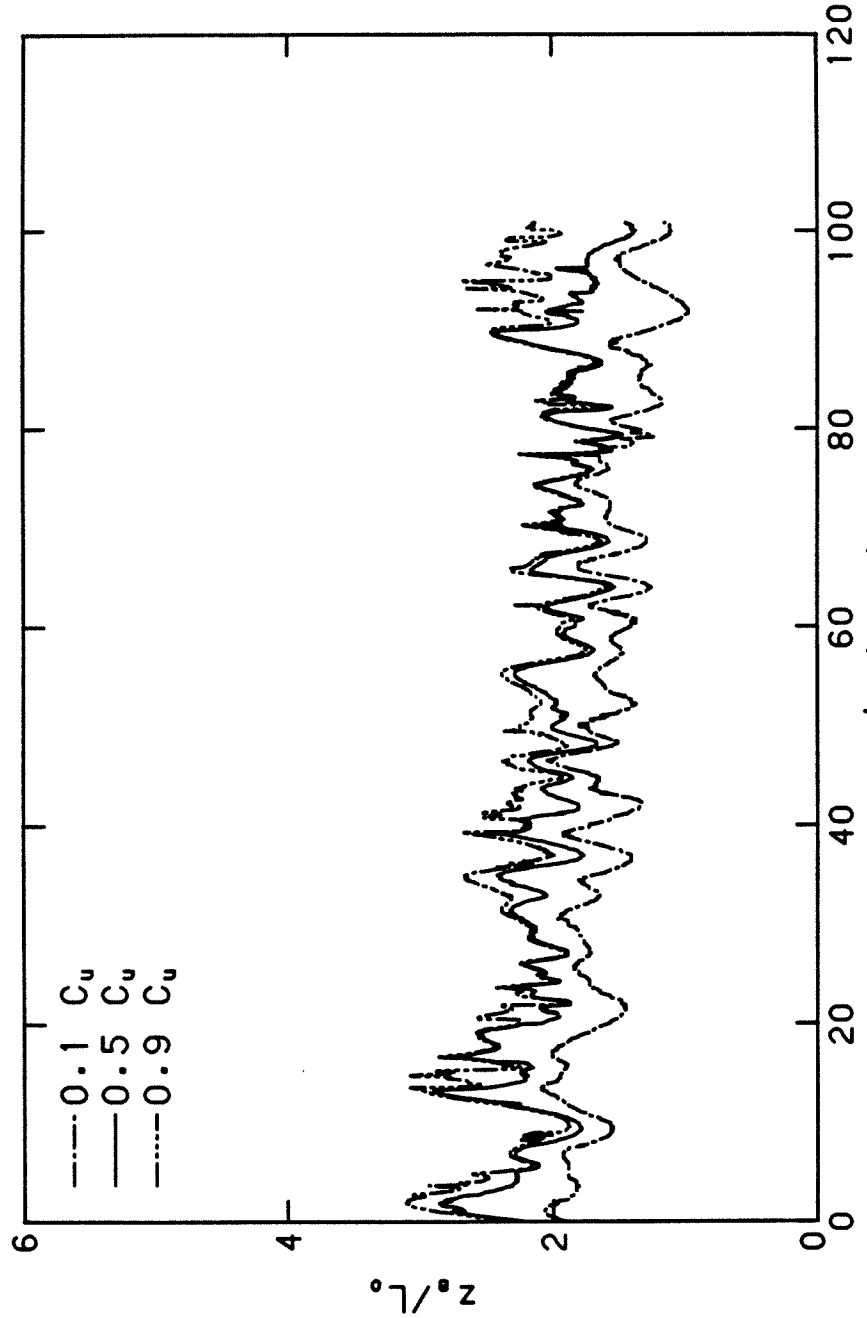

Figure 4.4: Concentration-time contours corresponding to C/C_u = 0.1, 0.5, and 0.9. R_j = 24

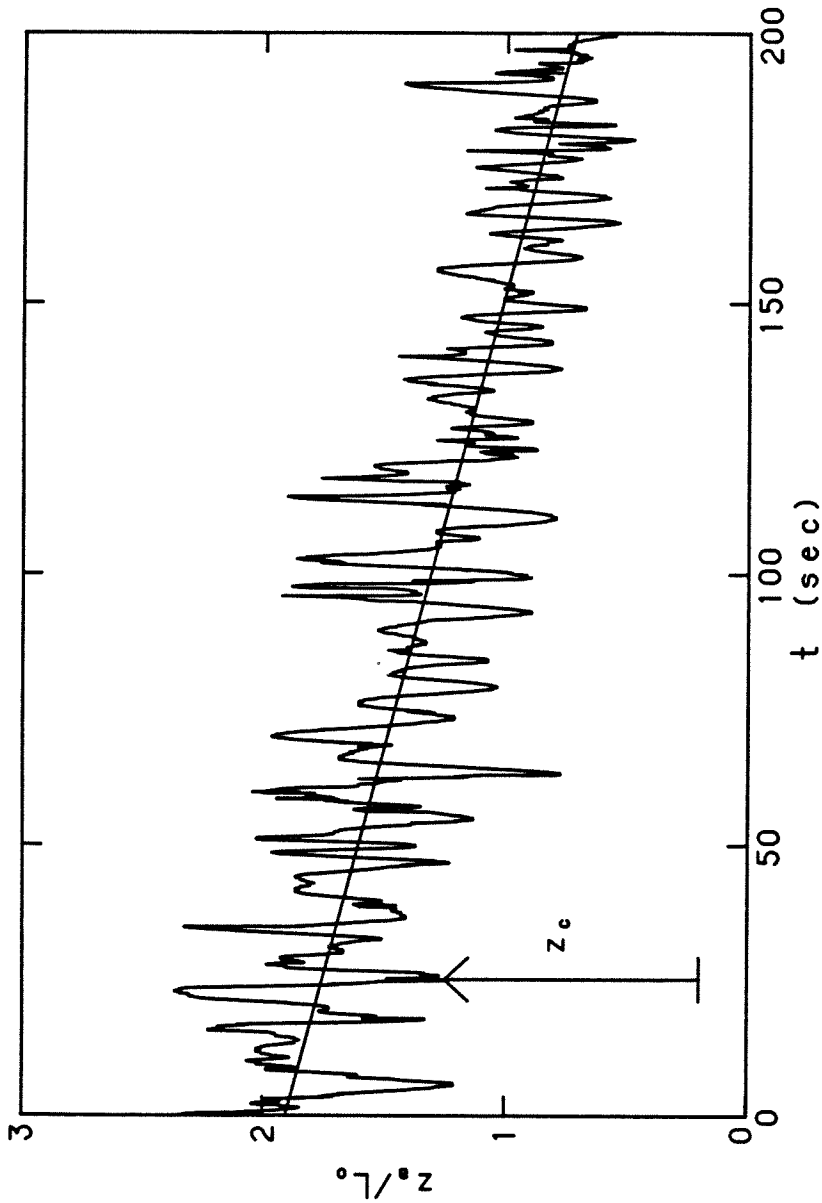

Figure 4.5: Concentration-time contour for $C/C_u = 0.5$ at $R_j = 24$. The straight line is a least-squares best fit line for the contour

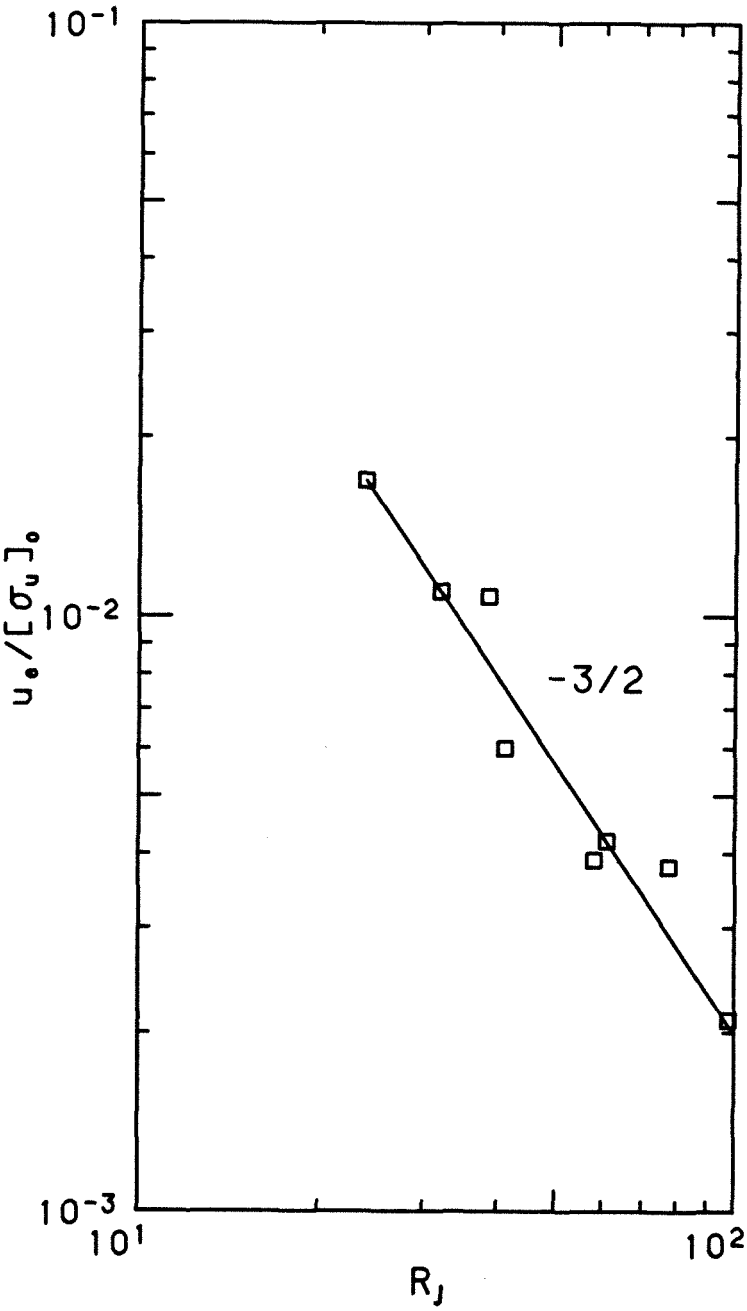

Figure 4.6: Variation of $u_e/[\sigma_u]_o$ with the overall Richardson number R_j

agreement with Hopfinger & Toly (1976) and Turner (1968). The variables in the experiments discussed in this chapter are given in Table 4.1. The magnitude of the deviations of a certain contour from the least-squares straight line, denoted by χ, yields a measure of the amplitude of the interfacial waves. To determine a representative quantity that characterizes the amplitude of the internal waves, we located the C/C_u = 0.1, 0.5 and 0.9 concentration contours for each experiment and then determined the least-squares best fit line for each of these contours. The r.m.s. value of χ was then computed and its average for the three different contours in each experiment, denoted by ζ, was determined. ζ is an overall measure of the amplitude of the internal waves. The averaging procedure was used to compensate for the limited length of record available in each experiment.

Figure 4.7 presents a plot of ζ/L_o versus R_j. It can be seen that a relationship of the form $\zeta/L_o \sim R_j^{-1}$ provides a good fit for the experimental data. Actually, a least-squares line fit to the data yields $\zeta/L_o \sim R_j^{-.91}$. A $\zeta/L_o \sim R_j^{-1}$ relationship implies that $\zeta \sim [\sigma_u]_o^2/\Delta b$, *i.e.*, the amplitude of the interfacial waves is determined by the relative magnitude of the kinetic energy of the eddies and the buoyancy jump across the density interface.

If z_c is a vertical distance to a certain contour line measured from an arbitrary origin as shown in Figure 4.5, then $w_d = d(z_c)/dt$ represents an instantaneous vertical velocity of the internal waves.

Table 4.1

Conditions for the experiments involving concentration measurements

Experiment number	L_o (cm)	f_g (Hz)	$[\sigma_u]_o$* (cm/sec)	$\Delta\rho$ (gm/cm^3)	R_j
4	1.60	2.20	0.60	0.00541	24
5	1.70	2.20	0.60	0.00693	32
6	1.90	2.12	0.48	0.00478	38
7	1.84	2.32	0.54	0.00664	41
8	2.17	2.20	0.46	0.00579	58
9	1.95	2.25	0.49	0.00767	61
10	2.15	2.25	0.45	0.00737	77
11	2.39	2.25	0.40	0.00671	98

* $[\sigma_u]_o$ was calculated based on values at $f_g = 2.20$ using $[\sigma_u]_o \sim f_g$.

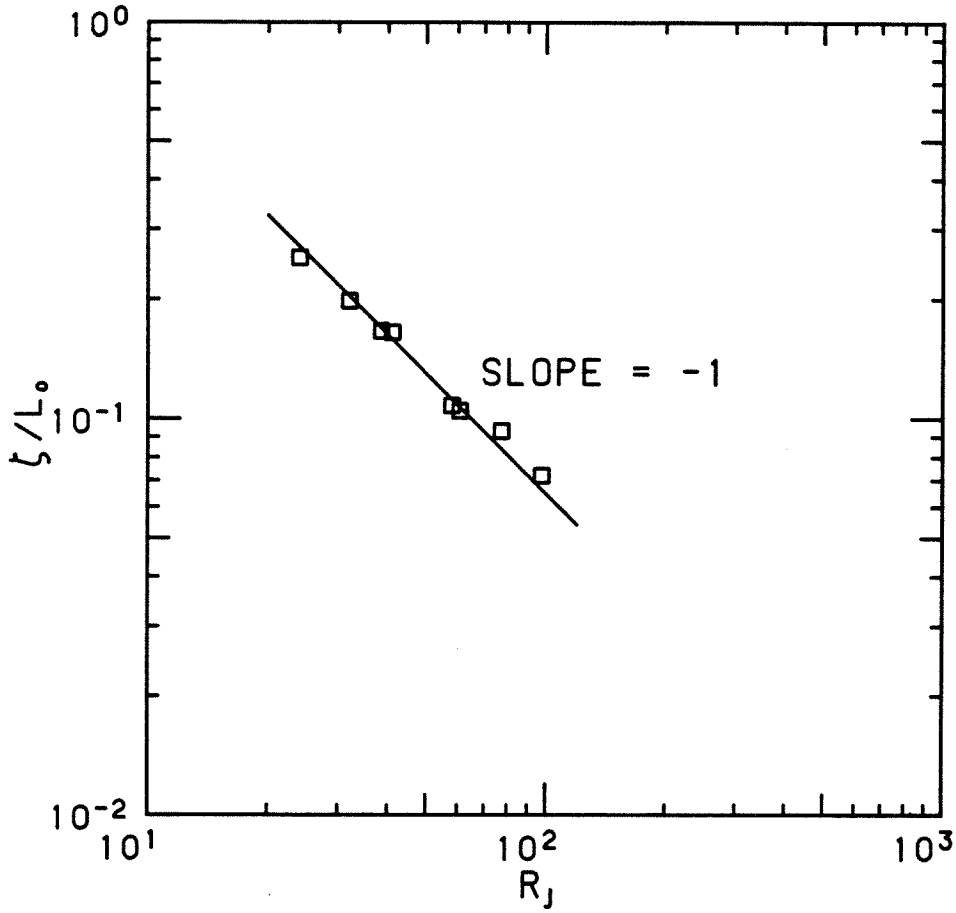

Figure 4.7: Variation of the normalized internal wave amplitude ζ/L_o with the overall Richardson number R_j

Figure 4.8 presents w_d as a function of time obtained from the $C/C_u = 0.5$ concentration contour at $R_j = 24$. Every tenth point in the original concentration contour was used and the deriviative was calculated by taking the difference between two adjacent points. No smoothing or filtering was applied. The r.m.s. value of w_d was determined and the average of the r.m.s. values from the $C/C_u = 0.1$, 0.5 and 0.9 contours, referred to as w_i, was then computed. Here again, the averaging procedure was used to compensate for the limited time record in the experiments. The quantity w_i is a measure of the vertical velocity of the internal waves. Figure 4.9 presents $w_i/[\sigma_u]_o$ as a function of R_j. It can be observed that w_i is well represented by a relationship of the form $w_i/[\sigma_u]_o \sim R_j^{-1/2}$. After the determination of interfacial wave amplitudes and velocities we obtained a measure of the internal wave frequency n_a defined as $n_a = c_1(w_i/\zeta)$ where c_1 is a constant. By invoking the $w_i/[\sigma_u]_o \sim R_j^{-1/2}$ and $\zeta/L_o \sim R_j^{-1}$ relationships we obtain $n_a \sim (\Delta b/L_o)^{1/2}$. It is to be noted here that if most of the energy resides in the lowest internal mode as usually is the case when the thermocline is relatively sharp (Phillips 1977), then n_a is approximately equal to the frequency of the lowest internal wave mode.

The vertical concentration gradient in each scan was determined by evaluating the spatial derivative of the concentration profile. The derivative was computed by taking the difference in

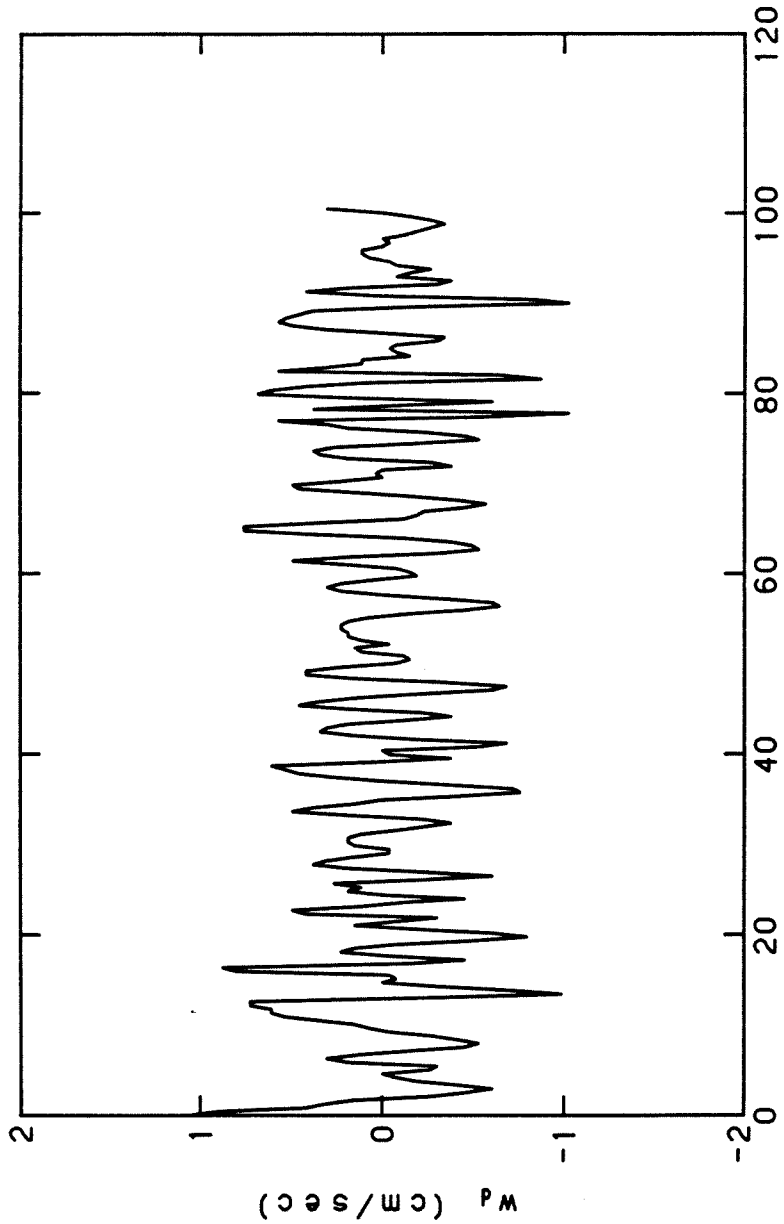

Figure 4.8: Variation of the instantaneous vertical wave velocity w_d with time. The record is obtained from the $C/C_u = 0.5$ contour at $R_j = 24$

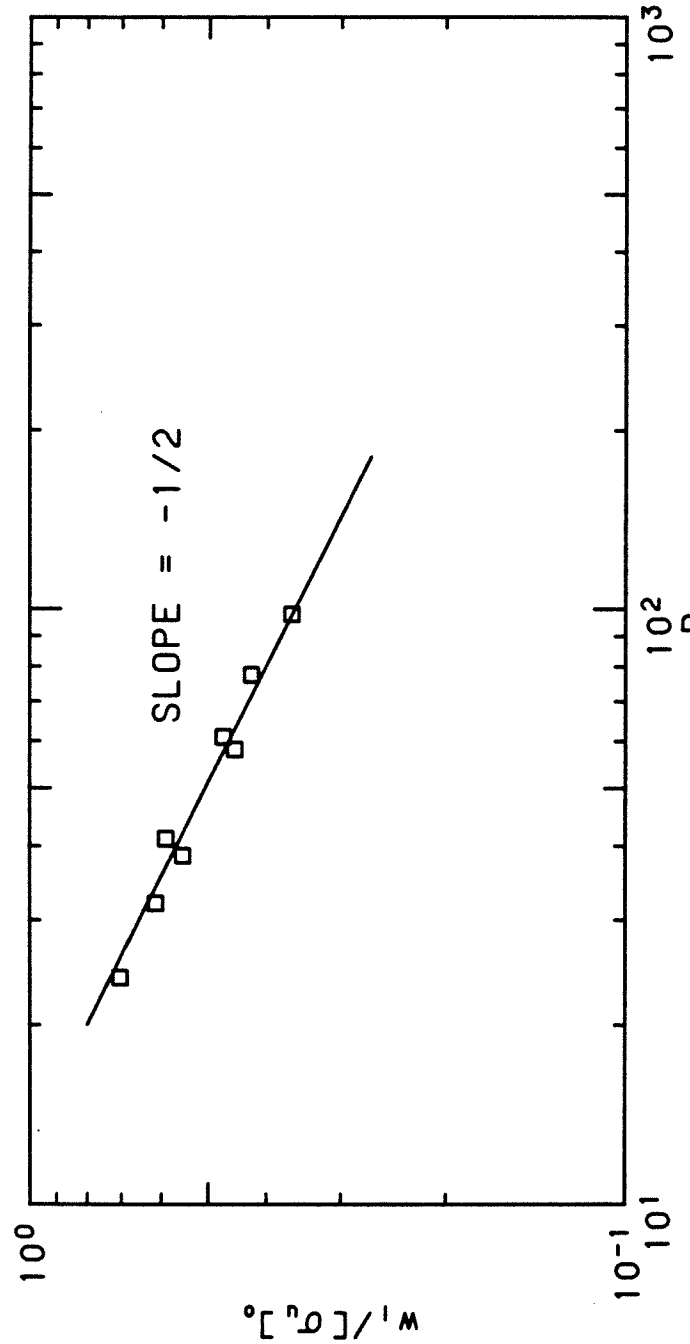

Figure 4.9: Variation of $w_1/[\sigma_u]_o$ with the overall Richardson number R_j

concentration as defined by adjacent pixels. The maximum value of the vertical concentration gradient was obtained and its average over time, denoted by $\overline{C'}$, was computed. The maximum average Brunt-Väisälä frequency in each experiment N_m was computed using $N_m^2 = (\overline{C'}/C_u)\Delta b^*$. A plot of $N_m^2/(\Delta b/L_o)$ versus R_j is shown in Figure 4.10. It can be seen that the data for $R_j < 50$ can be well represented by a relationship of the form $N_m^2/(\Delta b/L_o) \sim R_j^2$. At higher R_j the interface becomes sharp enough so that the calculation of $\overline{C'}$ becomes significantly affected by the limited spatial resolution. For example at $R_j = 61$ the calculated $\overline{C'}$ equals $0.49\ C_u/\Delta z$ where Δz is the spatial resolution of the camera which was 0.038 cm in that experiment. We anticipate that the effects of limited spatial resolution become important when $\overline{C'}$ is about $.5\ C_u/\Delta z$. As a result, we can conclude that at $R_j > 50$, we are underestimating N_m because of limited spatial resolution. Hence, the results for $R_j > 50$ should not be viewed with much confidence.

---

* It is worth noting that the concentration and density gradients are essentially equivalent if molecular diffusion is not important. This is the case because the fluid density is an almost linear function of the solute concentration, considering the very low solute concentrations used in this study (Weast 1976). As a result, the value of N_m based on the concentration gradient will be approximately equal to that obtained from using the density gradient when the above conditions are satisfied. Moreover, the diffusivities of the solutes used are close. κ for salt is 1.48×10^{-5} cm^2/sec (Weast 1976), that for alcohol is 1.24×10^{-5} cm^2/sec (Reid & Sherwood 1966), and the diffusivity of Rhodamine 6G may be estimated from formulas given in Reid & Sherwood (1966) to be about 0.8×10^{-5} cm^2/sec. When molecular diffusion becomes important, the tracer will not follow the solutes and the LIF method will breakdown.

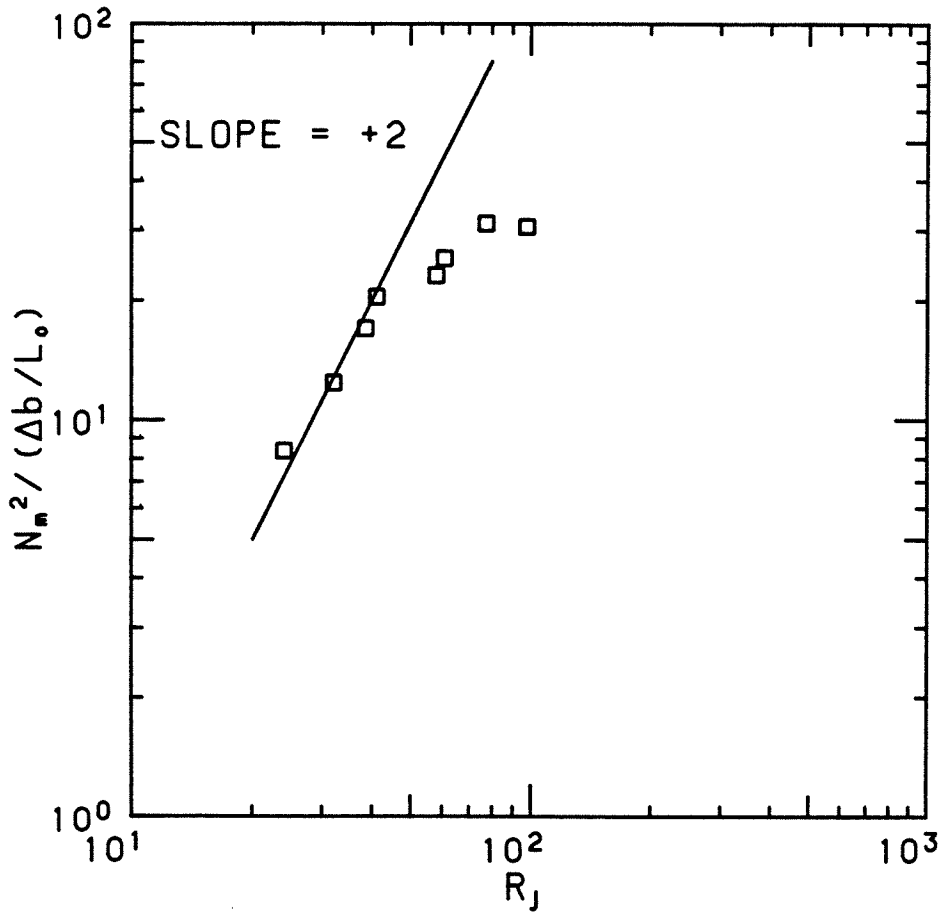

Figure 4.10: Variation of $N_m^2/(\Delta b/L_o)$ with the overall Richardson number R_j

They provide only a lower limit on $N_m^2/(\Delta b/L_o)$. If an interfacial layer thickness h_c is defined as $h_c = C_u/\overline{C'}$, then the $N_m^2/(\Delta b/L_o) \sim R_j^2$ relationship would lead to $h_c/L_o \sim R_j^{-2}$.

The results of saline density profile measurements at high P_e obtained by Crapper & Linden (1974) indicate that h/ℓ_o is constant with R_j. In Crapper & Linden's experiments h was determined by least-squares fitting a straight line to the central 50% of the data points (at least 20 points) in the interface and extending this line until it intersected the mean density in the upper and lower layers. In the instances when the interface is sufficiently sharp in our experiments the determination of the interfacial layer thickness by a method similar to that of Crapper & Linden is not possible. This is due to the fact that the number of points with concentrations between 0.25-0.75 C_u is usually much less than 20 and and can be as low as zero. This makes a direct comparison with the results of Crapper & Linden impossible. Although there is some difference in the method used to calculate h and h_c, it is thought that these differences cannot account alone for the discrepancies in the observed dependance of h/ℓ_o and h_c/L_o on R_j. It is also worth noting that values of h_c/L_o as small as 0.03 were observed in our experiments. This is much smaller than the h/ℓ_o = 1-1.5 values in Crapper & Linden. Some of the discrepancies in the interfacial thickness measurements may be due to the difference in spatial resolution between the two experiments. Crapper & Linden used a

conductivity probe traveling at 5 cm/s with a vertical resolution of 0.1 cm. Since the probe was traveling the actual resolution exceeds 0.1 cm and depends on the frequency response of the instrument and the "washing" of the probe. The vertical resolution in our experiments was in the range of 0.03-0.04 cm.

It is to be noted that the R_j range is limited in our experiments due to some practical considerations. At very small R_j the interface migrates very quickly, and as a result, we are not able to obtain records that are long enough for statistical purposes at fairly constant R_j. High values of R_j may be obtained by either increasing the density difference, increasing the depth of the upper layer, or decreasing the grid oscillation frequency. The latter option was not used because the Reynolds number would have been substantially lowered. Moreover, the density differences that were used were kept low so as to reduce the effects of refractive index fluctuations. The depth of the upper layer D was kept to below 25 cm to eliminate the undesirable wall effects observed by Fernando & Long (1983) at large D. Additionally, higher R_j values were not used because the resolution of the equipment becomes a limiting factor for $R_j > 50$.

4.3 Entrainment Model

Phillips (1977) has theoretically investigated the evolution of infinitesimal disturbances at a sharp density interface in the ocean in the absence of mean shear. He studied a case when the Brunt-Väisälä frequency is appreciable only within a small depth surrounding the thermocline. The analysis was focused on the lowest mode of the internal wave at the interface. For the case when the layer above the thermocline is only a small fraction of the local depth, Phillips showed that the frequency of the first mode internal waves ω is given by

$$\omega^2 = (\Delta b)[gk/(1+\coth(kd))],$$

where k is a horizontal wave number and d is the depth of the layer above the thermocline. In the special case that $k \sim 1/d$ the above relationship reduces to $\omega^2 = \Delta b/d$. This last relationship is equivalent to a result obtained in Section 4.2, namely $n_a^2 \sim \Delta b/L_o$, if we take into account that $L_o = 0.1D$.

Phillips then investigated the degradation of the first internal wave mode and considered the possibility of occurrence of a dynamic instability in the thermocline where the maximum rate of shear U'_m induced by the internal waves is maximum. He postulated that if the rate of shear induced by the lowest mode is large compared with the rate at which the basic flow changes, *i.e.*, if $U'_m \gg \omega$, then it might be anticipated that the stability criteria

developed for stratified shear flows (Miles 1961) would be relevant for the case of the lowest internal wave mode at a relatively sharp thermocline in the absence of mean shear. Motivated by the results of instability theory in stratified shear flows, Phillips investigated the possibility of occurrence of similar interfacial instabilities when the local gradient Richardson number $J < 1/4$ for the case of the lowest internal wave mode at a sharp density interface. The local gradient Richardson number J, defined as $J = (N_m/U'_m)^2$, was calculated by Phillips for this case to be

$$J = (N_m/\omega - \omega/N_m)^{-2} k^{-2} s^{-2},$$

where s is the amplitude of the thermocline displacement. When the wavelength of the internal wave is large compared with the thermocline thickness, *i.e.*, $\omega << N_m$, we obtain $J = (\omega/N_m)^2 (ks)^{-2}$. The condition $J = 1/4$ yields a limiting slope

$$(ks)_m = 2n_a/N_m \qquad (<< 1).$$

Phillips suggested that if the energy supply to the internal wave mode continues after the above limiting condition is attained, a local instability may develop, with a length scale of the order of the interfacial layer thickness, giving rise to a patch of intense, small scale turbulence. Phillips added that the energy acquired (and then ultimately dissipated) by the turbulence is at the expense

of the internal wave, so that an occasional local instability of this kind can restrict the magnitude of the internal waves in a similar fashion to the way breaking limits the growth of surface waves.

The possibility of the occurrence of such an instability in our experiments will be investigated next. To compare our experimental results with the theory we will take $s \sim \zeta$ since ζ is a measure of the amplitude of the interfacial waves. If we take $k \sim 1/L_o$ *, then it follows that $\omega \sim n_a$ and $J \sim (L_o/\zeta)^2 (n_a/N_m)^2$. The assumption that $n_a \ll N_m$ was used and is valid because in our experiments $N_m \sim 5$ Hz, whereas n_a as determined from visual observations of concentration contours is about 0.1 Hz. A plot of J_i, defined by $J_i = (L_o/\zeta)^2 (n_a/N_m)^2$, versus R_j, is shown in Figure 4.11 and indicates that J_i is constant with R_j ($R_j < 50$). For $R_j > 50$, the N_m values are significantly affected by the limited experimental spatial resolution as previously discussed, and as a result, we anticipate that the J_i values are overestimated. Actually, if we use the results from Section 4.2, *i.e.*, $\zeta \sim L_o R_j^{-1}$ and $N_m^2/(\Delta b/L_o) \sim R_j^2$ ($R_j < 50$), we obtain J_i = constant.

---

* The assumption that $k \sim 1/L_o$ implies that the wavelength of the lowest internal mode is set by the integral length scale of the turbulence near the interface (or equivalently the depth of the upper layer). The consequences of this assumption will be discussed later.

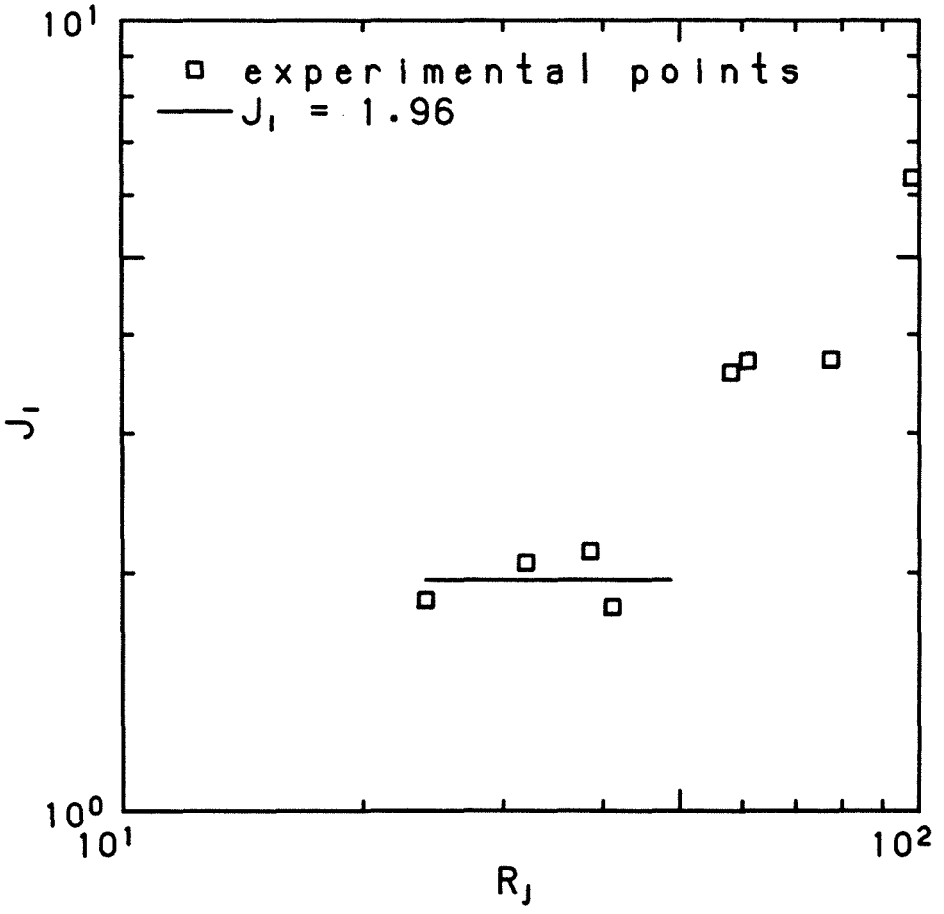

Figure 4.11: Variation of the local gradient Richardson number J_i with the overall Richardson number R_j

The facts that $n_a^2 \sim (\Delta b/L_o)$ and J = constant for a range of R_j, when viewed by themselves, may not provide sufficient evidence that an instability similar to the one discussed by Phillips (1977) is limiting the amplitude of the lowest mode waves. To further test the applicability of Phillips' theory to our experiments, we will compare the theoretical predictions of the amplitude of the interfacial displacement and the internal wave spectra with our experimental results.

Phillips (1977) had calculated the mean square displacement of the thermocline $\overline{\alpha_k^2}$ when the process of local breakdown described above limits the amplitude of a single wave train with wave number k. He found

$$\overline{\alpha_k^2} = 2n_a^2/(N_m k)^2 .$$

If most of the total energy resides in the lowest mode, as is usually the case when the thermocline is relatively sharp (Phillips 1977), then the internal wave amplitude is approximately determined by the mean square displacement of the thermocline due to the first mode. This implies that $s^2 \sim \overline{\alpha_k^2} = 2(\omega L_o/N_m)^2 \sim L_o^2 R_j^{-2}$, if we take $k \sim 1/L_o$ and $\omega \sim n_a$ for the lowest internal mode. This result is equivalent to our experimental observation in Section 4.2, namely $\zeta/L_o \sim R_j^{-1}$, if we take $s \sim \zeta$.

If the lowest mode waves are visualized as a random succession of wave groups at different wave-numbers, and if the growth of all wave-numbers is limited by an instability similar to the one discussed above, then the spectrum of the internal waves $\Phi(d,f)$ where f is the frequency is predicted (Phillips 1977) to be

$$\Phi(d,f) \sim (d\Delta b/N_m^2)f^{-1} \quad , \qquad f \ll \omega$$

$$\sim (\Delta b)^2 N_m^{-2} f^{-3} \quad , \qquad \omega \ll f \ll N_m .$$

An internal wave spectrum, obtained by a fast-Fourier transform applied to the $C/C_u = 0.5$ contour at $R_j = 24$ is presented in Figure 4.12. An f^{-3} range is observed for a range where $n_a < f < N_m$. Moreover, spectra from different experiments, normalized by $(\Delta b)^2 N_m^{-2}$ with $N_m^2 \sim (\Delta b/L_o)R_j^2$, are shown in Figure 4.13. All the spectra collapse, thus giving support for Phillips' theory. If we use the actual measured N_m to normalize the spectra for $R_j > 50$, the collapse is not as good. This might further indicate that N_m values in that range are significantly attenuated by the limited experimental spatial resolution.

The close agreement between our experimental results and the theory suggests the existence of a saturated wave field at the density interface and reveals that the process of local breakdown is limiting the growth of various wave number disturbances. The form

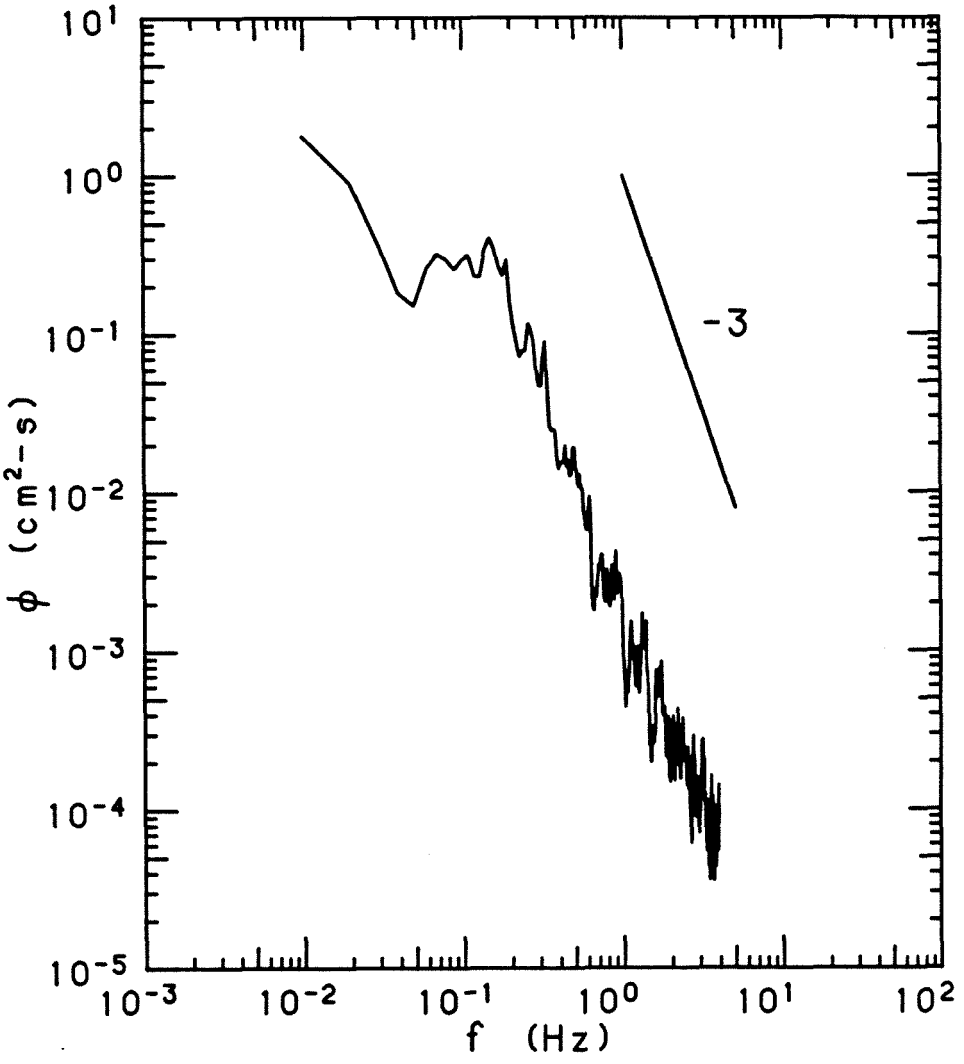

Figure 4.12: Internal wave spectrum Φ at R_j = 24

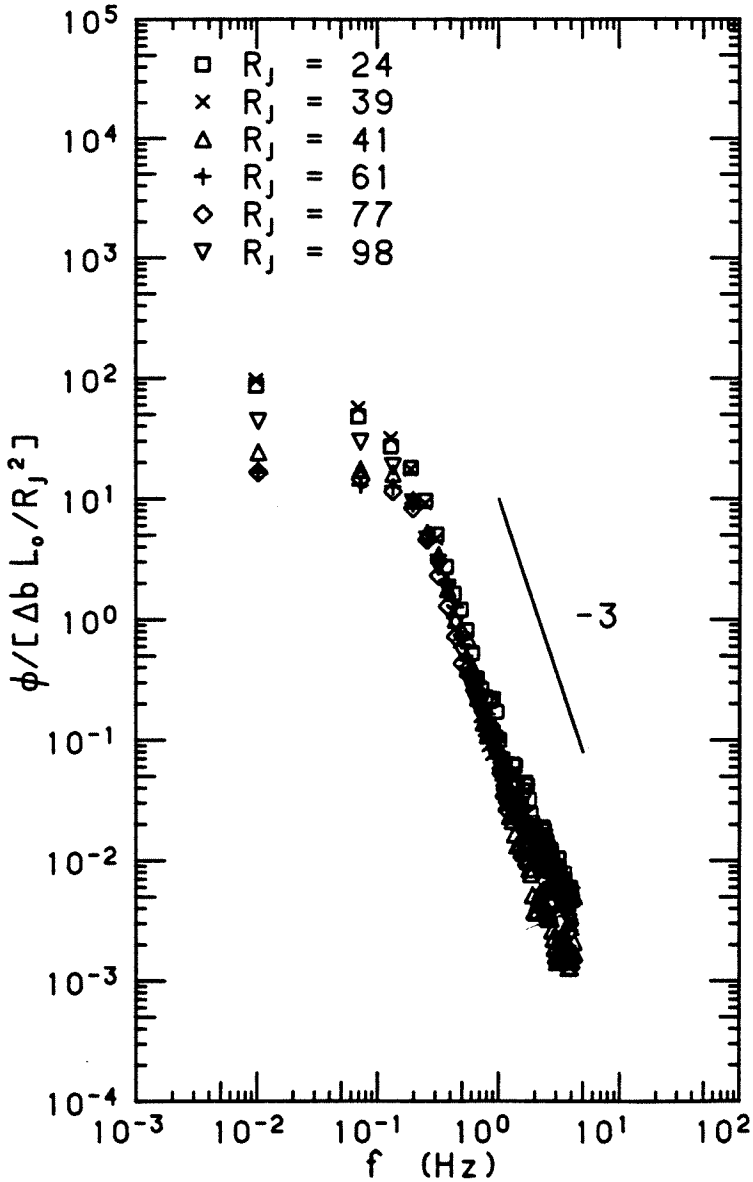

Figure 4.13: Normalized internal wave spectra $\Phi/(\Delta b L_o/R_j^2)$

of the spectra, the behaviour of the wave amplitude and frequency, as well as the constancy of J with R_j are all in agreement with the theoretical model. This agreement between the theory and the experiments, after invoking $k \sim 1/L_o$, suggests that this relationship might be valid, thus implying that the wavelength of the lowest mode internal waves is determined by the large turbulence scales. This is not surprising in view of the flattening of the large eddies near a density interface as observed in Chapter 3. As a result of this flattening, we might anticipate that the largest eddies in the mixed layer impose the largest horizontal length scale of the internal waves. The flow images shown in Figure 4.1 also provide qualitative support for the above theory in that they show that the breakdown of the internal waves is a sporadic intermittent process. The images also seem to indicate that the length scale of the interfacial instability is comparable with the thickness of the interface. The events marked A and E in Figures 4a and 4b clearly show that.

In order to calculate the rate of entrainment at a shear-free density interface, we have to determine (i) the volume of fluid entrained in individual mixing events and (ii) the frequency of occurrence of these events, f_m. The above theory indicates that the length scale of the interfacial instabilities is of the same order as the thickness of the interfacial layer. This suggests that the volume of fluid entrained per unit area per event is proportional to

h_c. The quantity f_m could not be determined in the experiments, but in general, it may be expressed as $f_m \tau_o = G(R_j)$ where G is some function. Furthermore, we may write:

$u_e \sim$ (volume entrained per event per unit area) x

(frequency of occurrence of mixing events)

or,

$$u_e \sim (h_c) \times f_m$$

thus,

$$u_e/[\sigma_u]_o \sim h_c\, f_m/[\sigma_u]_o \sim f_m\, \tau_o\, R_j^{-2}.$$

The experiments of Fernando & Long (1983) and Folse *et al* indicate that $u_e/(\sigma_u)_o \sim R_j^{-7/4}$ whereas Hopfinger & Toly (1976) and Turner (1968) found that $u_e/(\sigma_u)_o \sim R_j^{-3/2}$. These results imply either that $(f_m \tau_o) \sim R_j^{-1/4}$ or $(f_m \tau_o) \sim R_j^{-1/2}$ respectively. We may thus conclude that the frequency of mixing events is a decreasing function of R_j, a result which is in agreement with our visual observations in Figure 4.1.

It is anticipated that the decrease of h_c/L_o with R_j cannot continue indefinitely. We suggest that a lower limit on h_c at sufficiently high R_j is determined by molecular diffusion. A possible scaling of the interfacial thickness under these conditions is $h_c \sim (\kappa \tau_o)^{1/2}$ which yields $h_c/L_o \sim P_e^{-1/2}$. The latter result was observed in heat stratified experiments when the interface is governed by molecular diffusion (Crapper & Linden 1974). The above conjecture implies the existence of a cut-off region in which the

processes determining the interfacial structure are altered. The cut-off point is obtained when $h_c \sim L_o R_j^{-2}$ becomes of the same order as $(\kappa\tau_o)^{1/2}$, *i.e.*, $L_o R_j^{-2} \sim \kappa L_o/[\sigma_u]_o$. This yields an $R_j \sim P_e^{1/4}$ criterion for the onset of diffusive effects. In Figure 4.14 we plot $R_j P_e^{-1/4}$ = constant in the P_e-R_j plane. Below the line and sufficiently far from it we expect the interfacial structure to be governed by molecular effects. Sufficiently above the line the interfacial structure can be described by the local wave breakdown model as discussed in this chapter. It is also worth noting that for small enough R_j, say $R_j < (R_j)_a$, the buoyancy effects are not important and the upper layer grows in a similar fashion to a turbulent front in a homogeneous fluid.

4.4 Discussion

This chapter presents a simple model for turbulent entrainment at a shear-free density interface. The entrainment process and the interfacial structure are proposed to be, in general, functions of Peclet and overall Richardson numbers. The model suggests the existence of three distinct entrainment regimes where the interfacial dynamics are governed by different force balances. At very low R_j, *i.e.*, $R_j < (R_j)_a$, it is expected that the buoyancy effects are negligible and the mixed layer grows in a similar fashion to a turbulent front in a homogeneous fluid. For $(R_j)_a \ll R_j \ll \beta P_e^{1/4}$, where β is a constant, the interface may be

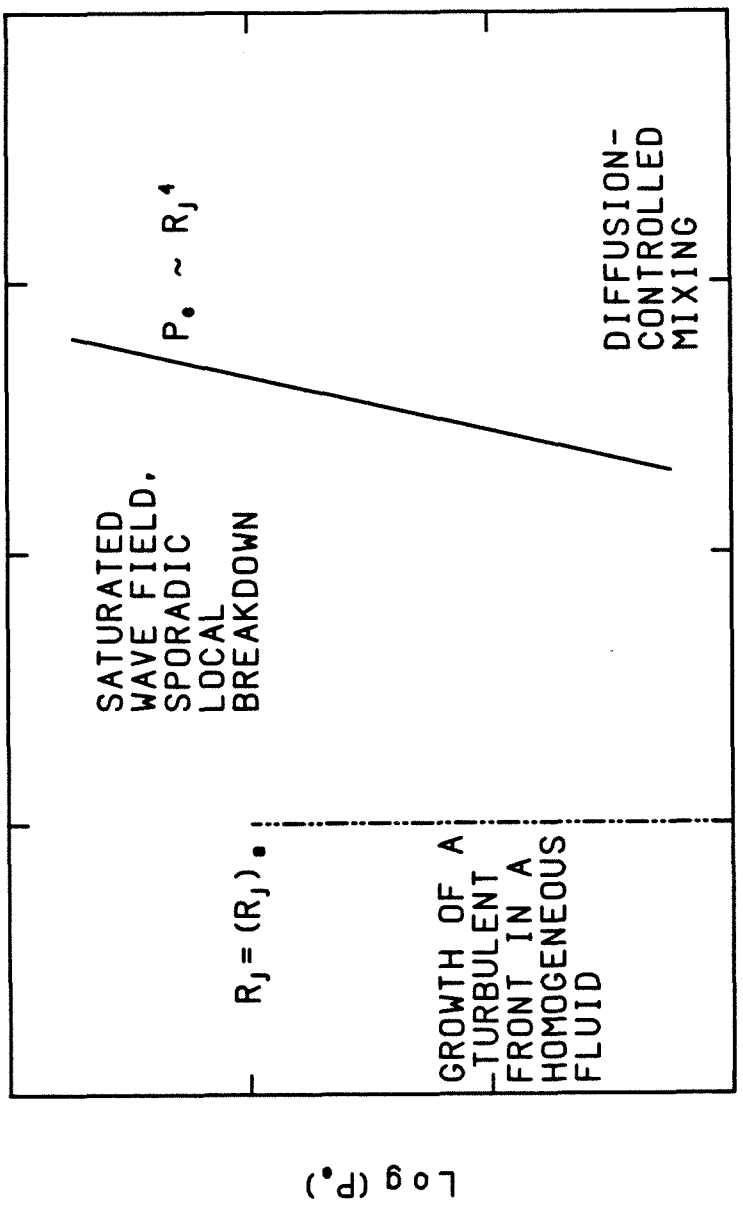

Figure 4.14: Different entrainment regimes for various values of the Peclet number P_e and the overall Richardson number R_j

characterized by the existence of a saturated wavefield and the occurrence of intermittent and sporadic local instabilities that provide a mechanism for fluid mixing. At $R_j >> \beta P_e^{1/4}$ the interfacial structure is governed by molecular diffusion.

Although no experiments were carried out within the last range, our experiments suggest that due to the sharpening of the interface with increasing R_j, molecular effects are bound to become important at sufficiently high R_j. For example, a simple calculation shows that for h_c of about 0.05 cm, as obtained in our experiments at $R_j = 98$, κ/h_c, which presents an estimate of the molecular flux, is about 2×10^{-4} cm/sec. The measured u_e at $R_j = 98$ is 8×10^{-4} cm/sec. This implies that the molecular flux contributes a significant amount to the total mass flux at $R_j = 98$. Actually, $h_c = .05$ cm at $R_j = 98$ provides a high estimate for the interfacial thickness. This is due to the limited spatial resolution of our equipment as discussed in Section 4.2. The above calculation suggests that molecular effects become important at $R_j \sim 10^2$ for $P_e \sim 10^5$. Turner's (1979) results suggest that molecular effects become important at $R_i \sim 10$ for his heat-stratified experiments. P_e in those experiments is estimated to be about a factor of 2000 lower than our experiments. The $P_e \sim R_j^4$ scaling for the onset of diffusive effects implies that, based on Turner's findings, we expect diffusive effects to become significant at $R_i \sim 10\ (2000)^{1/4} \sim 50$ in our experiments. Considering the

different methods for obtaining the integral length scale of the turbulence in the calculations of R_j and R_i and taking into account that the point at which the diffusive effects become important is not defined very precisely, the $P_e \sim R_j^{1/4}$ relationship seems to provide a good scaling for the onset of molecular effects when heat and salt experiments are compared.

When the interface is governed by molecular diffusion, *i.e.*, sufficiently below the $R_j P_e^{-1/4}$ = constant line, we anticipate that the rate of entrainment will be proportional to both the concentration gradient and the appropriate diffusivity κ, *i.e.*, $u_e \sim \kappa/h_c$. Denton & Wood (1981) had previously used a similar relationship with $h \sim \ell_o$ (or alternatively $h_c \sim L_o$) as determined by Crapper & Linden (1974) at high P_e. This leads to a $u_e/(\sigma_u)_o \sim P_e^{-1}$ relationship. If we use $h_c \sim (\kappa\tau_o)^{1/2}$ as suggested by our experiments we obtain $u_e/(\sigma_u)_o \sim P_e^{-1/2}$, a result which is in agreement with the findings of Fortescue & Pearson (1967) who determined the rate of entrainment at high R_j in the context of gas absorption into a water surface.

The model we are proposing is similar to the one presented by Denton & Wood (1981) but with the following major exceptions: (i) our model is valid at all P_e as opposed to the low P_e limitation in Denton & Wood's model and (ii) when the interface is governed by molecular diffusion we suggest a $u_e/(\sigma_u)_o \sim P_e^{-1/2}$ as opposed to the $u_e/(\sigma_u)_o \sim P_e^{-1}$ relationship proposed by Denton & Wood. The

differences between the $P_e^{-1/2}$ and P_e^{-1} relationships may be significant. In particular, the $P_e^{-1/2}$ dependence, when taken in conjunction with $h_c/L_o \sim R_j^{-2}$, provides a criterion for the onset of molecular effects that is in agreement with the experimental findings as discussed above. On the other hand, the $u_e/(\sigma_u)_o \sim P_e^{-1}$ relationship, when used with $h/\ell_o \sim$ constant, cannot predict the prevalance of molecular effects at high P_e as observed in our experiments.

Turner (1979) had reported that in heat stratified experiments by C.G.H. Rooth, where P_e was varied over a wide range, an $R_j^{-3/2}$ range was observed. As P_e was reduced, the curves broke away from the $R_j^{-3/2}$ line at successively lower values of R_j, rising above it with decreased slope as molecular diffusion increases the transfer rate. This last observation is in qualitative agreement with our model.

Our model suggests that for $(R_j)_a \ll R_j \ll \beta P_e^{1/4}$, the turbulence in the upper layer induces the internal wavefield at the interface. Furthermore, it is the breakdown of these internal waves that generates local mixing events. This turbulence-wave-turbulence model is different from some earlier ideas about mixing near a shear-free density interface, which postulated that the large eddies in the mixed layer are directly responsible for entraining unstirred layer fluid. For instance, Turner (1968) suggested that the mixed layer turbulent eddies directly entrain unstirred layer fluid which

becomes ultimately incorporated in the mixed layer. Moreover, Linden (1975) suggested that the rate of change of potential energy is proportional to the kinetic energy flux near the interface. Such an energy argument indicates that the kinetic energy of the eddies is directly converted into potential energy as the eddies impinge on the interface. The work of Linden (1973), in which he studied the effects of vortex rings impinging on a sharp density interface, also suggests that the entrainment occurs after each eddy impinges on the density interface. Although Linden (1973) postulated that the mixing occurs after the recoil of the interface and not by direct entrainment of fluid by the large eddies, the main idea is that mixing occurs after the arrival of every eddy at the interface. However, our flow images in Figure 4.1, the flattening of the eddies near the density interface (Chapter 3), and the observations concerning the internal wave field in Section 4.2 all suggest that the mixing is a result of local wave breakdown and is not due to direct entrainment of unstirred layer fluid by the individual large turbulent eddies. The major idea in our work is that the mixing is occurring sporadically and intermittently and is related to the mixed layer turbulence only through the internal wavefield. Moreover, it is also thought that the turbulence in the upper layer is not very essential for the growth and the instability of the internal wave field. Alternatively, irrotational disturbances in one fluid layer may yield similar interfacial structure and dynamics as in our experiment. Actually, Phillips' (1977) theory assumes

irrotational flow near the density interface. The close agreement between our experimental results and the theory suggests that the rotational aspect of the oscillating grid induced turbulence may not be very essential to the problem.

Although the large turbulent eddies in our experiments are flattened at the density interface and the mixing occurs intermittently as postulated by Long (1978), the model proposed in Section 4.3 is essentially different from Long's arguments. Two major differences between our experimental results and Long's model are in the functional dependence of the interfacial wave velocities and the interfacial thickness on the overall Richardson number. In our experiments, we find that h_c/L_o is a fast decreasing function of R_j as opposed to h/ℓ_o = constant in Long's model. Moreover, we find that $w_i/[\sigma_u]_o \sim R_j^{-1/2}$ as opposed to $w_h/(\sigma_u)_o \sim R_i^{-1/4}$ as predicted by Long where w_h is defined as the r.m.s. vertical velocity of the interfacial waves. Although the definitions of w_i and w_h may be slightly different, the $w_i/[\sigma_u]_o \sim R_j^{-1/2}$ relationship provides a better fit to our data than a $w_i/[\sigma_u]_o \sim R_j^{-1/4}$ relationship. Furthermore, Long's model cannot account for the significant molecular mass flux that was observed in our experiments at $P_e \sim 10^5$ and $R_j \sim 10^2$.

The realization that molecular effects might be important even at $P_e \sim 10^5$ provides a possible interpretion of some of the observations of Wolanski & Brush (1976). They suggested that the

rate of entrainment is a function of both an overall Richardson number and a Prandtl number $P_r = \nu/\kappa$. An inspection of their entrainment rate versus Richardson number plots suggests that the various curves corresponding to different solutes (except for the case of clay as a "solute") may be viewed as breaking away from an R_j^{-n} line (with n about 2) at values of R_j that become succesively higher as P_r (and consequently P_e, since ν is almost constant) increases. This is in qualitative agreement with our model. A more quantitative comparison is difficult to make because the errors involved in translating Wolanski & Brush's form of the overall Richardson number to a form similar to the one used in this analysis might be large. It is worth mentioning that Wolanski & Brush concluded that their non-dimensionalized entrainment rates are independent of P_e. However, our model predicts that the dependence of the entrainment rate on P_e is variable and depends on the location in the P_e-R_j plane. In any event, our model shows that the dependence on P_e is slow and in the extreme case is given by $u_e/[\sigma_u]_o \sim P_e^{-1/2}$. In suggesting that the entrainment rate is independent of P_e, Wolanski & Brush varied P_e by about a factor of 3. If we take into account the amount of scatter in their data points we cannot rule out a P_e^{-m} dependence with $m \lesssim 1/2$.

The results of our experiments indicate that the density interface is very effective in limiting the transfer of vorticity to the unmixed layer. It is thought that the generation of vorticity

due to baroclinic effects prevents the large turbulent eddies from overturning near the density interface. As a result, the interfacial waves are excited as the vorticity near the interface is countered by the baroclinic vorticity generation. Moreover, it is anticipated that small scale rotational motions are not very affected by the presence of the density interface, and thus are able to overturn.

CHAPTER 5

SUMMARY; SUGGESTIONS FOR FUTURE RESEARCH

5.1 Summary

In this work, the interaction of a sharp density interface with oscillating grid induced shear-free turbulence was experimentally investigated. Only one fluid layer was stirred and potential refractive index fluctuation problems were avoided by using solutes that provided a homogeneous optical environment. Laser-induced fluorescence was used to measure the concentration of a tracer. This technique, when used in conjunction with a photodiode array, is capable of providing both temporal and spatial resolution unattainable by conventional methods. Moreover, the technique is nonintrusive and, when combined with a fast data acquisition system, provides an unprecedented amount of information about the structure and dynamics of the flowfield. A laser-Doppler velocimeter was also used to measure the vertical component and one horizontal component of velocity in and above the density interface and at a point where tracer concentration was also measured. Turbulence intensities, energy spectra, turbulent kinetic energy, and turbulent kinetic energy fluxes were measured. Moreover, internal wave spectra, amplitudes, velocities, as well as the vertical mass flux were experimentally determined. The major findings of this study are

summarized below:

1. The horizontal r.m.s velocity σ_u is amplified and the vertical r.m.s. velocity σ_w is sharply attenuated in a layer adjacent to the density interface. This can be regarded as being due to the flattening of the turbulent eddies near the density interface. The point at which the maximum amplification in σ_u occurs is about 0.1-0.2 integral length scales away from the interface. The effect of the interface on the turbulence extends to about one integral length scale from the interface.

2. The energy spectra of the vertical velocity fluctuations show that there is preferential attenuation of low frequencies (large scales) as the interface is approached. On the other hand the horizontal energy spectra indicate that there is substantial gain at the low frequency end of the spectrum. This indicates that the density interface is efficient in altering large eddies. Both the horizontal and vertical spectra indicated that the high frequency motion was not significantly affected by the presence of the interface.

3. The experiments indicate that the density interface acts, at least qualitatively, in a manner similar to a rigid flat plate inserted in the flow. The attenuation of the vertical velocity, the amplification of the horizontal velocities, the kinetic energy distribution, and the form of the energy spectra exhibit similar

trends in both cases.

4. The results of turbulence measurements for both the density interface and the rigid flat plate indicate strong qualitative (and sometimes quantitative) agreement with the postulates of the theory of Hunt & Graham (1978). In particular, the amplification of the horizontal velocities accompanied by a sharp reduction in the vertical velocity, the form of the energy spectra, and the distance up to which the effect of the interface/wall is felt are all in accordance with the predictions of Hunt & Graham's theory. One observation which is not in good agreement with the results of Hunt & Graham is the magnitude of the amplification of the horizontal turbulent velocity. Near both the density interface and the flat plate, σ_u is amplified by as much as 40% as opposed to a maximum of 22% predicted by Hunt & Graham. The discrepancy may be due to the increased values of the energy flux divergence near the density interface and the flat plate.

5. From simultaneous concentration and velocity records as well as motion picture films, it was determined that fluid mixing occurs in intermittent, sporadic bursts. These bursts are a result of local interfacial instabilities that are not directly related to individual eddies impinging on the interface.

6. The local gradient Richardson number $J_i = (L_o/\zeta)^2 (n_a/N_m)^2$ (where L_o is the integral length scale of the turbulence near the interface, ζ and n_a are measures of the internal wave amplitude and vertical velocity respectively, and N_m is the maximum averaged Brunt-Väisälä frequency) is constant for a certain range of the overall Richardson number R_j. R_j is defined as $R_j = \Delta b L_o / [\sigma_u]_o^2$ where Δb is the buoyancy jump across the interface and $[\sigma_u]_o$ is a r.m.s. horizontal velocity near the interface. In that range, it was found that $\zeta/L_o \sim R_j^{-1}$ and that the vertical wave velocity at the interface obeys a $w_i/[\sigma_u]_o \sim R_j^{-1/2}$ relationship. Moreover, it was experimentally determined that $N_m^2/(\Delta b/L_o) \sim R_j^2$. This last relationship implies that the thickness of the interfacial layer is a rapidly decreasing function of R_j. It was also found that the internal wave spectra decay as f^{-3} at frequencies below the maximum Brunt-Väisälä frequency.

7. The form of the internal wave spectra, the behavior of the internal wave amplitude and frequency, as well as the constancy of J with R_j (for a certain R_j range), are all in agreement with a theoretical model proposed by Phillips (1977), in which the internal waves are limited in their spectral density by sporadic local instabilities and breakdown to turbulence. The instabilities occur when the maximum rate of shear induced by the lowest mode internal wave is large compared with the rate at which the basic flow changes. The occurrence of such an instability, with a length scale

of the order of the interfacial layer thickness, gives rise to a patch of intense, small scale turbulence. The energy acquired (and ultimately dissipated) by the turbulence is at the expense of the internal waves, so that an occasional local instability of this kind can restrict the magnitude of the internal waves in a similar fashion to the way breaking limits the growth of surface waves.

8. A simple generalized model for turbulent entrainment at a shear-free density interface was presented in Chapter 4. In that model, the interfacial structure and the entrainment process are proposed to be functions of Peclet and overall Richardson numbers. The model suggests the existence of three distinct entrainment regimes where the interfacial dynamics are governed by different force balances. At very low R_j, say $R_j \ll (R_j)_a$, the buoyancy effects are negligible and the mixed layer grows in a similar fashion to a turbulent front in a homogeneous fluid. For $(R_j)_a \ll R_j \ll \beta P_e^{1/4}$, where β is some constant, the interface may be characterized by the existence of a saturated wavefield and sporadic local instabilities that provide a mechanism for fluid mixing as discussed in the preceding paragraph. At $R_j \gg \beta P_e^{1/4}$, the interfacial structure is governed by molecular diffusion. Although no experiments were carried out in this range, our results suggest that, due to the sharpening of the interface with increasing R_j, molecular effects are bound to become important at sufficiently high R_j. These diffusive effects become significant when the

interfacial thickness h_c becomes of the same order as that of a diffusive interface, *i.e.*, $(\kappa\tau_o)^{1/2}$, as observed by Crapper & Linden (1974). Our experiments suggest a value of β of about 5 and the experiments of Turner (1968) suggest a value of $(R_j)_a$ on the order of 1.

9. Our model suggests that for $(R_j)_a \ll R_j \ll \beta P_e^{1/4}$ the turbulence in the mixed layer induces the internal wavefield at the interface. Furthermore, it is the breakdown of these internal waves that generates local patches of turbulent fluid that are responsible for mixing. This turbulence-wave-turbulence model is different from some earlier ideas about mixing near a shear-free density interface, which postulated that the large eddies in the mixed layer are directly responsible for entraining unstirred layer fluid (Turner 1968, Linden 1975). Such arguments imply that the kinetic energy of the eddies is directly converted into potential energy as the eddies impinge on the interface. However, our experimental results suggest that the mixing is a result of local wave breakdown and is not due to direct entrainment of unstirred layer fluid by individual large turbulent eddies. The major idea in our work is that the mixing is related to the mixed layer turbulence only through the internal wave field. Moreover, the turbulence in the upper layer may not have been essential for the growth and instability of the internal wave field. Alternatively, it is thought that irrotational disturbances in one fluid layer might yield similar interfacial structure and

dynamics as in our problem. Actually, Phillips' theory assumes irrotational flow near the interface. The close agreement between our experiments and the theory suggests that the rotational aspect of the turbulence may not be very essential in this problem.

10. The results of this study may be useful in the development and improvement of one-dimensional reservoir models. Although the turbulence in a reservoir may have different characteristics from those of oscillating grid induced shear-free turbulence, there are instances in nature when the mean shear is small. One such example is when the turbulence is produced by heating or cooling at the surface. In such instances, the results of our model may be readily applied to predict the dynamics of mixing and the structure of density interfaces in reservoirs.

5.2 Suggestions for Future Research

There are several important topics in density-stratified fluid flow in need of further research. Some of these topics are suggested by the findings of our investigation and will be discussed in this section.

An important by-product of this study was the realization of the importance of limitations due to the experimental equipment. There has been a tendency in density-stratified studies to ignore such limitations and as a result interpret measurements beyond their

significance. One such example is in the use of travelling conductivity probes. In many studies, the temporal and spatial resolution of the probes was not reported and/or determined on site. Moreover, errors due to the boundary-layer washing of such probes were mostly left unaccounted for. As a result, the resolution of travelling probes in some previous oscillating grid experiments may not have been adequate. Furthermore, some discrepancies in the literature about interfacial thickness measurements may be attributed to poor resolution as determined in the present experiments. As a result, the need for higher resolution equipment, both temporally and spatially, is of utmost importance for successful experimental investigations of density-stratified flows. In this day and age, many alternatives are present and the most promising among them are perhaps the optical-based techniques, since they do not disturb the flow. It is thought that the use of some advanced techniques, such as one and two-dimensional photodiode arrays for measuring both concentrations and velocities, will prompt numerous advances in our understanding of stratified flows.

One particular problem where the techniques used in this study might be useful is the study of turbulent stratified shear flows. This problem is considerably more complex than the shear-free case because it involves more variables. However, it might be worth while to test the applicability of a model similar to the one proposed in the present investigation and determine whether a simple

turbulence-wave-turbulence model is applicable.

Another interesting problem that was suggested by this investigation is the study of the interaction of turbulence with interfacial waves. Our investigation presented a very special case in which both the length and velocity scales of the turbulence were imposed. Moreover, our work constituted a first-order approach based on the gross quantities involved, such as the turbulence integral length scale and the lowest mode internal waves. It will be of interest to predict the higher mode internal waves when subjected to a variety of turbulence conditions. Moreover, the evolution of internal waves in the presence of mean velocity shear needs further investigation. Such studies may be analogous to investigations of the evolution of surface waves when subjected to turbulence in the lower atmosphere.

The simplified configuration of the experimental conditions in this study as well as the availability of detailed experimental results render the present problem an attractive candidate for numerical modelling. The outline for such a model might include (i) simulation of the oscillating grid induced turbulence, (ii) modelling of the turbulence-internal wave interactions, and (iii) predicting the occurence of interfacial instabilities and the associated mixing.

REFERENCES

Bouvard, M. & Dumas, H. 1967. The measurement of turbulence in water by the hot wire method. Part 2: Measurement procedure and results. La Houille Blanche 22, 723.

Crapper, P.F. & Linden, P.F. 1974. The structure of turbulent density interfaces. J. Fluid Mech. 65, 45.

Cromwell, T. 1960. Pycnoclines created by mixing in an aquarium tank. J. Mar. Res. 18, 73.

Denton, R.A. & Wood, I.R. 1981. Penetrative convection at low Peclet number. J. Fluid Mech. 113, 1.

Drain, L.E. 1980. *The Laser Doppler Technique.* John Wiley & Sons.

Durst, F., Melling, A. & Whitelaw, J.H. 1976. *Principles and Practice of Laser-Doppler Anemometry.* Academic Press, London.

Fernando, H.J.S. 1986. Molecular diffusive effects in stratified turbulent mixing. *Advancements in Aerodynamics, Fluid Mechanics, and Hydraulics.* (Editors Arndt, R. & Stephen, H.)

Fernando, H.J.S. & Long, R.R. 1983. The growth of a grid-generated turbulent mixed layer in a two-fluid system. J. Fluid Mech. 133, 377.

Fernando, H.J.S. & Long, R.R. 1985a. Mixed-layer growth in stratified fluids. *The Ocean Surface: Wave Breaking, Turbulent Mixing and Radio Probing.* (Editors Y. Toba and H. Mitsuyasu), 541.

Fernando, H.J.S. & Long, R.R. 1985b. On the nature of the entrainment interface of a two-layer fluid subjected to zero-mean shear turbulence. J. Fluid Mech. 151, 21.

Fernando, H.J.S. & Long R.R. 1985c. The growth of a shear-free mixed layer in a linearly stratified fluid. Phys. Fluids. 28, 2999.

Fischer, H.B. et al 1979. *Mixing in Inland and Coastal Waters.* Academic Press. 483 pp.

Folse, R.F., Cox, T.P., and Schexnayder, K.R. 1981. Measurements of the growth of a turbulently mixed layer in a linearly stratified fluid. Phys. Fluids. 24, 396.

Fortescue, G.E. & Pearson, J.R.A. 1967. On gas absorption into a turbulent fluid. Chem. Eng. Sci. 22, 1163.

Gartrell, G. 1979a. Studies on the mixing in a density-stratified shear flow. Ph.D thesis. California Institute of Technology.

Gartrell, G. 1979b. A signal processor for a laser-Doppler velocimeter. W.M. Keck Laboratory of Hydraulics and Water Resources Technical Memorandum 78-5. California Institute of Technology.

Hannoun, I.A. 1986. Use of the Reticon array camera. W.M. Keck Laboratory of Hydraulics and Water Resources Technical Memorandum 86-1. California Institute of Technology.

Hopfinger, E.J. & Linden, P.F. 1982. Formation of thermoclines in zero-mean shear turbulence subjected to a stabilizing buoyancy flux. J. Fluid Mech. 114, 157.

Hopfinger, E.J. & Toly, J.A. 1976. Spatially decaying turbulence and its relation to mixing across density interfaces. J. Fluid Mech. 78, 155.

Hunt, J.C.R. 1984. Turbulence structure in thermal convection and shear-free boundary layers. J. Fluid Mech. 138, 161.

Hunt, J.C.R. & Graham, J.M.R. 1978. Free-stream turbulence near plane boundaries. J. Fluid Mech. 84, 209.

Kantha, L.H. & Long, R.R. 1980. Turbulent mixing with stabilizing surface buoyancy flux. Phys. Fluids 23, 2142.

Kantha, L.H. , Phillips, O.M. & Azad, R.S. 1977. On turbulent entrainment at a stable density interface. J. Fluid Mech. 79,753.

Kato, H. & Phillips, O.M. 1969. On the penetration of a turbulent layer into a stratified fluid. J. Fluid Mech. 37, 643.

Kitaigorodski, S.A. 1979. Review of the theories of wind-mixed layer deepening. Marine Forecasting, Elsevier Oceanographic Ser. 25, 1.

Komori, S., Ueda, H., Ogino, F. & Mizushina, T. 1983. Turbulence structure in stably stratified open channel flows. J. Fluid Mech. 130, 13.

Koochesfahani, M.M. 1984. Experiments on turbulent mixing and chemical reaction in a liquid mixing layer. Ph.D thesis. California Institute of Technology.

Linden, P.F. 1975. The deepening of a mixed layer in a stratified fluid. J. Fluid Mech. 78, 385.

Linden, P.F. 1973. The interaction of a vortex ring with a sharp density interface: A model for turbulent entrainment. J. Fluid Mech. 60, 467.

Liu, H.T. et al 1977. Application of a fluorescence technique to dye-concentration measurements in a turbulent jet. *NBS special publication 484, in Proc. Symp. on Flow in Open Channels and Closed Conduits* held at NBS, Gaithersburg, MD, February 1977.

Long, R.R. 1978. A theory of mixing in stably stratified fluids. J. fluid Mech. 84, 113.

McDougall, T.J. 1979a. Measurements of turbulence in a zero-mean shear mixed layer. J. Fluid Mech. 94, 409.

McDougall, T.J. 1979b. On the elimination of refractive index variations in turbulent density stratified flows. J. Fluid Mech. 93, 83.

Papanicolaou, P.N. 1984. Mass and momentum transport in a turbulent buoyant vertical axisymmetric jet. Ph.D thesis. California Institute of Technology.

Papantoniou, D.P. 1986. Observations in turbulent buoyant jets by use of laser-induced fluorescence. Ph.D thesis. California Institute of technology.

Phillips, O.M. 1977. *Dynamics of the Upper Ocean.* Cambridge University Press.

Reid, R.C. & Sherwood, T.K. 1966. *The Properties of Gases and Liquids.* McGraw-Hill.

Reticon (1981). LC300A Camera Manual. EG&G Reticon.

Rouse, H. & Dodu, J. 1955. Turbulent diffusion across a density discontinuity. La Houille Blanche 4, 522.

Scavia, D. & Robertson, A. (Editors) 1981. *Perspectives on Lake Ecosystem Modeling.* Ann Arbor Science.

Tennekes, H. 1975. Eulerian and Lagrangian time microscales in isotropic turbulence. J. Fluid Mech. 67, 561.

Thomas, N.H. & Hancock, P.E. 1977. Grid turbulence near a moving wall. J. Fluid Mech. 82, 481.

Thompson, S.M. & Turner, J.S. 1975. Mixing at an interface due to turbulence generated by an oscillating grid. J. Fluid Mech. 67, 349.

Turner, J.S. 1979. *Buoyancy Effects in Fluids*. Cambridge University Press.

Turner, J.S. 1968. The influence of molecular diffusivity on turbulent entrainment across a density interface. J. Fluid Mech. 33, 639.

Uzkan, T. & Reynolds, W.C. 1967. A shear-free turbulent boundary layer. J. Fluid Mech. 28,803.

Wang, J. & Wu, J. 1985. Wind induced water turbulence: *The Ocean Surface: Wave Breaking, Turbulent Mixing and Radio Probing*. (Editors Y. Toba and H. Mitsuyasu), 401.

Watrasiewicz, B.M., & Rudd, M.J 1976. *Laser-Doppler Measurements*. Butterworth, London.

Weast, R.C. (editor) 1976. *Handbook of chemistry and physics*. 56th edition. C.R.C. Press.

Wolanski, E.J. & Brush, L.M. 1976. Turbulent entrainment across stable density step structures. Tellus 27, 259.

Wu, J. 1973. Wind induced turbulent entrainment across a stable density interface. J. Fluid Mech. 61, 275.

APPENDIX A

MATCHING THE REFRACTIVE INDEX IN DENSITY-STRATIFIED FLOWS

A.1 Introduction

The use of optical methods such as LDV and LIF in experimental fluid mechanics is becoming very common. The greatest advantage of such methods is that measurements are made without disturbing the flow. A major impediment to using optical methods to study density-stratified flows is the variation of the refractive index within the flow field. McDougall (1979a) has proposed a method for the reduction of refractive index variations while maintaining a density difference. The method relies on the fact that various solutes in, say water, can contribute to the density and to the refractive index of the solution in different proportions.

A new pair of solutes (ethanol and NaCl) were found to be suitable for use in LDV and LIF studies of stratified flows. In some circumstances the new pair is more useful than that described by McDougall (1979a).

A.2 Practical Considerations

Consider two solutes A and B dissolved in water. The refractive index i_{AB} and density ρ_{AB} of an aqueous solution of both A and B may be expanded as

$$i_{AB} = 1.3330 + a_{i1}C_A + a_{i2}C_A^2 + b_{i1}C_B + b_{i2}C_B^2 + c_i C_A C_B + \text{higher order terms} \qquad (A.1)$$

$$\rho_{AB} = 0.9982 + a_{\rho 1}C_A + a\rho_2 C_A^2 + b_{\rho 1}C_B + b_{\rho 2}C_B^2 + c_\rho C_A C_B + \text{higher order terms } (g/cm^3), \qquad (A.2)$$

where C_A is the concentration of component A (defined as mass of component A / total volume of solution), C_B is the concentration of component B, and the a's, b's, and c's are constants.

To prepare two solutions of solutes A and B, respectively, having the same refractive $i_A = i_B$ (where i_A is the refractive index of the solution containing solute A), but with a prescribed density difference $\Delta\rho$, two considerations have to be kept in mind:

(1) There is an upper limit on $\Delta\rho$ that can be achieved. This is due to non-linear terms in equation (A.1).

(2) No double diffusive convection (salt fingering) should occur at the interface.

As for the first limitation, it is to be observed that the refractive index i_{AB} of a mixture of the two solutions is generally different from i_A. The maximum difference between i_A and i_{AB},

denoted by $\max|i_{AB} - i_A|$, is an increasing function of $\Delta\rho$ as shown in figure A.1. A certain optical method will break down when $\max|i_{AB} - i_A|$ exceeds Δi_{all} (or $\Delta\rho$ exceeds $\Delta\rho_{max}$) where Δi_{all} is the maximum allowable change in the refractive index. It is to be noted here that Δi_{all} is a function of both the distance the beams traverse through an interface and the type of optical application. In general, the longer the beam path, the smaller is Δi_{all} for equal performance. Moreover, Δi_{all} for an LDV application is in general different from that for LIF measurements. It was found experimentally that a value of $\max|i_{AB} - i_A|$ of about 0.0001 may affect the quality of LDV measurements when the beams traverse 30 cm of interface.

To avoid double diffusive phenomena, a certain relationship has to be satisfied by the solutes. McDougall (1979a) discusses this problem at length and concludes that the relationship is very stringent and excludes most pairs of solutes. In his experiments, McDougall (1979a) used Epsom salt ($MgSO_4$) and sugar as solutes with the sugar solution being less dense. In this work we propose the use of common salt (NaCl) and ethanol as solutes. By using this pair of solutes double diffusive phenomena are eliminated since both solutes are stably stratified. (An ethanol solution is less dense than pure water).

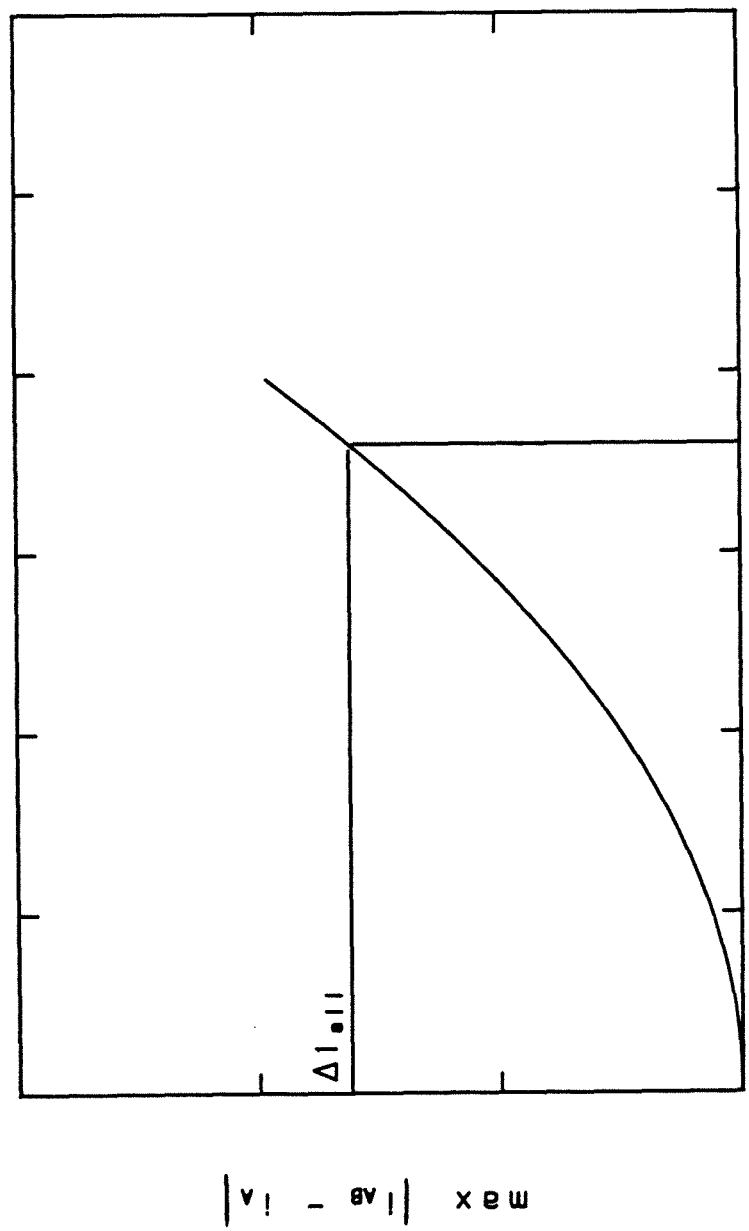

Figure A.1: Typical variation of max $|i_{AB} - i_A|$ with $\Delta\rho$.
$\Delta\rho_{max}$ is the value of $\Delta\rho$ corresponding to Δi_{all}

The use of salt and ethanol has an advantage in applications where the volume of the lower denser layer is large and the upper layer is relatively small. In that case the use of table salt/ethanol instead of Epsom salt/sugar is more economical. Moreover, the use of sugar in the lab can be impractical because it tends to stick to surfaces and supports the growth of microorganisms. However, the use of salt/ethanol has its own disadvantages. First, there is a significant temperature increase when alcohol is added to water. This can be remedied by either adding ice or waiting for the solution to attain its equilibrium temperature. The second is that alcohol is volatile. This can be a handicap when the upper layer is vigorously mixed. One way around this problem is to cover the tank. If only 95% of the surface is covered, negligible amounts of alcohol escape within several hours in the presence of mixing.

A.3 Experimental Verification

The application of the method was tested using an LDV system in the tank described in Chapter 2. Two different solutions were prepared: one containing salt and the other containing ethanol. Approximate amounts of both solutes were added so as to get two solutions with close refractive indices and a density difference of 0.021 gm/cm^3. The amounts were determined from tables of refractive

indices and density versus mass of solute added as published in Weast (1976). It was found that obtaining two solutions of the same refractive index by relying on published tables alone can be very frustrating. The main reason is the presence of impurities in both the solutes and the water. A refractometer proved invaluable in determining the difference in the refractive indices of the two solutions. The refractometer used was an American Optical model 10419 that provided readings to within 0.0001. Appropriate amounts of solutes were added to match the indices within the tolerance of the refractometer.

In order to match the refractive indices to within less than the tolerance of the refractometer, ethanol solution was injected from a dropper into a rectangular plexiglass box 6 x 6 x 15 cm (l x w x h) that contained the salt solution. The resulting plume was observed on a shadowgraph. Then, the concentration of the ethanol solution was adjusted very slowly by adding either very small amounts of ethanol or water and the resulting solution was injected into the plexiglass box. This trial and error procedure continued until the plume was not visible on the shadowgraph. At that point the ethanol solution was carefully poured over the salt solution in the large tank after ample time was allowed for the ethanol solution to reach its equilibrium temperature.

The upper fluid was disturbed vigorously using manual power. LDV measurements were performed by using laser beams that traversed the tank horizontally through the interface and measurements were made throughout the interfacial layer. Details of the LDV system are described in Chapter 2. The LDV output signal was continuous and was unaffected by the presence of the interface. Visual observation indicated no significant displacement of the laser beams. Moreover, salt fingers were not observed at the interface.

In the above experiment the density difference was 0.0207 g/cm^3. McDougall (1979b) was able to carry successful LDV measurements with a density difference between the layers of about 0.015 g/cm^3 using a tank of dimensions 25.4 x 25.4 x 46.0 cm (l x w x h). The maximum distance the laser beams had to traverse through the interface in McDougall's experiments was 25.4 cm, as compared to 115 cm in our experiment. It is expected that by using the NaCl/ethanol solute pair in tanks comparable in size to McDougall's (1979b), LDV measurements can be done successfully with density differences of about 0.03 g/cm^3. This value is comparable to the maximum density difference across an interface in a stratified natural body of water. It is also worth mentioning that a laser beam penetrating the interface vertically is much less affected by the presence of the interface than a horizontal beam. As a result, vertical LIF measurements can be performed with relative ease when the refractive indices are matched.

References

McDougall, T.J. 1979a. On the elimination of refractive index variations in turbulent density stratified flows. J. Fluid Mech. 93, 83.

McDougall, T.J. 1979b. Measurements of turbulence in a zero-mean shear mixed layer. J. Fluid Mech. 94, 409.

Weast, R.C. 1976. *Handbook of Chemistry and Physics*. 56th ed., C.R.C. Press.

APPENDIX B

DETERMINATION OF THE DYE ABSORPTION COEFFICIENT

In order to determine the dye absorption coefficient ϵ of Rhodamine 6G dye in Equation (2.1) a stock solution with a known dye concentration was prepared. The 514 nm line of the 2W argon-ion laser described in Chapter 2 was directed horizontally through a 10.0 x 10.0 x 20.0 cm square glass container with the 20.0 cm side being vertical. After its passage through the container the beam entered the experimental tank (described in Chapter 2) which contained a homogeneous Rhodamine 6G dye solution. A section of the beam in the tank was imaged onto a Reticon array. The glass container initially contained pure water. Known volumes of the Rhodamine 6G solution were successively pipetted into the container thus yielding a solution of known dye concentration C. After each dye addition the container fluid was vigorously mixed using a magnetic stirrer and the average output of 512 array scans was recorded. Afterwards, the spatial average of five adjacent pixels, defined as V_c, was computed. This last averaging procedure was used to minimize the errors involved. $\ln(V_c)$ versus C is plotted in Figure B.1. ϵ was then determined from the (V_c, C) pairs by using Equation 2.1. Equation 2.1 in this case reduces to:

$$V_c = (V_c)_0 \, e^{-\epsilon C s_a}, \qquad (B.1)$$

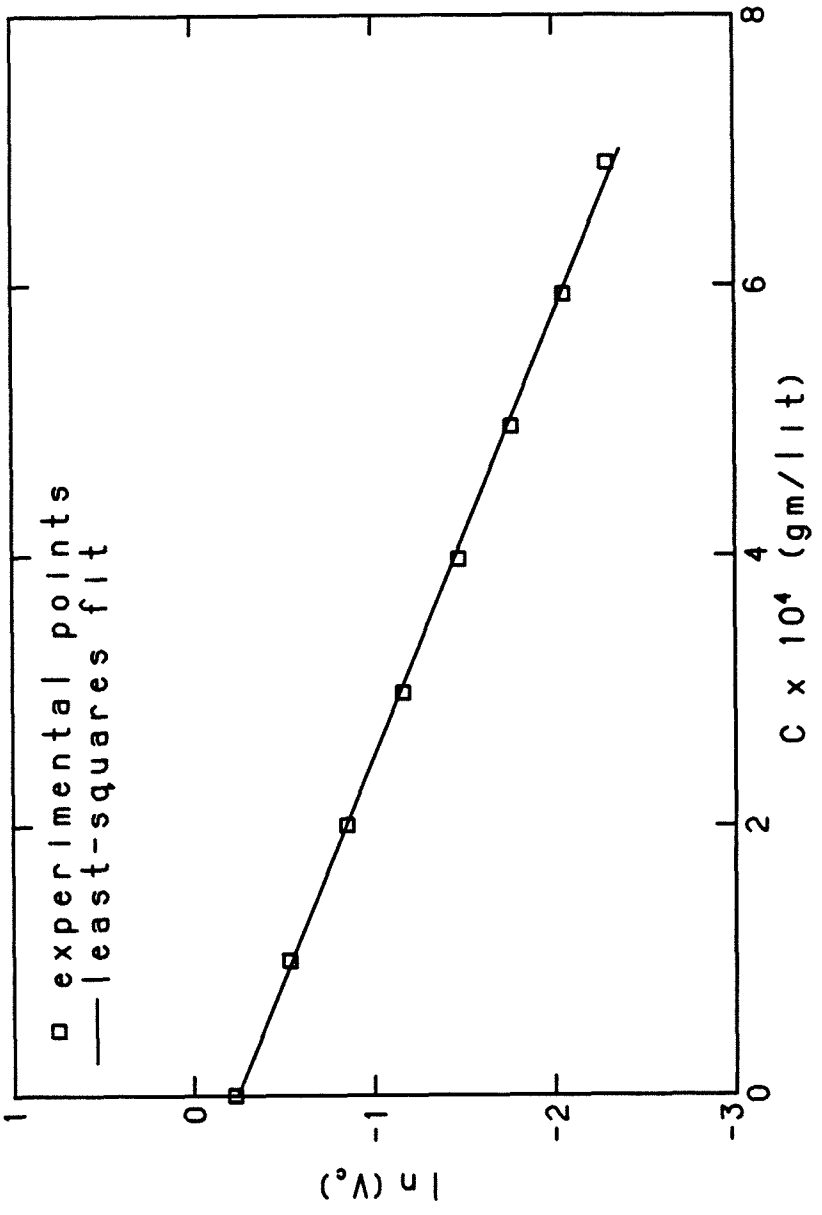

Figure B.1: ln (V_c) versus C

where $(V_c)_0$ is the value of V_c at C=0 and s_a is the width of the glass container, *i.e.*, 10.0 cm. The simplification of Equation (2.1) utilizes the fact that the array output voltage is proportional to the beam intensity. The slope in Figure B.1, which equals $-\epsilon s_a$, was determined from a least-squares best fit straight line and ϵ was calculated to be 300/cm-(gm/lit). It is worth mentioning here that the purity of the Rhodamine 6G powder was not precisely determined by the manufacturer (Sigma) and as a result the figure obtained in this study for ϵ is not suitable for powders of different purity.

APPENDIX C

HORIZONTAL INHOMOGENEITY OF OSCILLATING GRID TURBULENCE

C.1 Introduction

In this appendix we discuss some of the properties of oscillating grid induced turbulence, with particular emphasis on horizontal inhomogeneities. Figure C.1 presents the vertical r.m.s. velocity σ_w as a function of horizontal distance x_1/M at $z/a = 2.83$. M is the center-to-center spacing of the grid bars and is equal to 6.35 cm. The σ_w values are normalized by their spatial average, $[\sigma_w]$. It can be observed from Figure C.1 that $\sigma_w/[\sigma_w]$ exhibits a definite trend, with the peaks in velocity being separated by about a distance equal to M. Actually, the peaks in the r.m.s. vertical velocity occur directly below grid bars. Figure C.2 presents the normalized horizontal r.m.s. velocities as a function of horizontal distance for the same experiment. A similar trend seems to exist for the horizontal velocity as for the vertical velocity. However, the relative magnitude of the inhomogeneity in the horizontal velocity is less than that in the vertical velocity. Moreover, the peaks in $\sigma_u/[\sigma_u]$ are slightly shifted from the peaks in $\sigma_w/[\sigma_w]$.

The correlation coefficient between u and w, denoted by $\overline{u'w'}/[\sigma_u][\sigma_w]$, is plotted as a function of horizontal distance in Figure C.3. We may observe the existence of both positive and

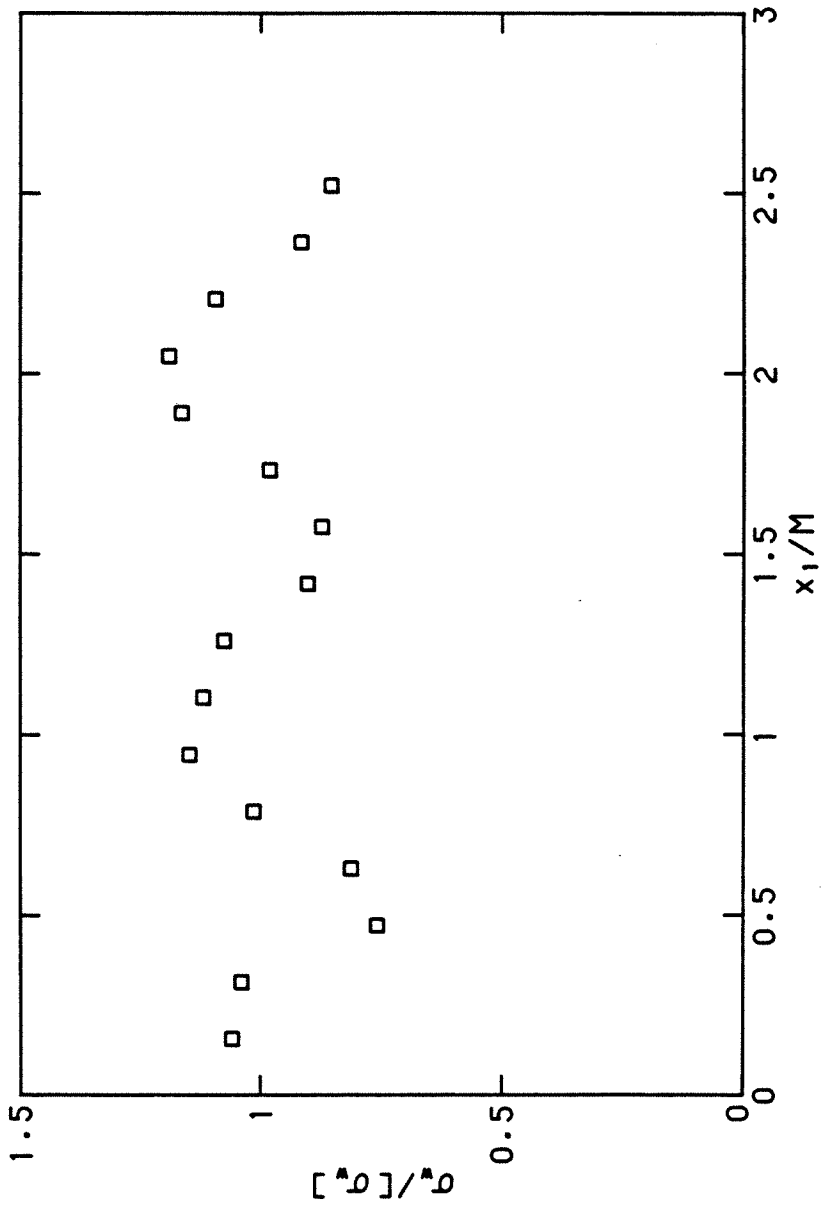

Figure C.1: Variation of the r.m.s. vertical velocity with horizontal distance. z/a = 2.83. a = 3.18 cm. M = 6.35 cm

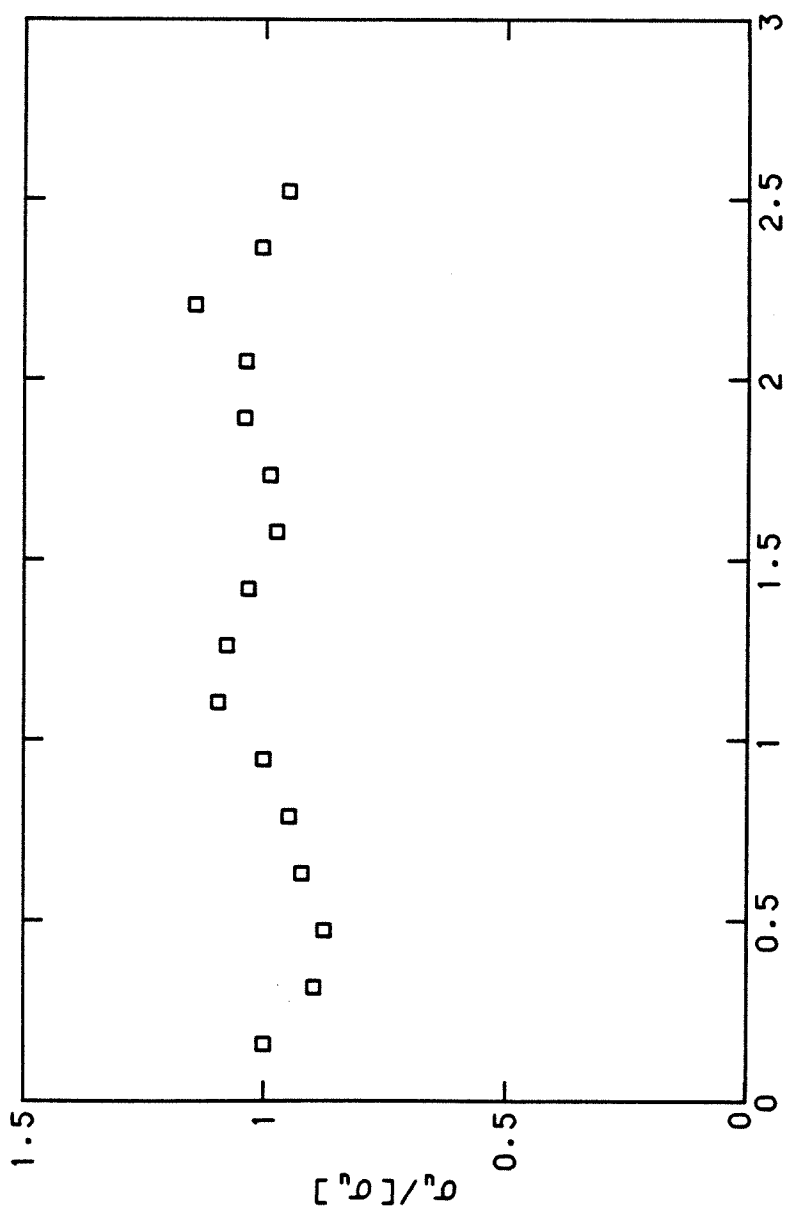

Figure C.2: Variation of the r.m.s. horizontal velocity with horizontal distance. z/a = 2.83. a = 3.18 cm. M = 6.35 cm

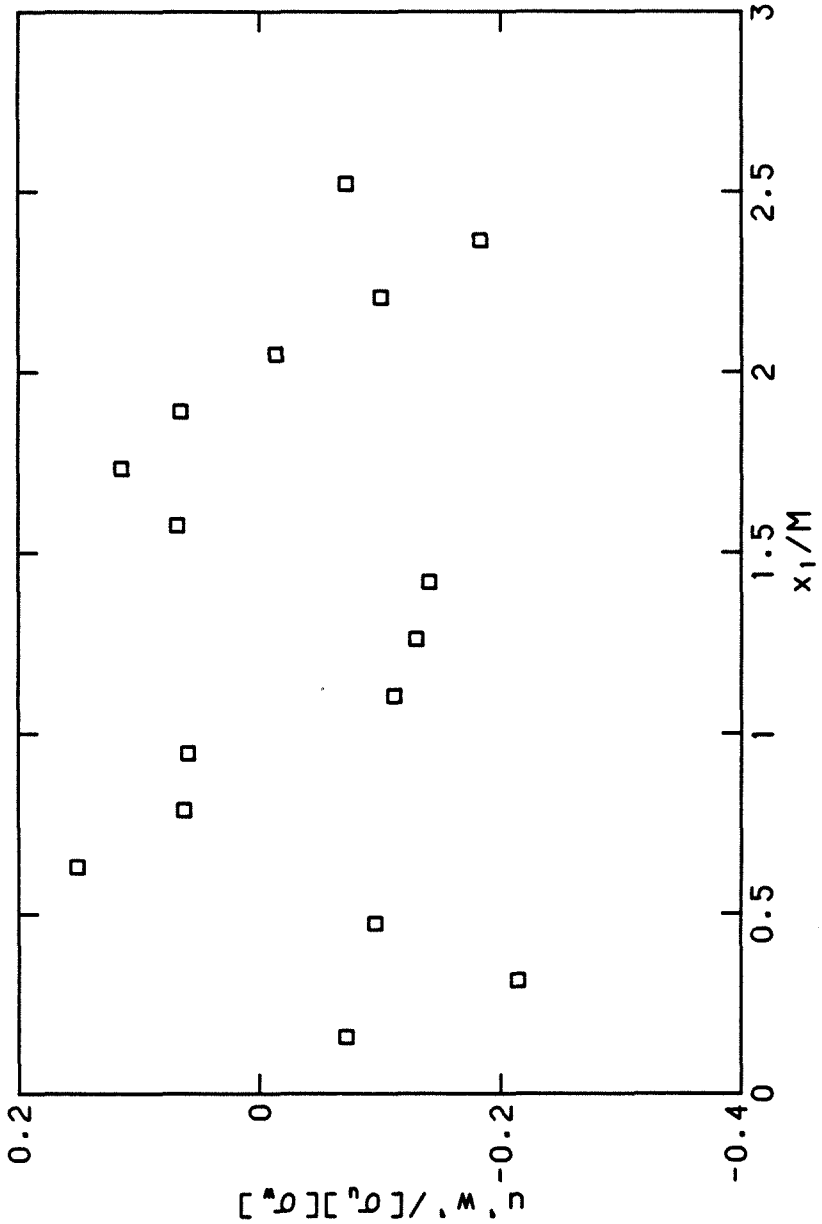

Figure C.3: Variation of the velocity correlation coefficient $\overline{u'w'}/([\sigma_u][\sigma_w])$ with horizontal distance.
z/a = 2.83. a = 3.18. M = 6.35 cm

negative peaks in the correlation coefficient. A comparison between Figures C.1, C.2, and C.3 indicates that the peaks in the velocity correlation coefficient are on either side of the peaks in the velocity. The above observations suggest that the turbulence produced by the grid may be viewed as a series of adjacent jets (or wakes) produced by the oscillatory motion of the grid bars and separated by a distance equal to the bar spacing.

It is of interest to investigate the evolution of these horizontal inhomogeneities with distance away from the grid. Figure C.4 presents a plot of $\sigma_w/[\sigma_w]$ versus horizontal distance at $z/a = 5.67$. In this figure, we may still observe the correlation between the peaks in velocity with the mesh size. However, the magnitude of the inhomogeneity in velocity is much less than that in Figure C.1. In order to investigate this effect more systematically, we will define θ as the ratio of the r.m.s. of the σ_w fluctuations along x_1 to $[\sigma_w]$. θ is a measure of horizontal inhomogeneity in the vertical velocity. Figure C.5 presents θ as a function of non-dimensional distance away from the grid, z/a. We may observe from Figure C.5 that θ decreases as we move away from the grid. In other words, the turbulence becomes less inhomogeneous with increasing distance from the grid. Figure C.6 presents $\overline{u'w'}/[\sigma_u][\sigma_w]$ as a function of x_1/M at $z/a = 5.67$. In this figure, we may still distinguish some peaks in the velocity correlation coefficient. However, some of the regularity observed in Figure C.3

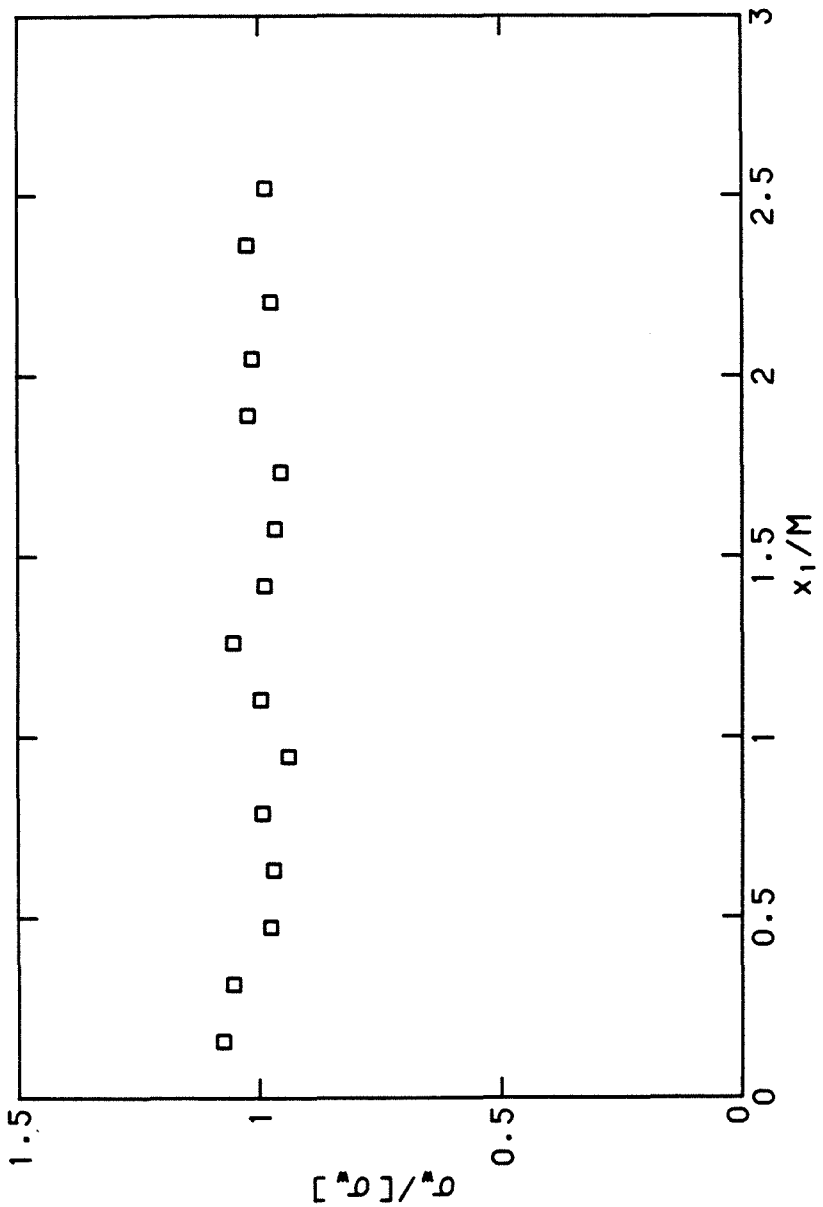

Figure C.4: Variation of the r.m.s. vertical velocity with horizontal distance. z/a = 5.67. a = 3.18 cm. M = 6.35 cm

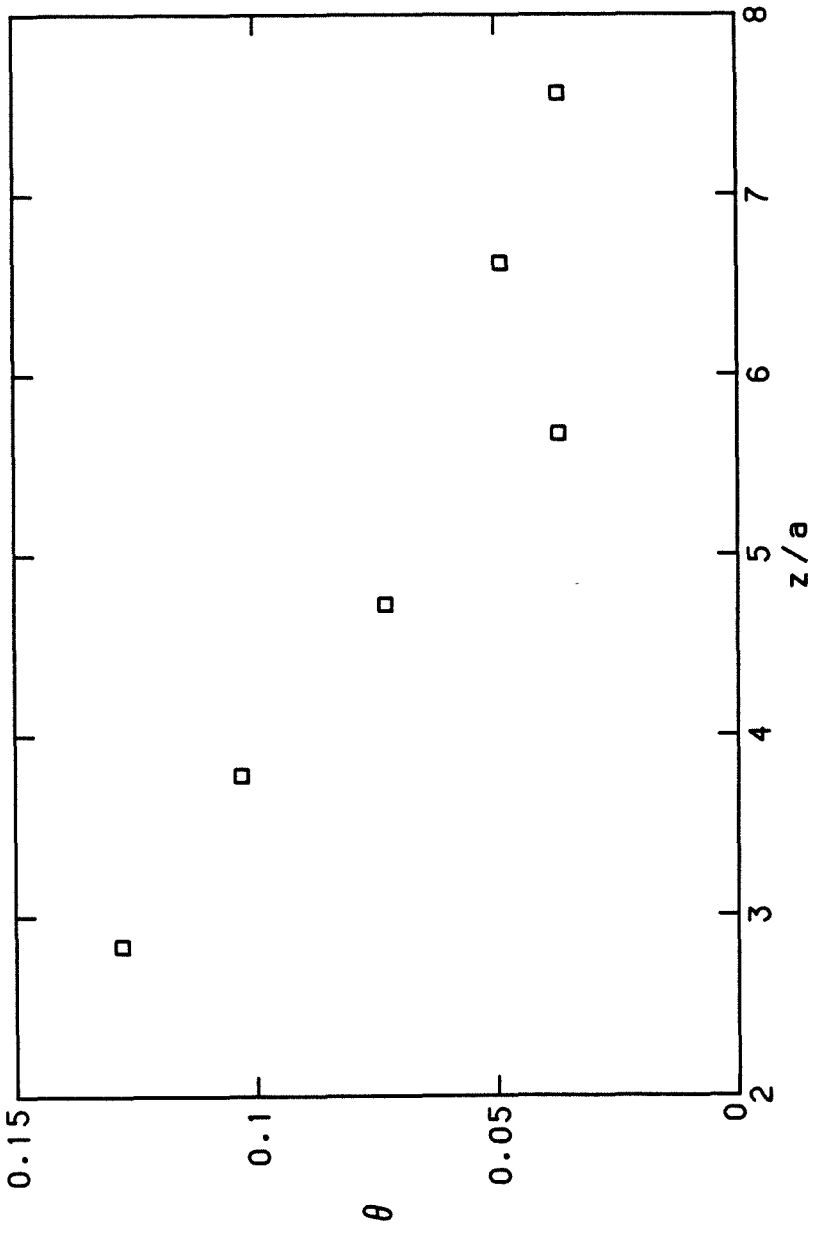

Figure C.5: Variation of θ with distance away from the grid, z/a.
a = 3.18 cm

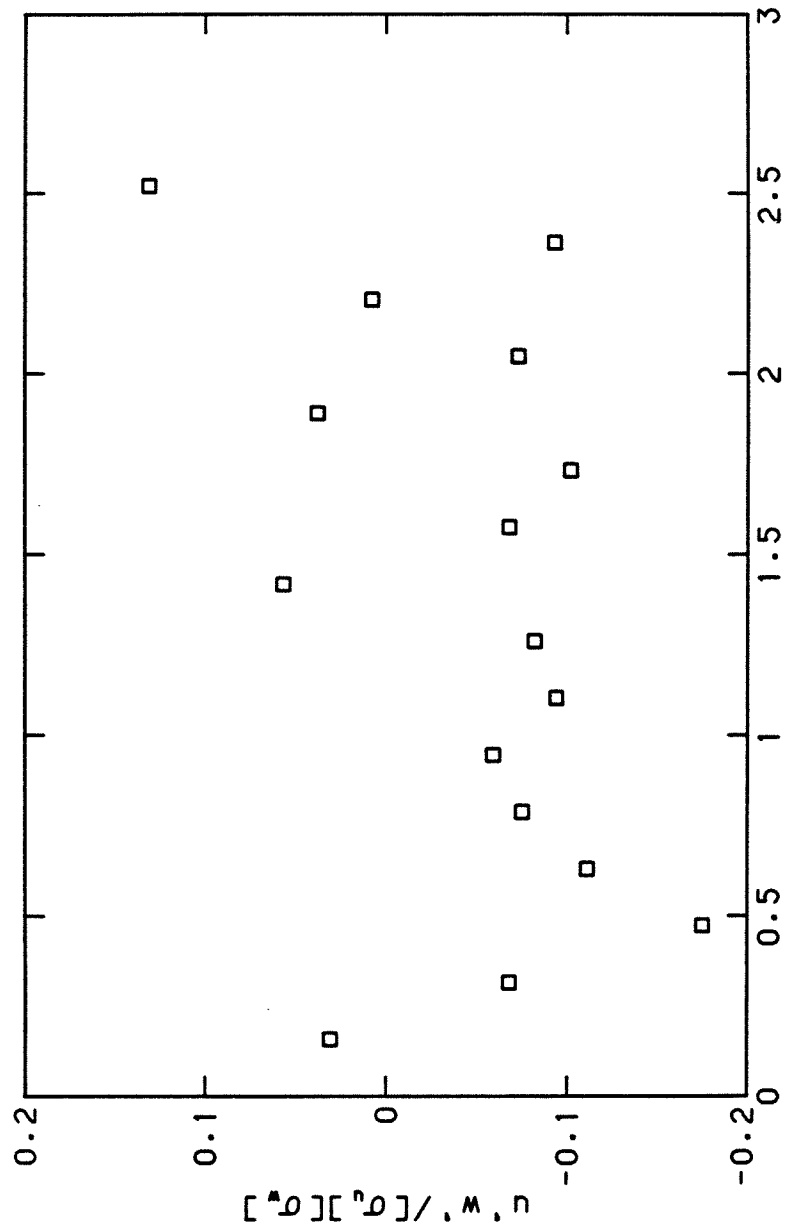

Figure C.6: Variation of the velocity correlation coefficient $\overline{u'w'}/([\sigma_u][\sigma_w])$ with horizontal distance.
z/a = 5.67. a = 3.18. M = 6.35 cm

(which presents data at smaller z/a) is lost.

The above observations suggest that the distinct jets (or wakes) generated near the grid merge into each other as we move away from the grid, and as a result, the separate identity of individual jets disappears with distance from the grid. It is also worth noting that all the experiments in the remainder of this work were performed at $z/a > 5.0$, a region in which the inhomogeneities in the velocity are not very serious.